Analysis of Metal to Composite
Adhesive Joints in Space Applications

Fredrik Fors

Teknisk Mekanik
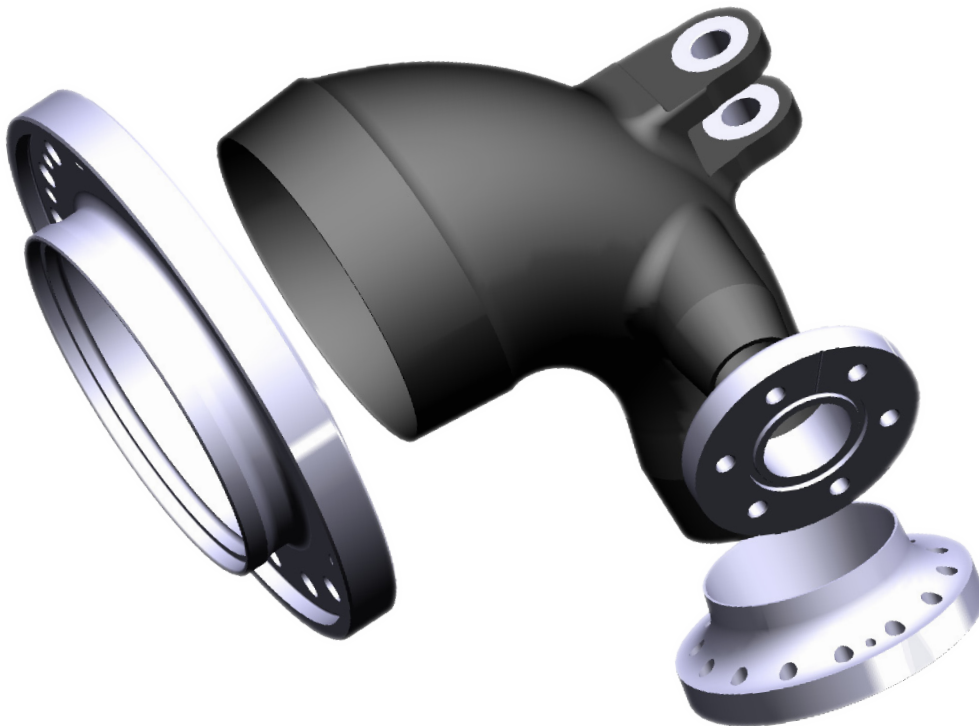
- I -

Preface

This report is the result of the final stage in the completion of a Master of Science degree in Mechanical Engineering at the Institute of Technology at Linköping University, Sweden. The work has been carried out at department 6670 Turbines & Rotors at the Volvo Aero Corporation (VAC) in Trollhättan, Sweden from January to May 2010.

I have always had an interest in aerospace technology and it has also been the focus for my engineering studies. I would therefore like to express my gratitude to my supervisor Staffan Brodin for giving me the opportunity to write this thesis within the subject at VAC, as well as to my professor at Linköping University, Peter Schmidt for excellent support and guidance during the semester.

I would also like to thank Fredrik Edgren and Niklas Jansson at VAC for invaluable advice and rewarding discussions regarding composite materials and engineering adhesives. A special thanks goes to Johan Andersson at dept. 6670 for coping with constantly having me at his desk asking basic questions about ANSYS programming or solid mechanics.

And last but not the least, a sincere thanks to my dear Abigail Cox for believing in me and wholeheartedly supporting me during the process as well as lending a native eye to the proof reading of the report.

Trollhättan, June 2010

_____

Fredrik Fors

Abstract

Within the European space programme, a new upper stage engine (Vinci) for the Ariane 5 launcher is being developed, and the Volvo Aero Corporation (VAC) is contributing with turbines for the fuel turbopumps. This MSc thesis investigates the possibility of designing the Turbine Exhaust Duct (TED) of the Vinci-engine in a carbon fibre composite material with adhesively attached titanium flanges. The focus of the project has been on stress analyses of the adhesive joints using Finite Element Methods (FEM), more specifically by using a cohesive zone material (CZM) to model the adhesive layer. Analysing adhesive joints is complex and an important part of the work has been to develop and concretise analysis methods for future use within VAC.

To obtain the specialised material parameters needed for a CZM analysis, FE-models of tensile test specimens were analysed and the results compared to those of equivalent experimental tensile tests. These parameters were then used when analysing the TED geometry with load cases specified to simulate the actual operation conditions of the Vinci engine. Both two-dimensional axisymmetric and fully three-dimensional models were analysed and, additionally, a study was performed to evaluate the effect of cryogenic temperatures on the strength of the joint.

The results show that the applied thermal and structural loading causes local stress concentrations on the adhesive surface, but the stresses are not high enough to cause damage to the joint if a suitable joint design is used. Cryogenic temperatures (-150 °C) caused a significant strength reduction in the tensile specimens, partially through altered adhesive properties, but no such severe effects were seen in the temperature-dependent FE-analyses of the TED. It should be pointed out however, that some uncertainties about the material parameters exist, since these were obtained in a rather unconventional way. There are also several other important questions, beside the strength of the adhesive joint, that need to be answered before a metal-composite TED can be realised.

Sammanfattning

Volvo Aero deltar i utvecklingen av Vinci, en ny motor till det övre steget i den europeiska Ariane 5-raketen. Detta examensarbete behandlar möjligheten att tillverka ett turbinutlopp (TED) till vätgasturbinen i Vinci-motorn i kompositmaterial med flänsar i titan för att på så sätt uppnå en viktbesparing gentemot den tidigare konstruktionen i gjuten Inconel 718. Fokus har legat på att analysera hållfastheten i de limfogar som är tänkta att sammanfoga huvudröret med flänsarna, genom analyser med finita elementmetoden (FEM). Ett viktigt syfte har även varit att, för Volvo Aeros räkning, samla praktiska erfarenheter angående numerisk analys av limfogar, särskilt med användning av kohesiva zon-element för att modellera limfogen.

FEM-analyser har gjorts av provstavsmodeller, där resultaten sedan jämförts med experimentella dragprovsresultat för att ta fram lämpliga material- och modelleringsparametrar för analys med kohesiva zonelement. Därefter tillämpades dessa parametrar i analyser av den verkliga TED-geometrin med relevanta lastfall framtagna för att simulera driftsförhållandena i Vinci-motorn. Lastfallsanalyser med både tvådimensionellt axisymmetriska och tredimensionella geometrimodeller genomfördes, liksom uppskattningar av limfogens styrka vid kryogena driftstemperaturer.

Resultaten pekar entydigt mot att en limfog med en ändamålsenlig tvärsnittsgeometri skulle hålla för de angivna lasterna utan att ta skada. De spänningskoncentrationer som uppstår ger lokalt höga spänningar i limmet, men inte på nivåer som skulle kunna orsaka brott. Det finns dock en viss osäkerhet angående riktigheten i materialparametrarna då en något okonventionell metod användes för att ta fram dessa. Flera stora frågor finns fortfarande kvar att besvara innan en metall-komposit konstruktion kan realiseras, inte minst hur flödeskammarens komplicerade geometri skall kunna tillverkas i kompositmaterial.

Contents

Abbreviations

ASTM	American Society of Testing and Materials
BC	Boundary Condition
CAE	Computer Aided Engineering
CFRP	Carbon Fibre Reinforced Plastic
CTE	Coefficient of Thermal Expansion
CZM	Cohesive Zone Model
DCB	Double Cantilever Beam
DLJ	Double-Lap Joint
DOE	Design of Experiments
DOF	Degree of Freedom
ENF	End Notch Flexure
FEA	Finite Element Analysis
FEM	Finite Element Method
GH2	Gaseous Hydrogen
GPS	Generalised Plane Strain
GTO	Geostationary Transfer Orbit
GUI	Graphical User Interface
LEFM	Linear Elastic Fracture Mechanics
LH2	Liquid Hydrogen
LOX	Liquid Oxygen
NRFP	Nationellt Rymdtekniskt Forskningsprogram
PVD	Principle of Virtual Displacement
RT	Room Temperature
RTM	Resin Transfer Moulding
SLJ	Single-Lap Joint
TED	Turbine Exhaust Duct
TPH	Hydrogen Turbo-Pump
TPO	Oxygen Turbo-Pump
VAC	Volvo Aero Corporation

– X –

1. Project Background

This introductory chapter presents background information regarding this thesis and the project it is a part of. A description of the aims and goals set out for the work is also included.

1.1 Volvo Aero Corporation

The Volvo Aero Corporation (VAC) is one of the companies incorporated in the Volvo Group, also including Volvo Trucks, Volvo Construction Equipment, Volvo Buses, Volvo Penta (producing marine engines) as well as numerous other business units aimed at supporting the main industries. Within the group are also other brands owned by Volvo such as Mack-, Renault- and UD trucks.

Volvo Aero produces and develops components for both commercial and military aero engines as well as for rocket engines for space propulsion within the European space programme. An important part of the business, although not as prominent as it used to be, is the partial development, manufacturing and assembly of military aircraft engines to the Swedish Air Force.

The tremendous complexity of a modern turbo jet or turbo fan engine means that very few companies have the capital and advanced engineering competence needed to develop a new engine from scratch. In today's market, the development of a new aircraft engine is a joint venture between a main contractor and several partners. The Volvo Aero Corporation has the role as a risk-sharing partner to the main engine developers, contributing with production development capital and responsibility for certain engine components. At present, VAC is a partner in engine programmes for Rolls Royce, General Electric, Pratt & Whitney and Snecma, meaning that VAC-

Figure 1.1. *Volvo Aero flags at main office in Trollhättan.*

developed components can be found in 90% of the large commercial aircraft in the world as well as in the Ariane 5 rockets.

Ever since the foundation, the company headquarters and main production site have been situated in Trollhättan, Sweden but today there are several VAC facilities all around the World including:

> ➢ Volvo Aero Connecticut – Newington, Connecticut, USA
> ➢ Volvo Aero Services – Boca Raton, Florida, USA
> ➢ Volvo Aero Norge – Kongsberg, Norway
> ➢ Applied Composites AB, ACAB – Linköping, Sweden

Historically, VAC has its origin in Svenska Flygmotor AB (Swedish Aero Engine Corporation) and has since the 1930's had the contract to deliver aircraft engines to the Swedish Air Force. Since the formation of Svenska Aeroplan-Aktiebolaget (SAAB, Swedish Aeroplane Corporation) in 1937, there has been a close link between the two when it comes to producing the aircraft for the Swedish Air Force and as of yet they have together developed and produced all main Swedish military aircraft. Apart from a few early attempts to design an entire engine, the engines produced by VAC have been modified and specialised derivatives of military engines licensed from major companies in the business. For example, the military engine currently in production, the RM12 powering the Saab Gripen fighter jet, is a General Electrics F404J enhanced and modified for single-engine use [1].

1.2 The Vinci Engine Project

Since the early days of the European space programme, Volvo Aero has been participating with specialised production of rocket nozzles and combustion chambers. In the 1970's VAC started the production of combustion chambers and nozzles for the Viking engines powering the early Ariane rockets. When the development of the Ariane 5 started in the early 80's, VAC's involvement increased and they were also given responsibility for design and development of turbines and nozzles for the new Vulcain 2 main stage engine. Today, there is con-

Figure 1.2. *Ariane 5 rocket during lift-off.*   Figure 1.3. *The Vinci upper stage engine.*

tinuous production and engineering support of Vulcain 2 components as well as ongoing development of both the next generation main stage engine, HTE, and a new upper stage engine, Vinci.

The Vinci engine is a cryogenic expander cycle rocket engine, using liquid hydrogen (LH2) and liquid oxygen (LOX) as fuel. Within the Ariane 5, the second stage engine is situated in the top part, just below the payload and is lit once the main stage engine and boosters have brought the system above Earth's atmosphere to an altitude of about 150 km altitude. There it produces the thrust necessary to inject the payload into its assigned orbit. The main advantage of the Vinci engine compared to its predecessor, the HMB7, is that it produces almost three times as much thrust and thereby allows for an improved payload capacity into Geostationary Transfer Orbit (GTO); increasing Ariane 5's capacity from today's 9.6 tons to 11.6 tons. In addition to this, Vinci is capable of restarting in space up to five times which facilitates precision delivery of multiple satellites [2].

1.3 The Turbine Exhaust Duct

For the Vince engine, VAC is designing the turbines for the LOX and LH2 fuel supply pump systems. In the Hydrogen Turbo-Pump (TPH), high pressure gaseous hydrogen (GH2) provides the power through a turbine connected to the pump drive shaft. After passing the turbine, the GH2 is passed through the Turbine Exhaust Duct (TED) in which it is divided into a main flow to power the Oxygen Turbo-Pump (TPO) and a secondary bypass that can be passed on directly to the combustion chamber.

Figure 1.4. TPH components made by VAC with the TED to the left.

Vinci LH2 turbine data [3]

- ➢ Number of stages   1
- ➢ Nominal speed   91,000 rpm (max 102,000)
- ➢ Nominal power output   2500 kW (max 3700 kW)
- ➢ Mean gas diameter   120 mm
- ➢ Mass flow   4.9 kg/s
- ➢ Turbine inlet pressure   180 Bar (max 232 Bar)
- ➢ Turbine inlet temperature   245 K (Max 325 K)
- ➢ Pressure ratio   2:1

The TED operates under very demanding conditions with cryogenic temperatures, high internal pressure, external structural loads and a pure hydrogen environment. Typically during an engine run cycle, the temperature inside the TED varies between room temperature and -140°C and the internal pressures reaches as high as 10 MPa. Naturally this is very stressing on the component material and the present TED is a robustly designed in cast Inconel 718, a nickel-based "super alloy".

1.4 The KOMET Research Project

Due to the extreme costs associated with delivering cargo into space, there is a strong demand from the space industry to increase the load capacity of the carriers. To keep the total weight of the system unchanged, an increase in load capacity must be accompanied by a decrease in the structural weight of the carrier. Just as within the aerospace and to some extent the automotive industry, the use of lightweight composite material to replace earlier all-metal constructions has accelerated. There are still inevitably components that have to be made of metal and the interface between the different materials can then become an engineering challenge. To deepen the understanding of metal-composite hybrid structures in aerospace applications, the research project KOMET (KOMposit mot METall) has been set up as a joint effort between VAC, RUAG Aerospace Sweden AB and the research institute Swerea SICOMP AB (Sicomp). The project is partially funded by, and administrated within, the National Space Research Programme (NRFP, Nationellt Rymdtekniskt Forskningsprogram).

From VAC's side, it has been proposed to manufacture the TED in a composite material in order to reduce the weight of the present design which due to the use of Inconel 718 is relatively heavy with a weight of about 7.7 kg. The flanges that form the interface with surrounding engine parts will still need to have a metal contact surface against the other components in order to assure a tight high-pressure seal. For this reason a metal-composite hybrid design is proposed where metal flanges are attached to a composite tubular body. The component geometry and the demand for a smooth inner surface leave adhesives as the only feasible option for the joints. A preliminary study of the stresses in such an adhesively bonded flange has already been carried out by Sicomp and their conclusion was that although the joint was severely stressed further analysis was needed to determine the feasibility of the design [4].

1.5 Thesis Project Specifications

The objective of this thesis project is to further investigate the possibility of a metal-composite hybrid design of the TED. More work has been done in the KOMET project and tests have been conducted to characterise the strength of a titanium-to-composite joint. This knowledge together with more advanced and specialised analysis methods such as cohesive zone modelling are to be applied to verify and extend the work done in the preliminary study. In addition, more realistic joint and component models as well as more detailed load cases will be developed and employed to evaluate the feasibility of a hybrid design. The key questions set out in the initial project specifications are:

> ➢ *Is it feasible to design and manufacture a TED in metal-composite hybrid design?*
> ➢ *What would the design of a metal to composite interface be like?*
> ➢ *Will the bonded interface of the TED be strong enough to sustain the specified loads?*
> ➢ *What could the design of a hybrid TED be like?*
> ➢ *What difficulties could be expected in hybrid TED design?*

The project is focused on numerical analysis of the joint itself and identification of critical parts and load cases. Since there is limited experience in VAC of numerical analysis of adhesive joints, the project will also result in some general guidelines and recommendations for future analyses of adhesively bonded structures.

2. Theoretic Background

This aim of this section of the report is to provide the reader with some insight on the fundamentals of the engineering subjects employed in the project. It is written to give a basic understanding of the concepts and perhaps to refresh old knowledge but should not be considered a comprehensive description of the topics that are covered.

2.1 Adhesive Joint Theory

Traditionally in engineering, structural joining has been synonymous to riveting, bolting and other purely mechanical fastening together with welding or soldering in the case of metallic construction materials. Up until the introduction of the polymeric adhesives around the time of the Second World War these were the only means of joining available but with the increased use of plastics, and more importantly fibre reinforced composite materials, the use of adhesive joining has increased rapidly and is today found in numerous applications with different material configurations [5].

The reason for the increased use of adhesive joining is that it can provide a number of structural and economical advantages over more traditional methods of joining, of course assuming that the joint is properly designed. One of the most important features to keep in mind during the initial joint design is that adhesive joints are very strong in shear, but unfortunately are very vulnerable to normal stresses (in the context of adhesives commonly referred to as peel stresses). Provided that the joint is loaded in its favourable direction, some of the advantages are [6]:

- ➢ High strength to weight ratio
- ➢ Stresses distributed evenly over the joint width
- ➢ No drilled holes needed
- ➢ Weight and material cost savings
- ➢ Improved aerodynamic surface design
- ➢ Superior fatigue resistance
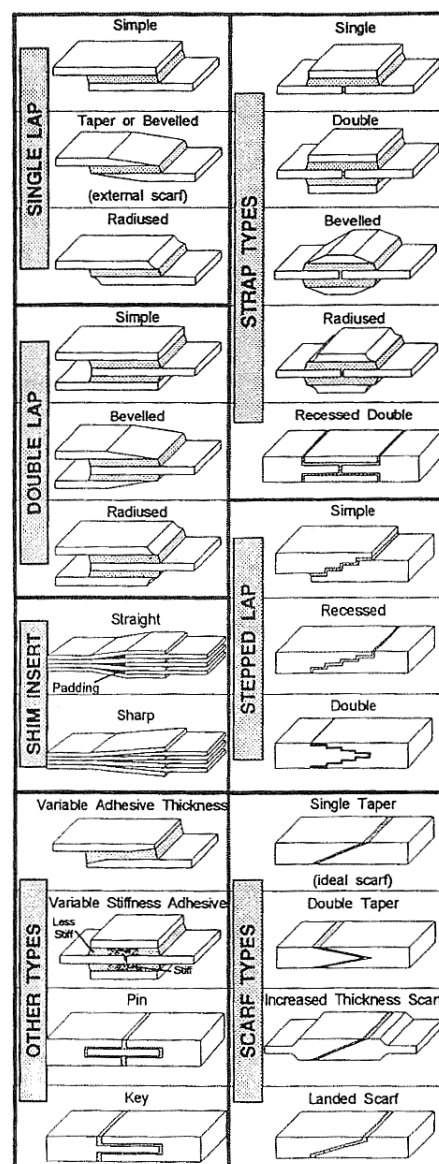- ➢ Outstanding electrical and thermal insulation

Figure 2.1. *Cross sections of a number of different adhesive joint*

As with any other technology, there are also limitations to consider when using adhesives in engineering. Elevated temperatures and high humidity can result in negative effects on the strength of some types of adhesives, especially when under continuous stress, and as with other polymeric materials, creep effects must be considered [7]. Even though manufacturing procedures such as drilling, machining and riveting can be avoided when using adhesive fastening, this is replaced with a need for careful surface preparation prior to bonding, especially when using metal adherends.

When designing an adhesively bonded structure, one of the first questions that arise is the cross-sectional geometry of the joint. Since the joint geometry greatly affects the stress distribution in the adhesive it must be carefully selected with the expected load case, adherend materials and global structural allowances in mind. Figure 2.1 shows a comprehensive overview of the most commonly used engineering adhesive joints and the terminology of the various adherend shapes [8].
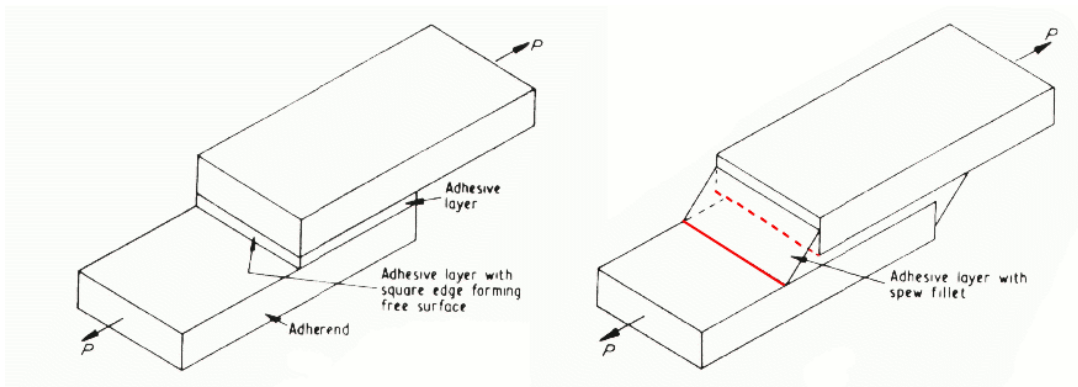
Figure 2.2 *Overview of a loaded SLJ with and without an adhesive spew fillet. Areas sensitive to crack initiation are marked in red.* [8]

The simplest type of joint, the single-lap joint (SLJ), is due to its simplicity commonly occurring and frequently used for test specimens. The load bearing capabilities are however limited by peel stresses induced by a bending moment resulting from the pulling forces not being collinear. These peel stresses can be severely reduced by instead using a double lap joint (DLJ) that is symmetric about its longitudinal centreline (see Figure 2.2), but even with the peel reduced to manageable levels, the stress state in the adhesive is complicated and not easily determined. In fact, most of the other joint configurations shown in Figure 2.1 are designed as different ways of reducing local end stress concentrations and peel.
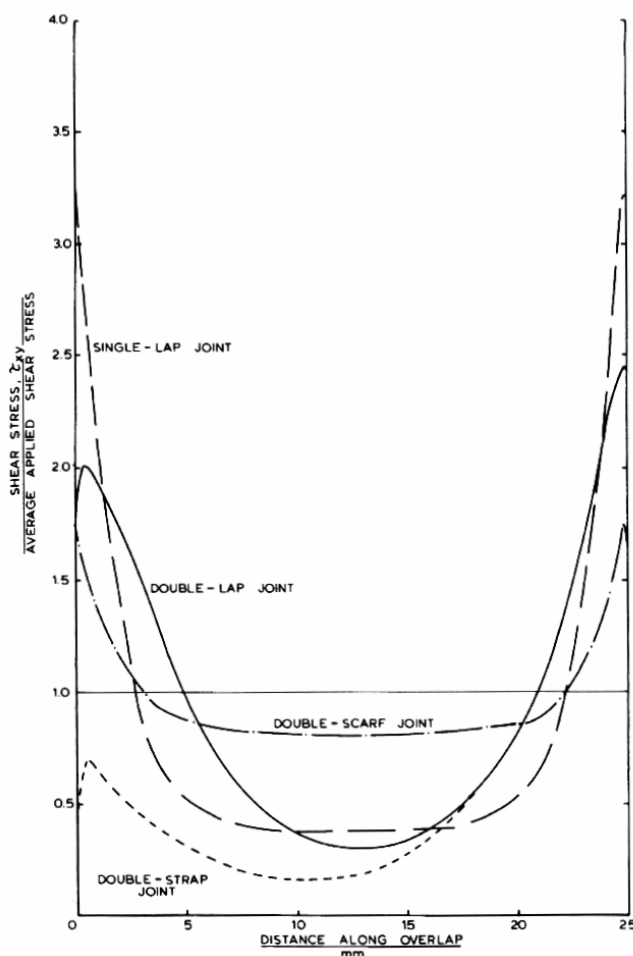
Figure 2.3. *Adhesive shear stress distribution along the over-lap length of four different joint types with CFRP adherends.* [8]

In the typical case of an axially loaded DLJ the principal stresses in the adhesive layer are considerably higher at the ends of the adherends, both in shear and peel. This comes as a result of elasticity effects in the adherends and is seen in all types of adhesive joints. The result is that an adhesive joint when failing tends to crack open in one end and then peel open until completely parted. The magnitude of the stress concentrations is dependent of numerous factors such as adherend material and geometry as well as the physical properties of the adhesive. The level of the shear stress along the overlap length with both adherends made of carbon fibre reinforced plastic (CFRP, or commonly carbon fibre composite) is presented in Figure 2.3 [8].

These local stress concentrations arise around the sharp corner at the end of the upper adherend and in the region where the adhesive attaches to the bottom adherend (areas marked red in Figure 2.2). With very sharp adherend corners the adhesive yields locally and a plastic zone is formed even at moderate loading. This can especially be the case in a numerical analysis where the adherend is usually modelled with perfectly sharp corners, but is generally less apparent in a real specimen where an edge radius even on the microscopic scale attenuates the stress singularity. When critically loaded, the failure is most often initiated in these stress concentration regions and then progresses along the adherend-adhesive interface [8].

2.1.1 Analytical methods

When it comes to determining the stresses in a specific joint configuration, today numerical FE-methods are used almost exclusively. Over the years however, extensive work has been done on deriving analytical methods for describing the behaviour of adhesive joints – a process that still continues. The foundations were laid out with the work of Volkersen in 1938 [9], where he derives a closed form mathematical solution for a simple case with tensionally loaded adherends and an adhesive loaded only in shear. For adherends with thicknesses t_1 and

t_2 and an adhesive layer of length *l,* width *b* and thickness t_3, he describes the relative displacement δ_x of the adherends as:

$$\delta_x = \delta_0 - \int_{-l/2}^{x} \varepsilon_1 dx + \int_{-l/2}^{x} \varepsilon_2 dx \qquad \text{(Eqn 2.1.1)}$$

From that he continues by assuming unit width and an applied load P together with basic expressions for δ_x, ε_1, and ε_2 to obtain an expression for the non-dimensionalised shear stress $\bar{\tau} = \tau_x / \tau_m$ as:

$$\bar{\tau} = \frac{\omega}{2} \frac{\cosh \omega X}{\sinh \omega/2} + \left(\frac{\psi - 1}{\psi + 1} \right) \frac{\omega}{2} \frac{\sinh \omega X}{\cosh \omega/2} \qquad \text{(Eqn 2.1.2)}$$

where

$$\left.\begin{aligned}
\omega^2 &= (1+\psi)\frac{Gl^2}{Et_1 t_3} \\
\psi &= t_1/t_2 \\
\tau_m &= P/bl \\
X &= x/l, \qquad -\tfrac{1}{2} \leq X \leq \tfrac{1}{2}
\end{aligned}\right\} \qquad \text{(Eqn 2.1.3)}$$

This in turn leads to a maximum adhesive shear stress at the end of the overlap:

$$\bar{\tau}_{\max} = \sqrt{\frac{\phi}{2}} \coth \sqrt{\frac{\phi}{2}} \qquad \text{(Eqn 2.1.4)}$$

Volkersen's solution can be considered the most basic and simplified description of an adhesive joint, but still, as can be seen from the abbreviated derivation above, results in a fairly complicated final expression. This theory also does not take into account two important factors that have influence on the joint strength. First, as can be seen in Figure 2.4, the directions of the tensional forces on the adherends are not collinear and there will as a result of this be a bending moment applied to the joint. Second, the adherend bend under the applied load causing a rotation of the joint.

Another classic analytic work in the field of adhesive joints, that also takes these additional factors into consideration, was presented by Goland and Reissner in 1944 [10]. The rotation of the joint causes the problem to become geometrically nonlinear, and Goland and Reissner have taken this into account by introducing a bending moment factor, which relates the bending moment at the end of the overlap to the in-plane loading.
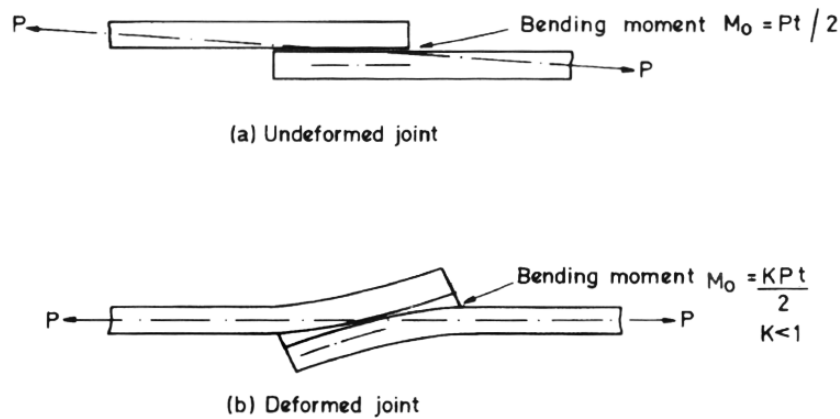
Figure 2.4. *Geometrical illustration of Goland and Reissner's bending moment factor.* [8]

These are just two examples of the early work done on the subject, but there has been more work continuously published over the years since then. While the above example only considered shear stress in single lap joints, there are analytical methods developed for a wide variety of joint configurations and load cases. There has however, since the 1970's, been more focus on developing the more adaptable numerical techniques, capable of producing good results for an almost completely arbitrary joint geometry and load case. Today, numerical methods is the dominant alternative when performing in-depth analyses of adhesive joints, even though analytical methods still can provide a good first estimate of the final result or be used as a complement to check the validity of the numerical solution.

2.2 Numerical Analysis in Solid Mechanics

Even though to this date a considerable amount of work has been done in the field of analytic research on adhesive joints, its use is still limited in engineering because of the restriction to fairly simple geometries and load cases. In many situations it is possible to, through assumptions and suitable simplifications use these analytical models to draw initial conclusions of the strength and stress distribution of a joint, but in modern engineering a more realistic and thorough analysis is most often required, involving complex geometries and influence of multiple types of loads. As in traditional solid mechanics, these needs have driven the evolution of computerised numerical methods, in this context almost synonymous to the Finite Element Method (FEM). By using Finite Elements techniques, problems of arbitrary geometry and load specification can be analysed with high accuracy, as long as the problem is set up properly with correct boundary condition and a suitable spatial discretisation (mesh).

2.2.1 Introduction to Elastic FEA

This introductory chapter cannot have any ambitions of a complete description of FEM, but a brief derivation of the basics is given as reference for the Cohesive Zone Model chapter. The most common form of Finite Element Analysis (FEA) is the linear elastic structural analysis, where the degrees of freedom (DOF) are the displacements of the nodes, from which strains and then stresses can be calculated. This is done in principle by first defining the boundary value problem (the strong form) and then transforming this equation into a variational (weak) form that in turn can be discretised and solved numerically. The following derivation will use the conventional index summation convention using indices i,j,k and l which all take on values $1,\ldots,n_{sd}$ where n_{sd} is the number of spatial dimensions. Repeated indices imply summation and differentiations is denoted by a comma (Example: $u_{,i} = u_{,x_i} = \partial u / \partial x_i$).

2.2.1 - a Strong Formulation

In the general 3D elastic case the boundary value problem to be solved is illustrated in Figure 2.5. An arbitrary body of volume V is subjected to a traction t on the surface S_t and a prescribed zero-displacement at the boundary S_u. Given the traction $\mathbf{t} = (t_i)$, find the displacement $\mathbf{u} = (u_i)$ such that the equilibrium equation is satisfied:

Figure 2.5. *Generic 3D body with traction and displacement BC's.*

$$\sigma_{ij,j} = 0 \qquad \text{in } V \qquad \text{(Eqn 2.2.1)}$$

and the boundary conditions hold.

$$u_i = 0 \qquad \text{on } S_u \qquad \text{(displacement condition)}$$

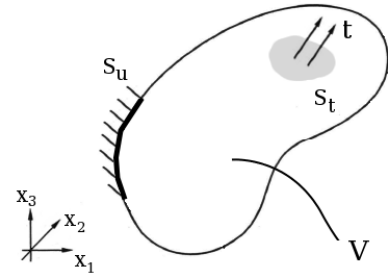$$\sigma_{ij} n_j = t_i \qquad \text{on } S_t \qquad \text{(traction condition)}$$

(Eqn 2.2.2a-b)

The above boundary conditions describe a somewhat simplified state not including any prescribed displacements or body forces acting on the body. The boundary conditions consists of a homogeneous BC on the surface S_u and a natural BC on S_t, mathematically defining the strong form as a multi-dimensional second order mixed boundary value problem [11].

In addition to the equations defined above the physical material behaviour of the body is dictated by the constitutive relationship which in this example simply is Hooke's law of elasticity:

$$\sigma_{ij} = E_{ijkl}\varepsilon_{kl} \qquad \text{(Eqn 2.2.3)}$$

where the strain tensor ε_{ij} contains the linear strain components and is defined to be the symmetric part of the displacement gradients [12]:

$$\varepsilon_{ij}(\mathbf{u}) = \frac{1}{2}\left(u_{i,j} + u_{j,i}\right) \qquad \text{(Eqn 2.2.4)}$$

The above equations form the basic mathematical equation system with $\mathbf{u}$ as the primary unknown that needs to be solved for at any point of interest. This analytical expression is however not very suitable for numerical solving, which is the reason why the strong form needs to be transformed into the variational, or weak, form.

2.2.1 - b Variational (Weak) Formulation

The variational form, as defined by the principle of virtual displacements (PVD), is a set of integral equations that are the equivalent of the strong form. The first step in obtaining this is to define the displacement variations w_i (also known as the virtual displacements) that belong to the variation space W consisting of the kinematically admissible displacements:

$$\text{W} := \left\{ \mathbf{u} = (u_i) \,\middle|\, \mathbf{u} = \mathbf{0} \ \ \text{on} \ \ S_u \right\} \qquad \text{(Eqn 2.2.5)}$$

By multiplying the strong form equilibrium equation (eqn. 2.2.1) with $w_i \in$ W and integrating over the entire domain V a basic integral equation is obtained:

$$0 = \int_V w_i \sigma_{ij,j} dV \qquad \text{(Eqn 2.2.6)}$$

This equation can then be transformed into the final variational form by using partial integration and the divergence theorem. Given the applied traction $\mathbf{t} = (t_i)$, find $\mathbf{u} \in$ W such that

$$\int_V \sigma_{ij}\varepsilon_{ij}(\mathbf{w})dV - \int_{S_t} t_i v_i dS = 0 \quad \forall\, \mathbf{w} \in \text{W} \qquad \text{(Eqn 2.2.7)}$$

where σ_{ij} is defined in terms of $\mathbf{u}$ by the constitutive law (Eqn 2.2.3) and equation 2.2.4 [12].

2.2.1 - c Discretisation

Before applying numerical solution techniques to obtain a solution the continuous functions of the problem need to be discretised over the domain. The spatial discretisation if often done in a separate process where a suitable mesh is defined and shape functions are generated depending on the element type used. By using linearly independent shape functions the integral equation that is the variational form can be rewritten into a matrix formulation that is well suited for numerical solving. For the $\mathbb{R}^3$ case, the stress, strain and displacement components are arranged in matrices as follows:

$$\boldsymbol{\sigma} = \begin{Bmatrix} \sigma_{11} \\ \sigma_{22} \\ \sigma_{33} \\ \sigma_{12} \\ \sigma_{13} \\ \sigma_{23} \end{Bmatrix}, \qquad \boldsymbol{\varepsilon} = \begin{Bmatrix} \varepsilon_{11} \\ \varepsilon_{22} \\ \varepsilon_{33} \\ 2\varepsilon_{12} \\ 2\varepsilon_{13} \\ 2\varepsilon_{23} \end{Bmatrix}, \qquad \mathbf{u} = \begin{Bmatrix} u_1 \\ u_2 \\ u_3 \end{Bmatrix}; \qquad \mathbf{w} = \begin{Bmatrix} w_1 \\ w_2 \\ w_3 \end{Bmatrix}; \qquad \mathbf{t} = \begin{Bmatrix} t_1 \\ t_2 \\ t_3 \end{Bmatrix}$$

These basic vectors and matrices are related to each other and the element definitions through the following elementary matrix relations:

$$\mathbf{u} = \mathbf{Ad}; \qquad \boldsymbol{\varepsilon} = \mathbf{Bd}; \qquad \boldsymbol{\sigma} = \mathbf{E}\boldsymbol{\varepsilon}; \qquad \mathbf{w} = \mathbf{A}\delta\mathbf{d} \qquad \text{(Eqn 2.2.8)}$$

where the **A** and **B** matrices contain the shape functions and their derivatives, **E** is the elasticity matrix, **d** is the nodal displacements and $\delta\mathbf{d}$ denotes the nodal displacement variations. These matrices are then inserted into the variational formulation to form a matrix equation:

$$\delta\mathbf{d}^T \left(\int_V \mathbf{B}^T \mathbf{E}\mathbf{B} \, dV \, \mathbf{d} - \int_{\mathbf{S_t}} \mathbf{A}^T \mathbf{t} \, dS \right) = \mathbf{0} \qquad \text{(Eqn 2.2.9)}$$

which has to be satisfied for all $\delta\mathbf{d}$ [12]. This equation defines the global displacements under a given load and is more commonly expressed on a pure matrix notation form as:

$$\mathbf{Kd} = \mathbf{F} \qquad \text{(Eqn 2.2.10)}$$

where

$$\mathbf{K} = \int_V \mathbf{B}^T \mathbf{E}\mathbf{B} dV \qquad \text{(Eqn 2.2.11)}$$

is the global stiffness matrix, and

$$\mathbf{F} = \int_V \mathbf{A}^T \mathbf{t} dS \qquad \text{(Eqn 2.2.12)}$$

is the global force vector. From Eqn. 2.2.10 the corresponding stiffness matrix and the nodal force and displacement vector can be identified for a single element.

Normally when performing an FEA the force acting on a body is known. This allows for computation of the global displacements through inversion of the **K** matrix:

$$\mathbf{d} = \mathbf{K}^{-1}\mathbf{F} \qquad\qquad \text{(Eqn 2.2.13)}$$

When the nodal displacements have been calculated, stresses and strains can be computed within each element accordingly:

$$\boldsymbol{\varepsilon} = \mathbf{B}\mathbf{d},$$

$$\boldsymbol{\sigma} = \mathbf{E}(\boldsymbol{\varepsilon} - \boldsymbol{\varepsilon}_0) \qquad\qquad \text{(Eqn 2.2.14a-b)}$$

The result of this solution is thereby displacement, strains and stresses for every element in the analysed geometry, but there is a range of specialised element types available in modern FEA software that allow for computation of thermal, electric, harmonic and many more DOF's.

2.2.2 Thermal FEA

Much in the same way as for the structural analysis described above, the mechanisms of heat transfer within a solid body can also be modelled using finite element techniques. For a purely thermal analysis the only DOF is temperature and consequently the state of a point is determined by the temperature T and heat flux $\mathbf{q}$. The solution derivation follows the same pattern with the problem initially formulated in a strong form that is consequently transformed into a weak form and then discretised into a matrix equation.

2.2.2 - a Strong Form

For the same generic body of volume V with a given internal heat supply Q per unit volume (Figure 2.6), find the temperature T such that the heat equation is satisfied:

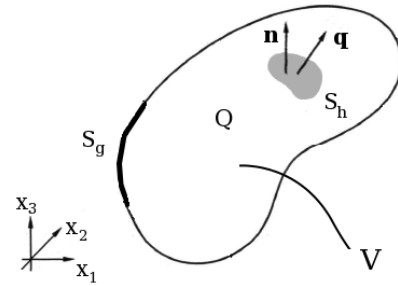$$\rho C_P \dot{T} + q_{i,i} - Q = 0 \qquad \text{in } V \quad \text{(Eqn 2.2.15)}$$

Figure 2.6. *Generic 3D body with thermal BC's*

With the boundary conditions:

$$T = g \qquad\qquad \text{on } S_g \qquad\qquad \text{(Prescribed boundary temperature)}$$
$$-q_i n_i = h \qquad\qquad \text{on } S_h \qquad\qquad \text{(Prescribed boundary heat flux)}$$

(Eqn 2.2.16a-b)

Alternatively to applying a direct value for the boundary heat flux as in equation 2.2.16b, a convection BC can be used that relates the heat flow to the temperature difference between the body surface T and the surrounding fluid T_b:

$$q_i n_i = h_f (T - T_b) \qquad \text{(Eqn 2.2.17)}$$

The convection is then controlled by the film coefficient h_f that depends on the materials and fluid flow conditions around the body. The heat flux is always defined perpendicular to the body surface which is why the surface normal vector **n** is used in the heat flux BC's.

Since equation 2.2.15 is time dependent, an initial condition is applied for the temperature as

$$T(\mathbf{x},0) = T_0(x) \qquad \text{(Eqn 2.2.18)}$$

The temperature and heat flux are related through Fourier's law of heat transfer which thus is the constitutive law of thermal FEA:

$$q_i = -D_{ij} T_{,j} \qquad \text{(Eqn 2.2.19)}$$

where D_{ij} are the material dependent thermal conduction coefficients [12].

1.1.1-a   Variational Formulation

Analogous to the weak formulation of the elastic problem, a similar integral equation can be formulated in the thermal case. The variational factor w is now one -dimensional and denotes a temperature variation in the variation space U according to:

$$\mathrm{U} := \left\{ w \,\middle|\, w = 0 \text{ on } S_g \right\} \qquad \text{(Eqn 2.2.20)}$$

The variational form can then be stated as: given Q find T such that the heat equation

$$\int_V \rho C_p \dot{T} w \, dV - \int_V q_i w_{,i} \, dV = \int_V Q w \, dV + \int_{S_h} h w \, dS \qquad \text{(Eqn 2.2.21)}$$

and

$$T(0) = T_0 \qquad \text{(initial condition)}$$

are satisfied $\forall\, w \in \mathrm{U}$ together with the thermal constitutive law (Eqn 2.2.19) [12].

2.2.2 - b Matrix Formulation

In the thermal case the basic vector valued properties are the heat flux $\mathbf{q}$ and the temperature gradient ∇T, closely related by the material conductivity matrix $\mathbf{D}$

$$\mathbf{q} = \begin{Bmatrix} q_1 \\ q_2 \\ q_3 \end{Bmatrix} \qquad \nabla T = \begin{Bmatrix} T_{,1} \\ T_{,2} \\ T_{,3} \end{Bmatrix} \qquad \mathbf{D} = \begin{bmatrix} k_{11} & k_{12} & k_{13} \\ & k_{22} & k_{23} \\ sym. & & k_{33} \end{bmatrix}$$

These are related through the following matrix-vector relations:

$$T = \mathbf{NT}; \qquad \nabla T = \hat{\mathbf{B}}\mathbf{T}; \qquad \mathbf{q} = -\mathbf{D}\nabla T \qquad \text{(Eqn 2.2.22)}$$

Where the element geometry is included in the $\mathbf{N}$ and $\hat{\mathbf{B}}$-matrices that contain the element shape functions, the vector $\mathbf{T}$ (not to be confused with the scalar T) contains the element nodal temperatures and δT the nodal temperature variations. Expressing the variational formulation with the relations from equation 2.2.21 then yields the following discrete set of matrix equations:

$$\delta \mathbf{T}^T \left(\int_V \mathbf{N}^T \rho C_p \mathbf{N} dV \dot{\mathbf{T}} + \int_V \hat{\mathbf{B}}^T \mathbf{D} \hat{\mathbf{B}} dV \mathbf{T} - \int_V \mathbf{N}^T Q dV - \int_{S_h} \mathbf{N}^T h dS \right) = \mathbf{0} \qquad \text{(Eqn 2.2.23)}$$

or in a more convenient matrix notation:

$$\mathbf{K}_{tb} \mathbf{T} + \mathbf{K}_{tc} \dot{\mathbf{T}} = \mathbf{F}_t \qquad (\mathbf{T(0)} = \mathbf{T_0}) \qquad \text{(Eqn 2.2.24)}$$

In relation to the elastic case the diffusion conductivity matrix $\mathbf{K}_{tb}$ is the thermal equivalent of the element stiffness matrix and is computed as:

$$\mathbf{K}_{tb} = \int_V \hat{\mathbf{B}}^T \mathbf{D} \hat{\mathbf{B}} dV \qquad \text{(Eqn 2.2.25)}$$

The transient nature of the heat flow is governed by the capacity matrix $\mathbf{K}_{tc}$, similarly constructed from the global shape function matrix $\mathbf{N}$ as:

$$\mathbf{K}_{tc} = \int_V \mathbf{N}^T \rho C_p \mathbf{N} dV \qquad \text{(Eqn 2.2.26)}$$

The applied boundary conditions are included the thermal load vector $\mathbf{F}_t$ that contains the supplied nodal heat:

$$\mathbf{F}_t = \int_V \mathbf{N}^T Q dV + \int_{S_h} \mathbf{N}^T h dS \qquad \text{(Eqn 2.2.27)}$$

The result from solving equation 2.2.24 is the temperature field over the body given the supplied boundary conditions and stating that the heat flux through the boundary surfaces equals the rate of change of thermal energy content in the volume plus internally generated heat.

2.2.3 *Thermoelastic coupling*

In cases where there are steep temperature gradients within a body, this can lead to internal strains being induced by thermal expansion in the material. This provides a thermoelastic coupling between temperature field and the elastic displacement field in a domain. This is in nearly all practical cases a one-way coupling in the sense that thermal loads induce elastic displacements by means of thermal expansion but displacements rarely affect the temperature of a body. For the general 3D case, this coupling means that thermal strains must be added to the elastic constitutive law – here presented in its final matrix form:

$$\boldsymbol{\varepsilon} = \mathbf{E}^{-1}\boldsymbol{\sigma} + \boldsymbol{\alpha}\left(T - T_0\right) \qquad\qquad \text{(Eqn 2.2.28)}$$

where $\boldsymbol{\alpha}$ is a matrix containing the material thermal expansion coefficients.

To incorporate this into the FE matrix calculations a thermal-structural coupling relation must be used. Applying the variational principle to the governing equations of elastic motion and heat flow conservation coupled by the thermoelastic constitutive equations, produces a direct coupling of the two fields. For a transient case with a strong coupling this expands the matrix equation to:

$$\begin{bmatrix} \mathbf{C} & \mathbf{0} \\ -T_o\mathbf{K}_{ut} & \mathbf{K}_{tc} \end{bmatrix}\begin{Bmatrix} \dot{\mathbf{d}} \\ \dot{\mathbf{T}} \end{Bmatrix} + \begin{bmatrix} \mathbf{K} & \mathbf{K}_{ut} \\ \mathbf{0} & \mathbf{K}_{tb} \end{bmatrix}\begin{Bmatrix} \mathbf{d} \\ \mathbf{T} \end{Bmatrix} = \begin{Bmatrix} \mathbf{F} \\ \mathbf{F}_t \end{Bmatrix} \qquad\qquad \text{(Eqn 2.2.29)}$$

where the thermoelastic coupling is controlled by thermoelastic stiffness matrix $\mathbf{K}_{ut}$ defined as:

$$\mathbf{K}_{ut} = -\int_V \mathbf{B}^T\mathbf{E}\boldsymbol{\alpha}\left(\nabla\mathbf{N}^T\right)dV \qquad\qquad \text{(Eqn 2.2.30)}$$

The structural damping matrix $\mathbf{C}$ governs the transient elastic behaviour of the material but need not be considered in this presentation since it is assumed that $\dot{\mathbf{u}} = \mathbf{0}$ for all analyses conducted in this project.

This type of direct coupling of the thermal and structural solutions allows for a solution to be achieved in a single solver iteration through inversion of equation 2.2.29. This is an important advantage to other coupling methods that require separate solver runs for the thermal and elastic solutions.

2.3   Cohesive Zone Material Modelling

Another specialised application of FEA is the analysis of adhesive layers and joints. Since the early days of practical computational engineering, studies have been made on how to calculate the stress distribution of adhesive layers [13] [14]. But the use of traditional FE-methods for analysing adhesive joints has been limited by the geometry, and the physical attributes of the adhesive layer making the analysis computationally cumbersome. The reason for this is that a relatively high number of elements in the thickness direction must be used, resulting in very large computation models and expensive, time consuming analyses. It can, however, be shown [15] that for a thin and soft adhesive layer the dominating stress and strain state is homogeneous through the thickness and governed by the shear and peel deformation modes. This means that the adhesive can be treated as a material surface, resulting in a more efficient model in terms of the adherends relative interface displacements.

In order to model the material behaviour of adhesives several specialised approaches have been presented. More than just looking at the local stresses in the adhesive, it is highly desirable to model the entire process of onset and propagation of the debonding of the joint until complete fracture occurs. The debonding of adhesive layers is mechanically closely related to the delamination of composite materials, where the composite resin yields and fails between two fibre layers. The increased use of composite materials in modern engineering has led to a corresponding increase in research and study of the mechanisms behind debonding and delamination and many of the methods developed are valid for use in both cases.

A number of these methods are based on Linear Elastic Fracture Mechanics (LEFM), which is the field of mechanics that regards the formation and propagation of cracks in engineering materials. When appropriate assumptions can be made of material non-linearities etc, computational LEFM methods have proved to work quite well for simpler delamination/debonding problems. The frequently used techniques include virtual crack closure (VCC), the contour integral methods, virtual crack extension and the stiffness derivative method.

2.3.1   *Basic Concepts of Fracture Mechanics*

The basic concept of fracture mechanics is the energy approach to crack growth, first proposed by Griffith as early as 1921 [16] and then refined by Irwin into its present form [17]. The central idea is the energy release rate, G, which is defined as the rate of change for the potential energy of the crack area and thus has the units of energy over area (J/m^2) [18]. The energies related to the growth of a crack in a material are mainly the free surface energy needed to create new free surfaces on the sides of the propagating crack and the strain energy stored in the loaded material. The original definition of the energy release rate is then the derivative of the potential energy, Π, with respect to crack area A:

$$G = -\frac{d\Pi}{dA} \qquad\qquad\qquad \text{(Eqn 2.3.1)}$$

The potential energy of the elastic material is in this context defined as the difference between the internal strain energy and the work done by external forces:

$$\Pi = U - F \qquad \text{(Eqn 2.3.2)}$$

The energy release rate can be seen as the driving force for crack growth, much like the applied stress for conventional elastic-plastic deformation. The material parameter that determines when fracture occurs, equivalent to the yield strength, is the critical energy release rate G_c, more often referred to as the fracture toughness or fracture energy of a material.

When applying LEFM in numerical methods the energy release rate is typically related to the local stress σ (force per unit area) and the node displacement δ at the crack tip, leading to the definition

$$G_c = \int_{}^{\delta_c} \sigma(\delta) d\delta \qquad \text{(Eqn 2.3.3)}$$

Also for a linear-elastic system, the implied stress-strain stiffness relation gives the value of σ as:

$$\sigma = E \frac{\delta}{\ell} \qquad \text{(Eqn 2.3.4)}$$

where ℓ is a characteristic length dependent on the specific problem geometry and mesh size used in the analysis. When fracture occurs, the value of σ falls to zero from a maximum value σ_{max} defined as a function of the material fracture toughness G_c. It should be noted here that it is G_c that is the defining fracture parameter and even though σ_{max} and ℓ influence the solution they are not material parameters as such.

2.3.2 *The Cohesive Zone Model*

A newer approach applicable to both cohesive and adhesive fracture is the *cohesive zone model* (CZM), which can be considered a generalised representation of the fracture failure criteria using two (or possibly three) material parameters. In the CZM fracture is described as occurring in a local process where the stress reaches a limiting value of σ_{max}. At this point a damage process occurs in which the stress decreases to zero before the actual fracture occurs at the critical displacement δ_c (see Figure 2.7).

The material properties defining this relation are the fracture toughness G_c, the maximal stress σ_{max} and then in some applications the shape of the traction-separation curve. The influence of the curve shape is of lesser importance and can be modelled as bilinear, quadratic or higher order depending on the numerical scheme used.
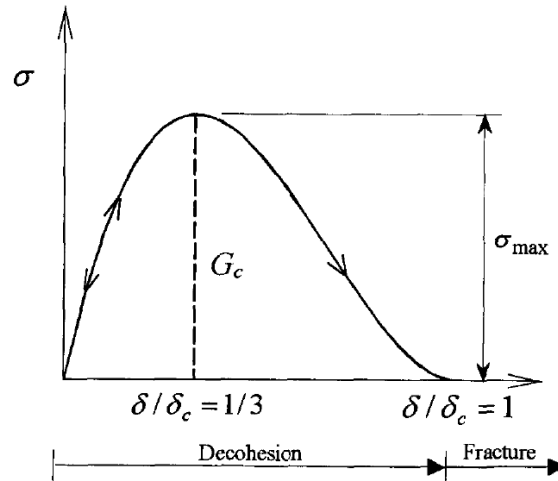
Figure 2.7. *Overview of the cohesive law relating the adhesive stress to the relative displacement.*

2.3.3 CZM *in ANSYS*

For this project, a CZM approach has been chosen for analysing the adhesive interfaces using the CAE software package ANSYS 11.0. Using CZM to analyse adhesive contact is available in ANSYS as a special case of regular contact analysis where a specially defined CZM material is used on the contact surfaces. The specific cohesive zone model implemented by ANSYS is based on the methods described by Alfano and Crisfield [19] and uses a mixed mode description to handle the different susceptibilities to fracture in mode I (normal) and mode II (shear) loading.

P = normal contact stress (tension)

K_n = normal contact stiffness

u_n = contact gap

$\bar{u}_n$ = contact gap at the maximum normal contact stress

u_n^c = contact gap at the completion of debonding

d_n = debonding parameter
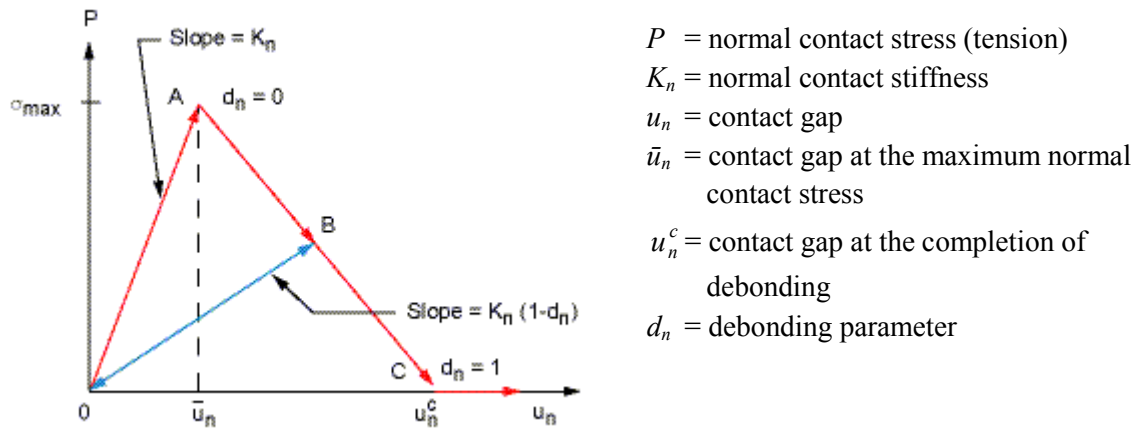
Figure 2.8. *The bilinear representation of the cohesive law used in ANSYS 11.0*

The traction-separation law is modelled as bilinear (Figure 2.8) consisting of a linear elastic loading part (O→A) followed by linear softening (A→C). The critical fracture energy is, as stated earlier, defined as the integral of the traction over the displacement; in this case (and ANSYS notation) giving:

$$G_{cn} = \int_0^{u_n^c} P du = \frac{1}{2} \sigma_{max} u_n^c \qquad \text{(Eqn 2.3.5)}$$

for mode I debonding and

$$G_{ct} = \int_0^{u_t^c} T du = \frac{1}{2} \tau_{max} u_t^c \qquad \text{(Eqn 2.3.6)}$$

for mode II debonding.

The debonding parameter describes the degree of debonding in a specific point and is for mode I loading defined as:

$$d_n = \left(\frac{u_n - \bar{u}_n}{u_n} \right) \left(\frac{u_n^c}{u_n^c - \bar{u}_n} \right), \qquad \text{subject to} \begin{cases} d_n = 0 & \text{when} \quad \dfrac{u_n}{\bar{u}_n} \leq 1 \\ 0 < d_n \leq 1 & \text{when} \quad \dfrac{u_n}{\bar{u}_n} > 1 \end{cases} \qquad \text{(Eqn 2.3.7)}$$

with only the subscript *n* differing from the mode II formulation. This allows for a formulation of the interface stress-displacement relation (see Figure 2.8) as:

$$P = K_n u_n \left(1 - d_n \right) \qquad \text{(Eqn 2.3.8)}$$

and

$$\tau_t = K_t u_t \left(1 - d_t \right) \qquad \text{(Eqn 2.3.9)}$$

for mode I and mode II debonding respectively.

2.3.3 - a Mixed Mode Debonding

For cases when the interface separation cannot be determined to be specifically dependent on either normal or tangential traction components a mixed mode debonding formulation is available. A redefinition of the debonding parameter is then necessary to account for both tangential and normal stress contributions:

$$d_m = \left(\frac{\Delta - 1}{\Delta} \right) \chi, \qquad \text{subject to} \quad \begin{cases} d_m = 0 & \text{when } \Delta \leq 1 \\ 0 < d_m \leq 1 & \text{when } \Delta > 1 \end{cases} \qquad \text{(Eqn 2.3.10)}$$

where

$$\Delta = \sqrt{ \left(\frac{u_n}{\bar{u}_n} \right)^2 + \left(\frac{u_t}{\bar{u}_t} \right)^2 } \qquad \text{(Eqn 2.3.11)}$$

and

$$\chi = \left(\frac{u_n^c}{u_n^c - \bar{u}_n} \right) = \left(\frac{u_t^c}{u_t^c - \bar{u}_t} \right) \qquad \text{(Eqn 2.3.12)}$$

The constraint on the contact gap ratio χ is automatically enforced in ANSYS by an appropriate scaling of the stiffness components.

Since both normal and tangential stresses contribute to the debonding this means that complete debonding occurs before either of the componential critical fracture energies are reached. To determine the completion of debonding, ANSYS uses a linear energy criterion defined as:

$$\left(\frac{G_n}{G_{cn}} \right) + \left(\frac{G_t}{G_{ct}} \right) = 1 \qquad \text{(Eqn 2.3.13)}$$

2.3.3 - b Artificial Dampening Parameter

The numerical analysis of a debonding process is complex and nonlinear and can result in convergence problems in the Newton-Raphson numerical solver ANSYS uses. A numerical artificial dampening is therefore included as a means of overcoming these difficulties. This parameter η has the units of time and is included in the numerical scheme with time step *t* as:

$$P_n = P_n^{final} + \left(P_n^{initial} - P_n^{final} \right) e^{\frac{t}{\eta}} \qquad \text{(Eqn 2.3.14)}$$

3. Analysis Methods

This chapter contains a thorough presentation of the methods that have been used when performing the research for this thesis. The aim is to include all relevant facts and parameters so a full validation of the analyses can be performed if necessary.

3.1 Obtaining CZM Material Parameters

A vital component of performing a successful FEA is to have an accurate description of the material one is analysing. This is achieved by selecting an appropriate material model (such as linear elastic or CZM) and using correct material parameters. Unfortunately, the material parameters required for a CZM-analysis (described in chapter 2.3.3) are not easy to obtain for a specific adhesive. Even though there are standardised test procedures defined to extract the critical fracture energies and maximum stresses, the results vary significantly with adherend material, surface treatment and other factors [20]. Searching the published literature, no single source could be found for all material parameters for the adhesive in question, Hysol EA 9394, and none regarding the specific adherend combination of titanium and CFRP.

The only first hand experimental test data available was from double lap joint specimens of quasi-isotropic CFRP and Ti 6Al-4V, performed by Swerea SICOMP AB in Piteå, Sweden, for the KOMET project. The experimental tests performed within the KOMET project were mainly focussed on identifying the influence of cryogenic temperatures on the adhesive bond strength by tensile testing of DLJ specimens where the adhesive overlap length and the temperature were varied to simulate different joints under space-like conditions.

For the time of determining the material parameters, only a small initial screening test was performed within the KOMET project. This was conducted at room temperature for three different overlap lengths (15, 50 and 100 mm) [21]. These tests were performed largely according to standard ASTM D3528-96 [22] and were as such simple tensile tests where a reaction force was measured as the specimens were axially loaded to failure in a testing rig. Unfortunately, this kind of test does not yield any specific results about the adhesive material as such, and can only be used for internal strength comparison in a set of specimens with different joint configurations.

Hence, it was decided to make FE-models of the different specimen configurations used in the tests and compare the results of the analyses to the experimental data from the screening tests. If the results were to differ too much from the test data the material parameters could then be adjusted to better fit the test data. The material properties found in the literature is here used as a well grounded starting point, but are then adjusted to provide parameters that are valid for the present configuration of adhesives and adherends.

Experimental attempts to obtain the mode II fracture toughness of EA-9394 have been performed and presented by Gunawardana [23] and Guess *et al* [20], both through performing an

end notch flexure (ENF) test where a specimen was loaded in 3-point bending to produce pure mode II stresses in the adhesive. The crack propagation was then continuously measured and a value of G_{IIc} was calculated from a relation between the applied load, geometry of the specimen and the crack length. The values presented in these reports were obtained from specimens of various material configurations; either of carbon or glass fibre composite laminates, Aluminium or, in the report by Guess *et al*, dissimilar adherends of CFRP and Aluminium. Even though specimens of Al/CFRP would be most similar to the material combination in the TED, those test specimens were reported to fail cohesively in the composite instead of in the adhesive which leaves the results unsuitable for use as a material property of the adhesive.

Gunawardana also conducts experiments to acquire the mode I fracture energy from a series of double cantilever beam (DCB) tests according to the ASTM D5528 standard. A precracked specimen was mounted as a cantilever beam and transversely loaded in the cracked end. The recorded crack propagation is related to the applied load and geometry and was used to calculate a value of G_{Ic}.

3.1.1 Specimen modelling

The symmetric geometry of a DLJ test specimen makes it very suitable for modelling using symmetry conditions and simplified stress assumptions. To take full advantage of this, the model used for the majority of the analyses is a 2D plane strain model with a longitudinal symmetry boundary condition in the mid-plane of the centre adherend (Figure 3.1). The dimensions are essentially those defined in the ASTM standard for DLJ tests, ASTM D3528-96 (See Figure 3.2), with an alteration of the adherend base thickness (T_1 and T_2) from 1.6 mm to 2 mm due to the thickness of the titanium plates used in the construction of the specimens.
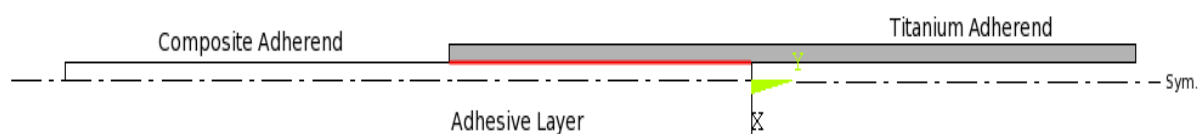

Figure 3.1. *Geometry of the 2D specimen model used in the FEA.*

The model geometry was meshed in ANSYS 11.0 with PLANE182, a 4-node structural solid element, and a base element size of 0.5 mm. The area around the adhesive zone was further refined to a mesh size of approximately 0.2 mm and then meshed with contact elements to simulate the adhesive layer (see Figure 3.3). Even though the adhesive in fact has a thickness of 0.2 mm it is in the FE-model defined as a zero-thickness cohesive zone, with 2-node CONTA171 contact elements on one adherend and corresponding TARGE169 target elements on the other. The physical behaviour of the adhesive layer thickness must therefore be corrected through the contact penalty stiffness parameters K_n and K_t.
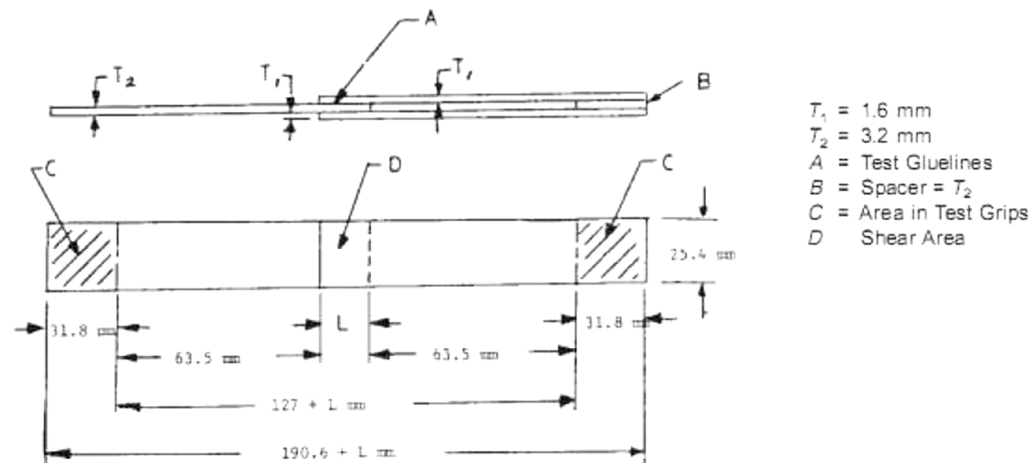
Figure 3.2. *Double lap joint test specimen according to standard ASTM D3528-96*

Once the model was set up and meshed, the boundary conditions (apart from symmetry) were simply applied as a zero displacement on the CFRP adherend end face and a prescribed displacement of 0.7-1 mm to the other end face. This is of course a simplification to the real world scenario with hydraulic grips holding the specimen, but was initially deemed sufficient since the main point of interest was the adhesive area in between.
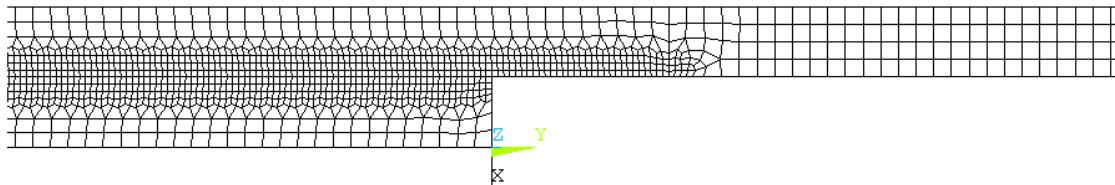

Figure 3.3 *Close up of the mesh around the end-point of the adhesive contact layer of the 2D specimen model.*

The CONTA171 element is not exclusively a cohesive zone element and can be used to simulate a variety of contact conditions of which bonded contact with CZM materials is a special case. It is a 2-node element that is overlaid on an existing solid, shell or beam element face and share nodes and geometry with these "parental elements" (see Figure 3.4). To define the cohesive debonding behaviour in ANSYS, first a CZM material has to be defined through the `TB` command with the `CZM` label. This material data table contains the values of the maximum stresses, fracture energies and the artificial damping coefficient of the material. Secondly the selected interfaces are meshed with contact and target elements using the `ESURF` command and with the CZM material activated. The bonding properties are set through the element `KEYOPTs` and finally the penalty stiffnesses can be adjusted through setting the `REAL` constants related to the contact elements. Target elements are meshed with `ESURF` in the same manner as the contact elements but do not require any additional settings.
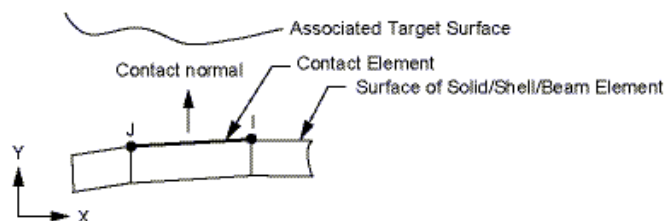
Figure 3.4. General illustration of the CONTA171 element geometry.

When a solution is done, the contact elements output data gives information about the local stresses and displacements in the adhesive layer. In addition to numerical list data, graphical contour plotting is available directly in the ANSYS graphical user interface (GUI) of stresses and relative displacements in both the normal and tangential directions. The local nodal values of the debonding parameter and normal and tangential fracture energies are also available but only as numerical lists.

3.1.2 Testing Procedure

To find suitable values for the material parameters and to gain an understanding of their influence of the overall results a series of tests was set up using the Design of Experiments (DOE) methodology. Designed experiments are widely used in the quality work in many industries as a way of systematically investigating the variables affecting a certain product or process and in this way direct improvement actions to where they are most needed. By designing the experiments before they are executed, the number of tests can be reduced and a more efficient analysis of the variables and their interactions is possible.

Table 3.1 *Parameters influencing the CZM analyses*

Material Parameters	Modelling Parameters
Maximum normal stress – σ_{max}	Adherend Shape – Straight/Tapered
Critical fracture energy, mode I – G_{Ic}	Contact Algorithm – Penalty/Aug. Lagrange
Maximum tangential stress – τ_{max}	Contact Surface – Ti/CFRP/Symmetric
Critical fracture energy, mode II – G_{IIc}	Nonlinear Geometry – On/Off
Normal contact penalty Stiffness – K_n	Element Order – High/Low
Tangential contact penalty Stiffness – K_t	-
Artificial dampening coefficient – η	-

Since a large number of variables affect the result of the adhesive specimen analysis, it was decided to first split them into two groups – material parameters and modelling parameters. Separate DOE matrices were constructed for the groups with the assumption that there were no cross-interactions between them. Since running the analysis and extracting the data is tedious and time-consuming, further steps were taken to minimise the number of runs by leaving

out specific parameters that were known either to be of little significance to the results or not to have any coupling effects with other parameters in the group.

From the material parameters listed in Table 3.1 G_{Ic}, τ_{max} and G_{IIc} were chosen to be included in the DOE test matrix. Since the specimens were only loaded in tension, the tangential parameters were considered of highest importance, and only single screening runs were made with the other parameters changed to verify their low impact on the results. Likewise, for the modelling parameters, an initial set of screening runs showed that the choices of contact solver algorithm and contact surface as well as the use of the nonlinear geometry were the most influential factors on the outcome, and these were selected for further testing.
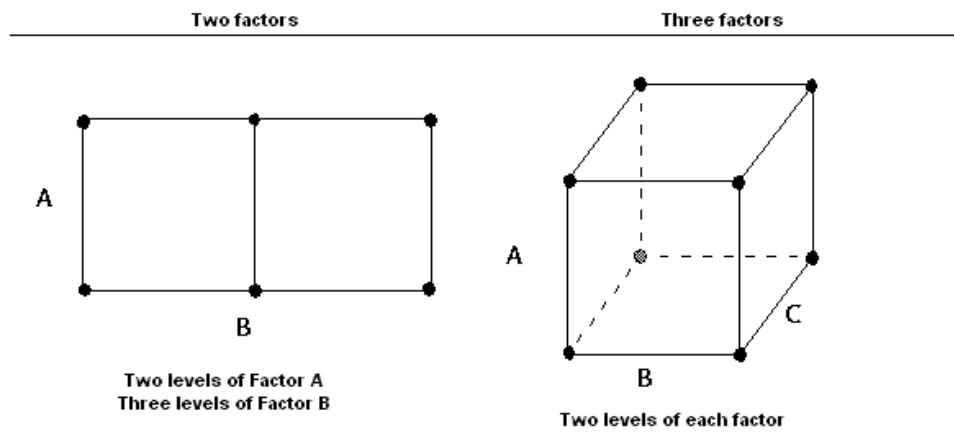

Figure 3.5. *Illustration of the "response spaces" created by DOE experiments.*

In order to thoroughly examine these selected parameters, a design matrix was constructed for each of the parameter groups. For the material parameters with numerical values a two-level full factorial design was chosen. For the modelling parameters a general full factorial design was preferred in order to include the three levels of the contact surface factor. In full factorial designs, responses are measured at all unique combinations of the factor levels which makes it possible to draw conclusions of the response interaction between the factors. That is, if level of one factor affects the response of another. Each factor in a design can be seen as a separate dimension in a "response space" where the functional values are the resulting response parameters. Three factors in two levels thus create a 3D box with one test response in each corner (see Figure 3.5). For the factors included in these designs, this means a total of 2^3 runs were needed for the material parameters and $2\times2\times3 = 12$ runs for the modelling parameters.

3.2 2D-axisymmetric TED Analysis

The next phase in the project is to use the adhesive material characteristics obtained in the previous phase and use them in a model of the actual TED geometry. Due to the rotational symmetry of the flange the geometry is well suited for a 2D axisymmetric model where only a radial cross section of the full geometry is modelled. This leads to a much simpler model with vastly reduced computation times for the solutions as only a fraction of the elements of a full 3D are needed and with fewer DOFs. The restriction is that only axisymmetric loads can be applied to the model[1], which is a limitation when analysing the rather complicated load case of the TED.

3.2.1 *Simplified Geometry from Preliminary Study*

Within the KOMET project a preliminary study of the stress distribution in the adhesive joints of the TED was performed at a relatively early stage. In this study the adhesive layer was fully resolved with elastic 2D elements in simplified axisymmetric geometry. Thermal and structural loads were then applied in two load cases to simulate the forces acting on the TED during engine test runs.

The first objective for this project is to reproduce the simulations that were performed in the preliminary study but with using CZM elements to model the adhesive layer. By using a more specialised tool for analysing adhesive debonding, further conclusions can hopefully be drawn about the actual effect on the integrity of the joint caused by the stresses observed in the purely elastic model.
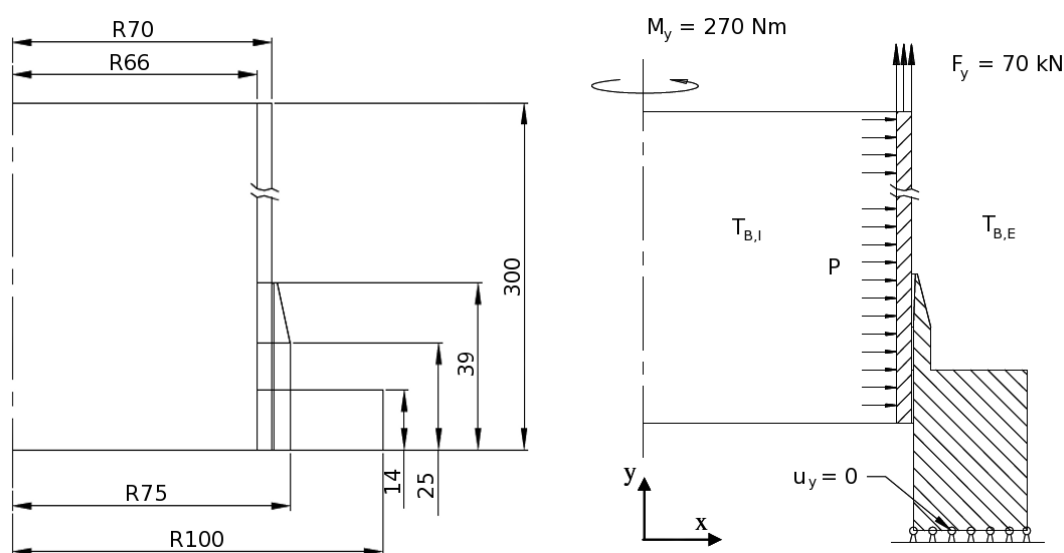

Figure 3.6. *Basic measurements and BC's for the initial 2D axisymmetric TED model.*

---

[1] Non-axisymmetric loads can in fact be applied in ANSYS by using special elements and expressing the load as a Fourier series of harmonic functions. This was however not deemed practical for this study.

The geometry used to represent the TED simply consists of a straight composite tube adhesively attached to the inside of a solid titanium flange (see Figure 3.6). The measurements largely represent those of the actual TED inlet section regarding flange and inlet inner and outer diameters. To incorporate the stiffness of the opposite interface flange (not included in the model) an extension of the flange geometry is made in the axial direction. This extension is then locked in the axial direction with zero-displacement boundary conditions.

The TED is analysed for two load cases, each representing an engine test sequence, where the magnitude and nature of the loads are specified by VAC in an initial testing specification [24]. The first case simulates the cooling of the components down to cryogenic temperatures before engine start with the objective to quantify the stresses induced in the material from the internal temperature variations. The cooling process is rather slow and can thus be considered as steady-state to further simplify the analysis. The second load case is a simulation of the actual operation of the engine and consists of a longer transient sequence where time-dependent functions of internal pressure, temperature and film coefficient are set up.

3.2.1 - a Load Case 1
The cooling load is achieved by setting thermal convection boundary conditions (Eqn 2.2.17) on the internal (facing the origin in Figure 3.6) and external surfaces (facing away from the origin) of the model. Rigid body motion is restricted by locking the stiffness flange in the Y-direction. Parameter values for the thermal BC's are presented in Table 3.2.

Table 3.2 *Load case specification for static cryogenic case (Load Case 1)*

Parameter		Value
Internal Fluid (Bulk) Temperature	$T_{B,I}$	40 K
Internal Film Coefficient	$h_{f,I}$	20 W/m^{2}K
External Fluid (Bulk) Temperature	$T_{B,E}$	313 K
External Film Coefficient	$h_{f,E}$	20 W/m^{2}K

3.2.1 - b Load Case 2
The second load case is much more complex and involves both structural and thermal loading as functions of time. The entire load sequence is about 514 seconds long and essentially consists of a short cooling phase followed by two subsequent engine runs. The effect of running the engine is a highly pressurised flow of hydrogen gas through the TED which results in a steep increase in internal pressure and film coefficient. In addition to these effects there are static structural forces and moments acting on the component throughout the load sequence. The full range of loads and BC's applied is presented in Table 3.3.

Table 3.3. *Load case specification for the transient operation case (Load Case 2)*

Parameter		Value
Internal Pressure	P	See Table 3.4
Internal Fluid (Bulk) Temperature	$T_{B,I}$	See Table 3.4
Internal Film Coefficient	$h_{f,I}$	See Table 3.4
External Pressure	P_E	0 Pa
External Fluid (Bulk) Temperature	$T_{B,E}$	293 K
External Film Coefficient	$h_{f,E}$	20 W/m²K
Axial Force	F_y	70 kN
Axial Torque	M_y	270 Nm

Simplified time dependent functions for the internal transient loads are specified in Table 3.4. Note that according to the specifications the load sequence starts at time t = -20 *s*, a separate time scale that is offset 20 seconds is used for the FE-analyses. In future reference the FEA time scale is used if nothing else is stated.

Table 3.4 *Specification of time-dependent load parameters for Load Case 2*

FEA Time [s]	Specification Time [s]	Internal Pressure [MPa]	Internal Bulk Temperature [K]	Internal Film Coefficient [W/m²K]
0	-20	0.64	260	274.6
20.6	0.6	0.69	260	298.9
22.4	2.4	7.68	205	22214
238.4	218.4	7.95	212	22639
244.4	224.4	0.7	127	594
259.4	239.4	0.29	162	158.7
409.3	389.3	0.68	196	422
415.3	395.3	0.27	177	190.2
424.3	404.3	8.07	211	23343
490.3	470.3	8.11	213	23269
499.3	479.3	0.91	165	707.5
514.3	494.3	0.3	182	146.2

For better overview the values from Table 3.4 are plotted as functions of time and presented in Figures 3.7-9 below.
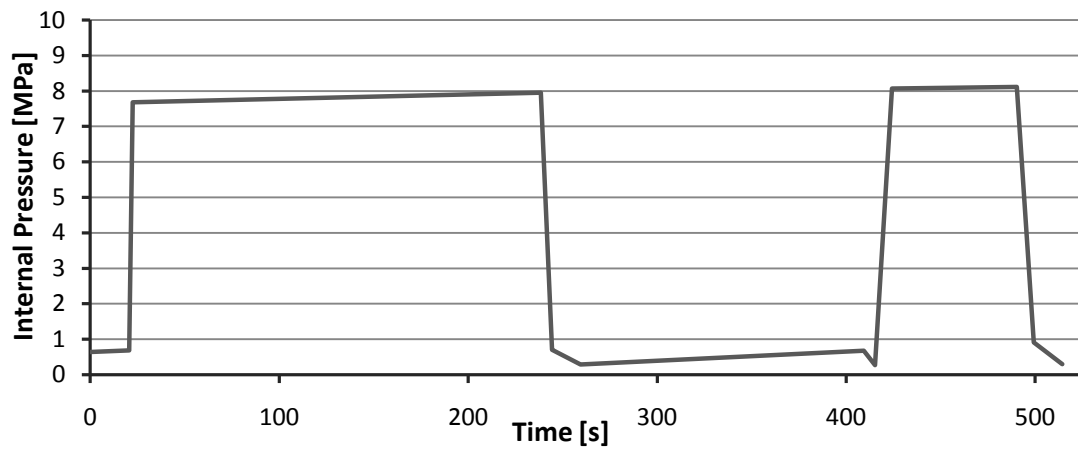
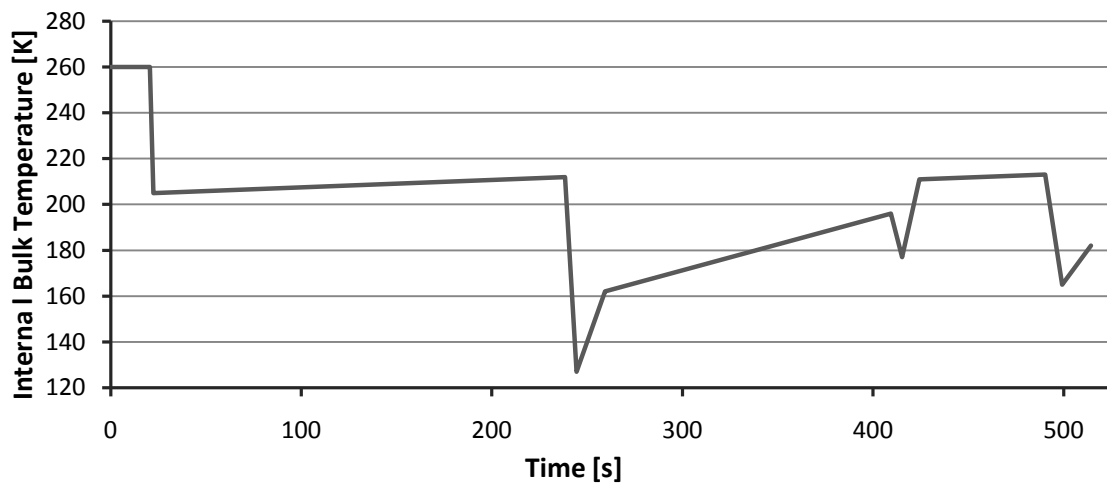Figure 3.7. *Internal pressure during Load Case 2 plotted as a function of time*

Figure 3.8. *Internal fluid temperature during Load Case 2 plotted as a function of time.*
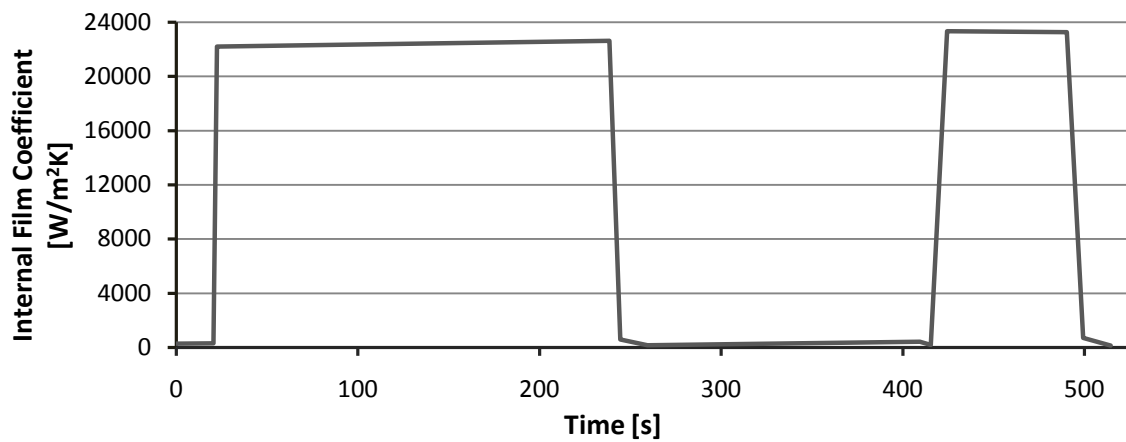

Figure 3.9. *Internal film coefficient during Load Case 2 plotted as a function of time.*

3.2.2 Setup of the Finite Element Analysis

Both of the load cases described above require thermal-structural coupled-field analyses where the temperature distribution leads to internal strains through the thermal expansion coefficient. ANSYS provides a number of methods for solving multi-field problems and in this case the use of specialised multi-field elements was considered the most suitable. The titanium flange and composite tube were both meshed with PLANE223 element set up for thermal-structural coupled field analysis (see chapter 2.2.3). The PLANE223 is a quadrilateral plane solid element with midside nodes and the extra number of nodes and integration points allowed for using a somewhat coarser mesh than in the earlier test specimen analyses. An adequate initial mesh size, capable of capturing the relevant stress concentrations, was decided to be 1 mm, with a refinement down to 1/3 mm in the adhesive contact zone[2]. The adhesive zone was meshed with contact and target elements in the same fashion as described in chapter 3.1.1, with the exception that the three-node CONTA172 element was used instead. The contact elements are fully compatible with coupled-field analyses and the thermal contact behaviour is controlled in ANSYS by the thermal contact conductance (TCC) parameter. The conductive heat flux between two surfaces in contact is defined by

Figure 3.10. *The meshed geometry of the 40 mm overlap joint from the preliminary study. Red line marks the application of CZM elements.*

$$q = TCC\left(T_t - T_c\right) \qquad \text{(Eqn 3.2.1)}$$

where T_t and T_c are the temperatures of the target and contact surfaces respectively. The value of TCC was derived from the conductivity value of an epoxy-like adhesive and the proposed thickness of the adhesive layer t_a according to the relation:

$$TCC = \frac{k_{xx}}{t_a} \qquad \text{W/m}^2\text{ K} \qquad \text{(Eqn 3.2.2)}$$

The value of the TCC-parameter is entered in the set of REAL constants in the same way as for the contact penalty stiffnesses.
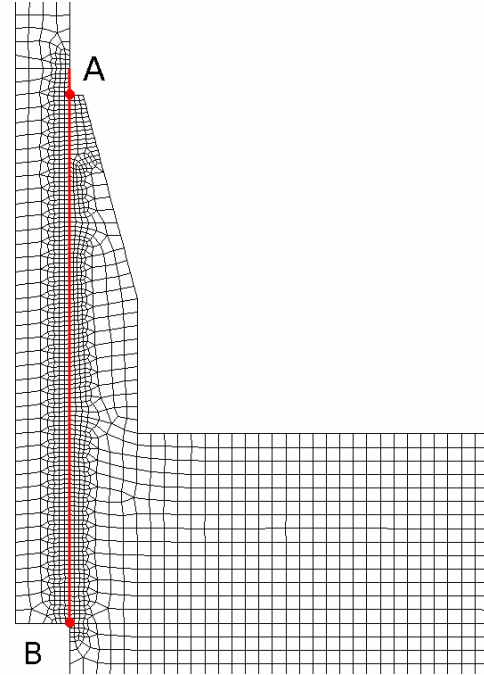
---

[2] Schmidt P. Linköping University, Private communication, March 1 2010

When fully meshed, convection BC's were added to the nodes on the internal and external faces of the model using the load data from Table 3.4. For the transient analysis additional loads were added in form of a time-dependent pressure on the internal face of the composite tube, an axial force (applied as a negative pressure on the top surface) and a structural moment about the central Y-axis. The moment was applied on the top surface nodes through a master node located on the Y-axis with rigid connections out to each node on the top surface of the tube. The moment could then be applied to the master node and proportionally transferred out to the surface via the rigid connections.

3.2.3 Material Data

A TED of a metal-composite hybrid design is initially specified to be constructed from Ti 6Al-4V (titanium alloy with 6% aluminium and 4% vanadium) and a carbon fibre composite consisting of T700 medium module carbon fibres in an RTM-6 epoxy matrix. Detailed temperature dependent data for forged Ti 6Al-4V was available from the materials department at VAC [25], and could readily be imported into ANSYS. The material data for the CFRP and the EA9394 was assumed to be the same as used in the preliminary study, with CZM-parameters for the adhesive taken from the results of the specimen analyses (see chapter 4.1.2). The material data used for the analysis is presented in Table 3.5.

Unfortunately, no valid temperature dependent material data could be obtained for the CFRP. This of course affects the results, but not necessarily in any significant way since the material properties in the in-plane directions are mainly governed by the properties of the carbon fibres, which are relatively insensitive to temperature changes.

Table 3.5 Material data parameters

Parameter		T700/RTM-6 CRFP (orthotropic)	EA 9394	Units
Elastic Modulus	$E_x / E_y / E_z$	10.1 / 52.9 / 52.9	4 / - / -	GPa
Poisson's Ratio	$v_{xy} / v_{yz} / v_{xz}$	0.056 / 0.317 / 0.056	0.3 / - / -	-
Shear Modulus	$G_{xy} / G_{yz} / G_{xz}$	3.69 / 20.1 / 3.69	- / - / -	GPa
CTE	$\alpha_{xx} / \alpha_{yy} / \alpha_{zz}$	56.1×10^{-6} / 3.8×10^{-6} / 3.8×10^{-6}	69×10^{-6}	K^{-1}
Spec. Heat Capacity	C_p	900	1340	J/kgK
Density	ρ	1528	1150	kg/m^3
Thermal Conductivity	$k_{xx} / k_{yy} / k_{zz}$	0.78 / 5.54 / 5.54	0.24	W/mK
Max. Contact Stress	$\sigma_{max} / \tau_{max}$	- / -	44.5 / 40	GPa
Crit. Fracture Energy	G_{Ic} / G_{IIc}	- / -	425 / 2000	J/m^2
Contact Stiffness	K_n / K_t	- / -	2×10^{13} / 1×10^{12}	N/m^3

3.2.4 Joint Geometry Concepts

In comparison to the actual geometry of the TED inlet, it is clear that there have been severe simplifications made when generating the flange geometry analysed in the preliminary study

and the previous section of this report. One of the aims of this project is to extend the analysis to more realistic and technically feasible joint and flange geometries so that more accurate and precise conclusions can be made on the matter of a composite TED design. In the following section the cross-sectional geometry of the adhesive joint is examined and revised to produce a joint concept that satisfies the high demands of the structure.

As a result of the extreme operating conditions of the TED, with high pressures and steep temperature gradients, a number of requirements must be fulfilled to assure functionality:

> ➢ Smooth inner surface – Aerodynamic design of inner surface cannot be altered
> ➢ Metallic flange contact – Required for maintaining high sealing capacity of the flange
> ➢ Preservation of flange geometry – No alterations to adjacent components
> ➢ Sufficient load-bearing capabilities – Must withstand specified operational load cases

Most notably, there is no room for long adhesive joints in the TED inlet cross section due to the curved shape of main flow chamber. Since it is highly undesirable to alter the present geometry of the TED, a first step would be to reduce the joint overlap length of the joint to one that can be accommodated within the present inlet geometry. Upon inspection of the original TED drawings it was decided that a straight overlap length of no longer than 25 mm could be allowed for. If the joint were to be tapered however, a somewhat longer overlap length could be fitted. Figure 3.11 shows a cross section of the actual TED geometry where suggested alterations to fit an axisymmetric metal flange have been marked in red. Note that it is a fully tapered joint geometry that is pictured on the drawing.
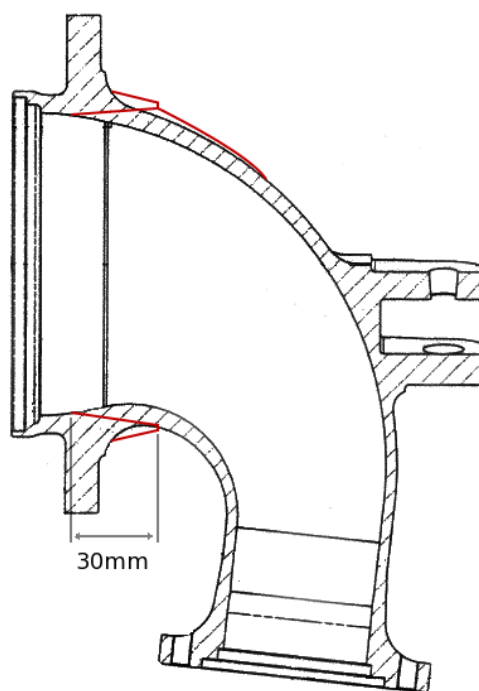

Figure 3.11. *Cross sectional drawing of the TED with a suggested flange geometry added in red.*
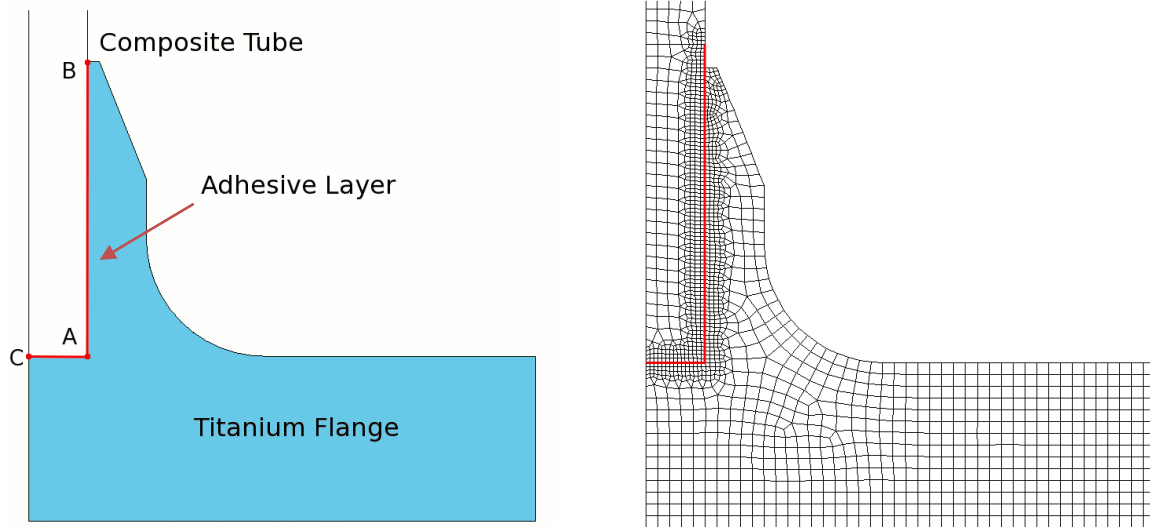
Figure 3.12. *The embedded straight end joint geometry concept overview (left) and mesh (right).*

To retain the original flange geometry with a protruding inner interface connecting to the turbine stator and a smooth inner surface, a tubular joint where the compose tube is integrated into the metal flange is needed. Two initial geometry concepts, labelled Embedded Straight End and Short Tapered End, were generated to overcome these problems. The common feature is that a large portion of the joint remained axially straight to resemble the previous overlap joint (see Figure 3.10) while the end surface of the composite tube are treated differently. On the outside titanium flange a corner fillet was also added to better correspond to the original design, and to remove the stress concentrations arising in the sharp corner.
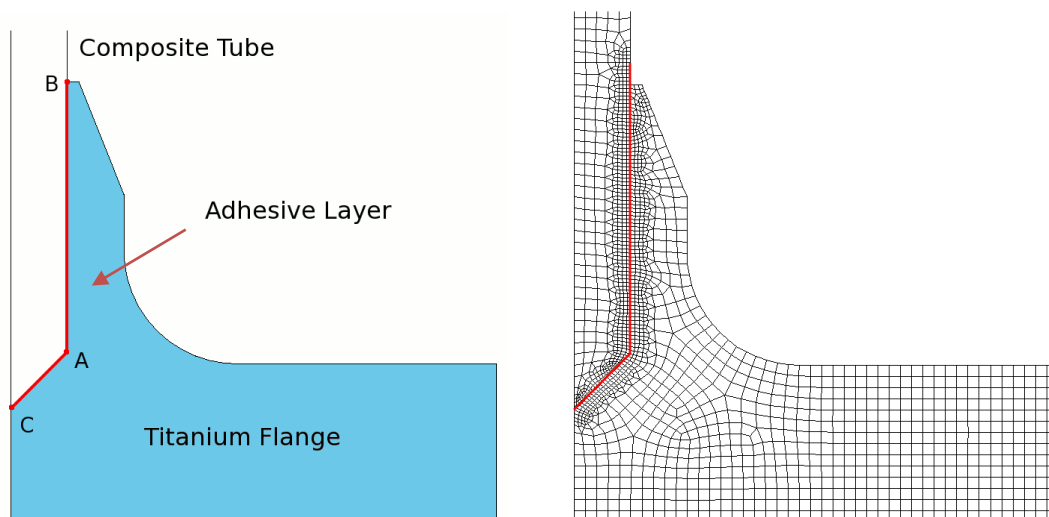

Figure 3.13. *The short tapered end joint geometry concept overview (left) and mesh (right).*

Another common alternative to using a simple tubular lap joint is the tubular scarf joint where the adherend is tapered to a conical shape. Although technically weaker in axial loading, it provides a radially more compact joint geometry suitable for the application in question. In addition, this type of joint has advantages when it comes to assembly since a correct bonding pressure can be easier applied during the curing of the adhesive[3]. Note that the sharp end surface of the composite tube is not meshed with contact element as its load bearing capabilities are negligible. For test documentation purposes, this concept was named Fully Tapered End Geometry.
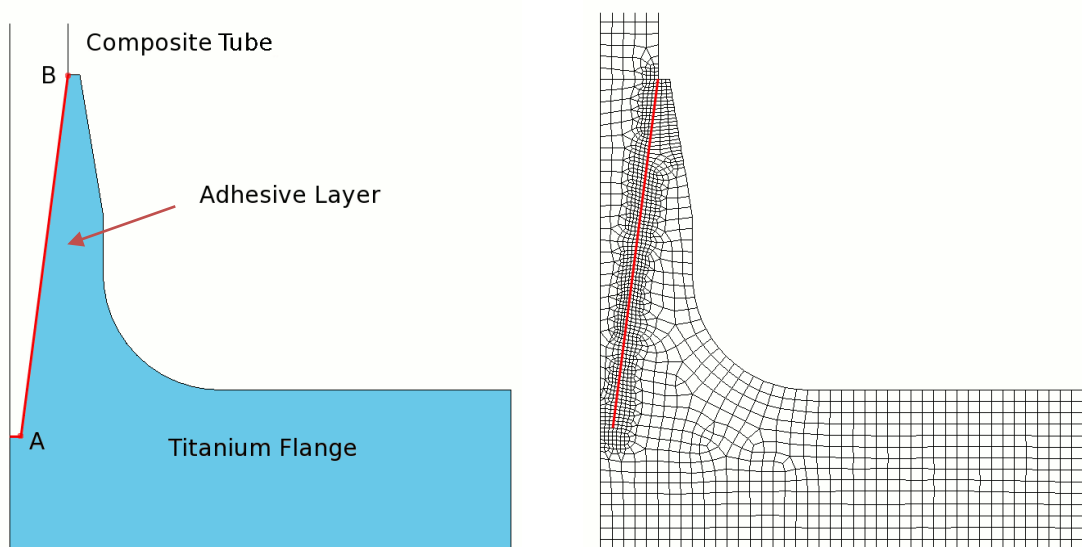
Figure 3.14. *The fully tapered end joint geometry concept overview (left) and mesh (right).*

These three geometry concepts were modelled and analysed, following the exact same description as for the original axisymmetric geometry above in order obtain comparable results. The geometry providing the most favourable stress distribution could then be further analysed in a three-dimensional load case.

---

[3] Johansson S. ACAB, Private communication, March 15 2010

3.3 Three-Dimensional TED Analysis

For the axisymmetric analyses, the structural loads on the component were simplified into a tensional axial force and a rotational moment, but in reality fully three-dimensional sets of loads are specified for all TED interfaces at different operational conditions. In the load specification used for structural robustness analysis of the current TED design [26], static structural loads are specified for the three flanged interfaces of the TED (inlet, main outlet and by-pass outlet) with the structural fixation set to the external engine support interface. This load case is designed as a combined weighting of the loads experienced under engine operation in four different flight modes and should thereby be sufficient for fairly reliable analysis of the adhesive joints. For previous structural analyses of the present TED design cast in Inconel 718 a complete FE-model of the TED had already been made by VAC, including mesh and applied loads according to Snecma's specification. The model was made available for use in this project as a source for extracting a 3D load case.

Since a three-dimensional analysis generally is far more computationally intensive than a 2D axisymmetric equivalent, it was highly prioritised to keep the computational costs at a minimum to make the analysis times manageable. For this reason it was decided not to model an entire composite TED geometry. Instead just the flange and surrounding composite material would be included and cut plane loads extracted from the existing full Inconel 718 3D model would be applied to the free cut surfaces . The result would be a fairly simple axisymmetric geometry with a 3D load case representing the response of the full TED geometry.
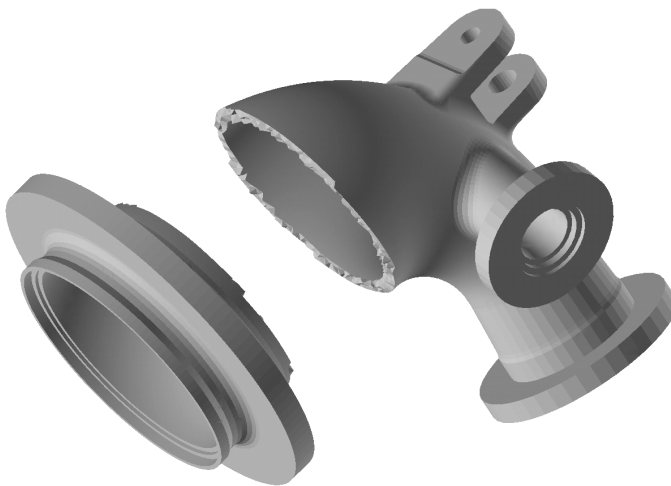

Figure 3.15. *The axisymmetric part of the TED geometry separated to illustrate the cut plane used for load extraction.*

3.3.1 Load Extraction

The loads used for the analysis of the flange were extracted as the reaction loads observed when locking the full FEA-model at the position of the cut plane. In order to cut off a reasonably axisymmetric part of the flange geometry, the distance from the flange bottom surface to the cut plane could not be longer than 48 mm (See Figure 3.15). At this distance in the full Inconel model, all nodes in a plane parallel to the flange surfaces were rigidly connected to a master node in the centre of the tube that in turn was fully constrained in both translation and rotation. After these alterations had been made to original script file, the analysis was run with appropriate loads applied to the other interfaces and after running the solution the reaction force on the master node in the cut plane could easily be extracted.

3.3.2   3D Modelling

The 3D FE-model that was prepared for the analysis of the cohesive joints was, as mentioned earlier, fully axisymmetric and was modelled by simply sweeping the earlier used 2D geometry 360° around the central axis. To keep the total number of elements down the global element size was set to 2.5 mm for the initial analysis, with no additional refinement at the bonding area. The mesh was designed as a mapped swept mesh where the original 2D cross sectional area was initially meshed with temporary MESH200 elements that were expanded into SOLID186 (structural) or SOLID226 (thermal-structural) during the rotational sweep operation. This resulted in two separate bodies (flange and composite tube) that were connected with CONTA174 area contact elements at the adhesive interface (see Figure 3.16). Element properties and capabilities as well as material properties are in all relevant aspect the same as for their 2D counterparts described in chapter 3.2.2-3.

On the top surface (i.e. the cut plane) of the composite tube, all nodes were constrained with rigid connections to a central master node, in the same way as for the load extraction. On this central node was then applied the force and moment vectors extracted from the full 3D model. Note that all values had to be multiplied by -1 to convert them from reaction forces to loads on the opposite surface.
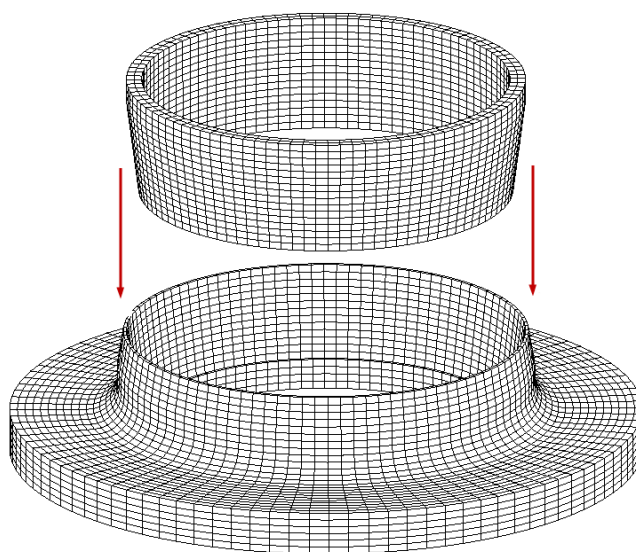

Figure 3.16. *The two bodies forming the coarse mesh full 3D model.*

The first step when the load had been extracted and applied was to run an initial static analysis on a mesh of purely structural elements to verify that the load were applied correctly and that the adhesive joints could handle e.g. the strong bending moments that were now present. Secondly, a larger transient analysis was made where the 3-dimensional static structural loads where applied together with the time-dependent thermal convection and internal pressure loads for the transient 2D analyses presented in chapter 3.2.1.

3.3.3   Submodelling

The coarse mesh of the initial 3D Flange model resulted in that the local stress concentrations in the adhesive layer could not be fully resolved by the CZM-elements. The main purpose of that analysis was thus to identify regions of the mesh and points in the time where high stress levels are encountered, rather than to quantify the effects on the adhesive layer. To further analyse these specific points of interest a cut-boundary displacement submodelling technique was utilised.

A sector of 50° centred on what was identified from the coarse model results as the most critical stress concentration was cut out and "submodelled" as a separate FE model with a much finer mesh in order to fully resolve the stress concentration. The cross-sectional mesh was refined around the adhesive layer before sweeping, creating fine quadratic mesh on the contact surface (see Figure 3.17). Similar to the load extraction technique described above, submodelling is based on Saint-Venant's principle stating that, if the actual force distribution is replaced by a statically equivalent system, the stress and strain distribution is altered only in the region near the load application. This implies that as long as the boundaries are far enough away from the stress concentration, reasonably accurate results can be obtained even if the stress effects are the result of a specified displacement on the submodel boundary instead of a complex global force distribution [27].
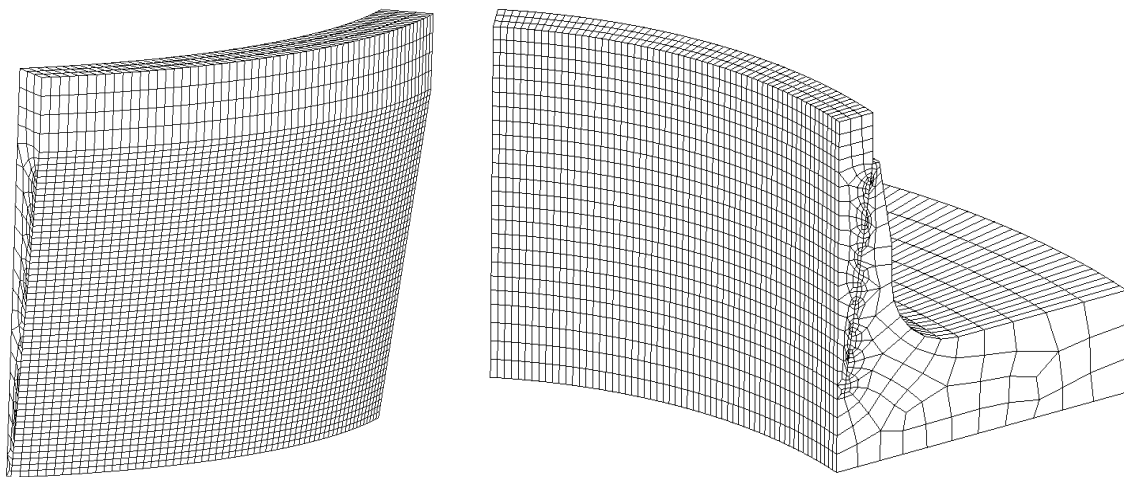

Figure 3.17. The finely meshed geometry of the submodel. The contact mesh is seen on the composite tube section to the left and the cross-section mesh is shown in the full model to the right.

Apart from creating the models and running the analysis solutions, there are three essential steps associated with performing a submodel analysis in ANSYS:

1. Identify cut-boundary node data from submodel and write it to file.
2. Perform DOF interpolation using the written nodal data with the result from the coarse model analysis.
3. Apply the interpolated nodal DOF displacements as boundary conditions on the submodel.

To incorporate the thermal loads in the submodel analysis, a similar extraction was made of the temperature at the point in time where the highest stress value was recorded. The temperature data was then applied as a body load instead of a boundary condition onto the submodel. Together, the thermal and structural loads provide a set of boundary and body load conditions that almost exactly correspond to the forces applied to the original model, and create the same conditions that gave rise to the original stress concentration.

3.4 Analysis of Cryogenic Properties

When the bulk of the analysis work that makes up this report was performed, Sicomp had not yet released their report on the tensile tests performed under cryogenic conditions (-150°C) and those results where thus not taken into consideration when performing the analyses described above. When they were published however, they showed such a significant decrease in bond strength that further tests had to be made to evaluate the impact of cryogenic material properties on the strength of the TED adhesive joints.

Before any FEA could be done to simulate this behaviour, an analysis of how the material parameters are affected by extremely low temperatures was needed. Reports on material properties of structural adhesives in cryogenic conditions are rare, but there has been some relevant research done on the subject. Much research has been done on composite fuel tanks for storing LOX and LH2 fuel in space applications and scientific tests have been made of the cryogenic strength of both the composite material [28] [29] [30] as well as different adhesives [31] [32]. Relevant for the TED application, the strength of metal to composite adhesive joints have been studied for both Ti 6Al-4V and CFRP adherends [33] and aluminium and CFRP [34] adherends.

As for the properties of carbon fibre composites, it can clearly be concluded that the material becomes stronger but stiffer when it is cooled to cryogenic temperatures. However, nearly all tests published are of unidirectional laminates and the results are not trivially translatable to the quasi-isotropic laminate that is proposed for the TED. There is also a temperature dependence of other material parameters such as the thermal expansion coefficient that needs to be considered, but again uncertainties of the impact on specific composite lay-ups make these values difficult to implement.

Table 3.6. *Compilation of bond strength reduction of EA9394 joints in cryogenic environment.*

Test	Adhesive	Adherends	Overlap	Strength RT -> CT
Shimoda	EA 9394	IM7-UD	15mm	-20%
Shimoda	EA 9394	T300-UD	15mm	-40%
Shimoda	EA 9394	Al	12,7mm	±0%
Shimoda	EA 9394	T300-UD	12,7mm	-33%
Shimoda	EA 9394	IM7-UD	12,7mm	-10%
Graf	EA 9394	IM7-QI	31,8mm	-10%
Sicomp	EA 9394	Ti6-4/T700-QI	15mm	-55%
Sicomp	EA 9394	Ti6-4/T700-QI	100mm	-60%

The published data on adhesive properties are considerably ambiguous. For DLJ tensile tests using the EA 9394 adhesive, Graf *et al*. showed only a minimal decrease in strength (<10%) while Shimoda *et al*. showed mixed results ranging from a slight increase to a 40% decrease in bond strength, depending on the adherend materials. The final results from the Sicomp study unanimously show a sharp decrease of bonding strength with 55-60% [35]. A compila-

tion of the approximate bond strength reductions seen in published results from DLJ tensile tests using EA 9394 is presented in Table 3.6

3.4.1 Estimation of Cryogenic Material Parameters

In order to attempt to reproduce these results in an FEA-analysis, further understanding of how specific material parameters are affected by cryogenic temperature was required. Shimoda *et al* also performed standardised (JIS K 7086) ENF-tests for obtaining mode II fracture energies (G_{IIc}) using a specimen with CFRP adherends bonded together with AF163-2K (3M), which is a 0.2 mm toughened epoxy adhesive film. The result of the ENF test was that the average critical fracture energy was lowered with almost 60%. The same report also shows an 80% decrease in "mode I rupture energy" according to an ASTM D-5041 cleavage test using the same material configuration as before.

Kang *et al* have performed extensive tests on three types of adhesives (FM 73, Bondex606 and
EA 9696) in bulk form as well as in aluminium-adherend DLJ specimens. In contrast to the other reports mentioned, a clear strength increase was observed for all DLJ tests as well as the bulk specimen tests. For the EA 9696 film adhesive, a graph over the typical stress strain curves indicate an increase of approximately 50% in strength and 100% in tensile modulus. That this modulus increase is valid also for the EA 9394 adhesive is confirmed by Bartoszyk [33] who presents some cryogenic material parameters for EA 9394 (E, G and α values).

Table 3.7 *Temperature dependent CZM material data*

Temp. [K]	G_{Ic} [J/m^2]	G_{IIc} [J/m^2]	τ_{max} [MPa]	K_n [N/m^3]	K_t [N/m^3]
293	425	2000	40	2×10^{13}	1×10^{12}
123	200	1000	60	4×10^{13}	2×10^{12}

Based on the literature values, an estimated set of temperature material data for EA 9394 (see Table 3.7) could be assembled and used with ANSYS to make reiterations of some key TED analyses. Although only containing data for two temperature values, ANSYS uses linear interpolation to extract values for intermediate temperatures. It has been assumed that the decrease of G_{IIc} for the EA 9394 corresponds to that reported for EA 9696 and that the increase of modulus and strength causes the stiffness and maximum shear stress to increase as well. This is a crude approximation of the nonlinear temperature dependence of the real materials but should show some indication of how severely the change of material properties affects the results.

4. Results

This section of the report presents the relevant results that were the outcome of the analysis methods described in the previous chapter. Since numerical analyses generate large amounts of data, only a fraction has been extracted and presented below. The aim is to objectively present the results of the tests and analyses without anything more than a short explanation of what is presented in the figures and graphs. A more thorough analysis of the results and comments on their importance to the project is found in the following Discussion chapter.

4.1 Obtaining Material Parameters

Simulations of tensile tests with double lap joint specimens were carried out to obtain material parameters for further analysing titanium to composite adhesive joints. In order to understand how changing the parameters of the cohesive zone material affected the results of the feigned tensile tests a Design of Experiments methodology was applied. In Figure 4.1 is the force-displacement response presented for the specimen models used in the first DOE matrix.

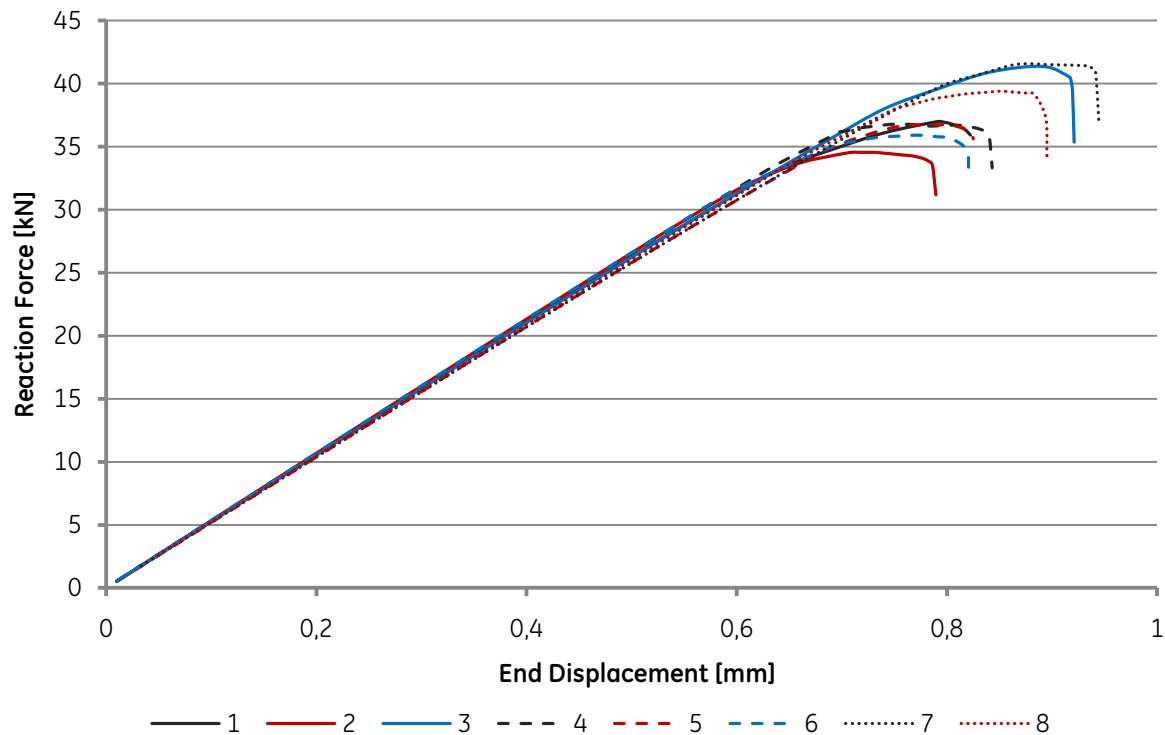### 4.1.1 DOE 1 – Material Parameters

Figure 4.1. *Force – displacement plot of the tests included in the DOE 1 test matrix*

The legend numbers in the force-displacement plot above correspond to the run numbers set up in the DOE test matrix shown in Table 4.1. A complete factorial test has been carried out and as can be seen from the table, all possible combinations of the factor levels have been tested. The quantity listed as Result was chosen as the maximum reaction force recorded during the test run in units of kN.

Table 4.1. *DOE test matrix 1 including results and calculated effects. Result of test is maximum reaction force in kN.*

Run	A	B	C	Result
1	-	-	-	37
2	+	-	-	34.4
3	-	+	-	41.5
4	+	+	-	36
5	-	-	+	36.7
6	+	-	+	36
7	-	+	+	41.5
8	+	+	+	39.4
Effect	-2,725	3,575	1,175	

Term	Factor	Levels (Hi - Lo)
A	τ_{max} [MPa]	40 / 60
B	G_{IIc} [J/m^2]	1600 / 2000
C	G_{Ic} [J/m^2]	350 / 425

The following figures have been extracted from the DOE test data using the statistical software Minitab 15. The relative effect on the result parameter from altering CZM material properties has been calculated for every test factor (See Table 4.1 – bottom row). In the following graphs (Figures 4.2-4) these effects have been illustrated in different ways to clarify the results and to assist the analysis of the results.
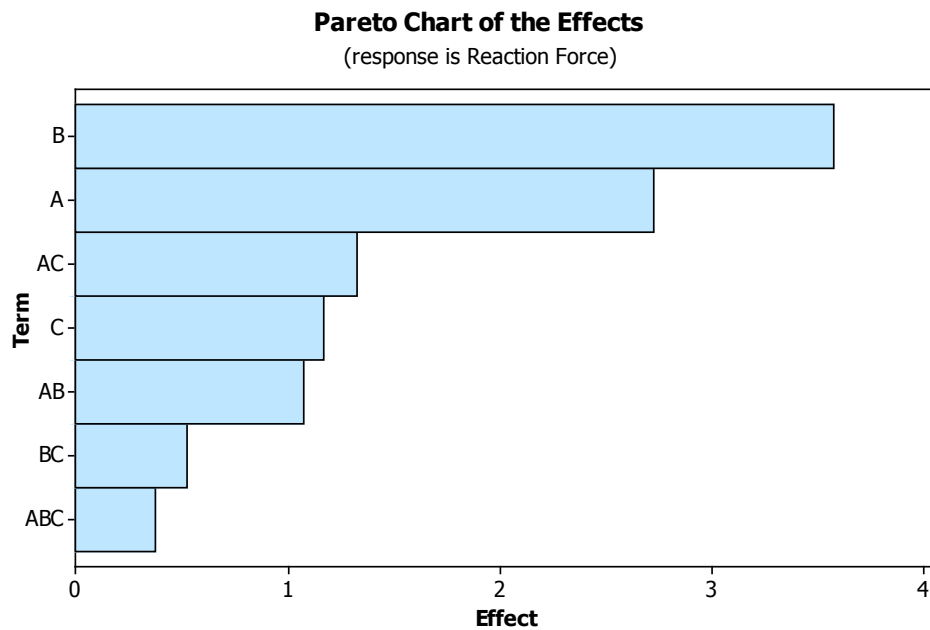
Pareto Chart of the Effects

(response is Reaction Force)

Figure 4.2. *Pareto chart showing the effects of the factors and their interactions. The length of the bars corresponds to the absolute value of the effect of each factor and factor combination.*
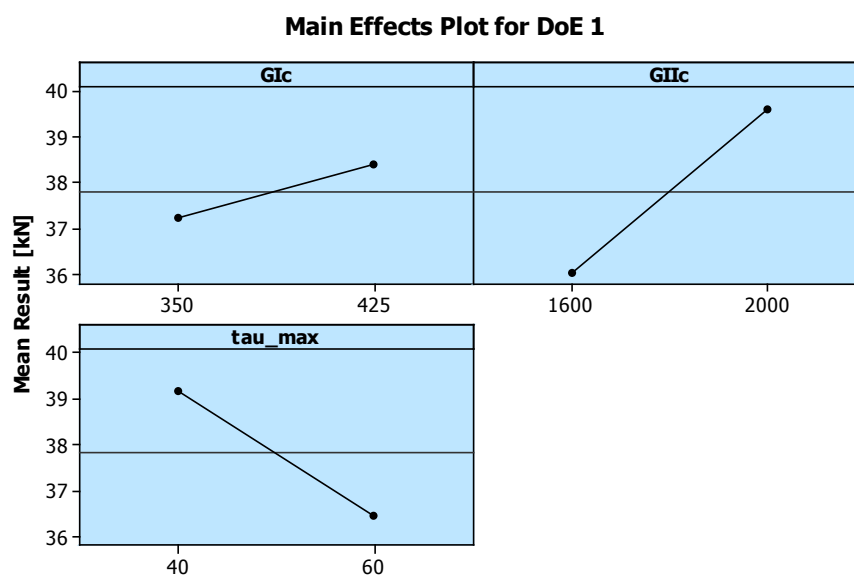
Main Effects Plot for DoE 1

Figure 4.3. *Test values of the main factors plotted against the mean result for each level. The slope of the curve indicates the magnitude of the effect*
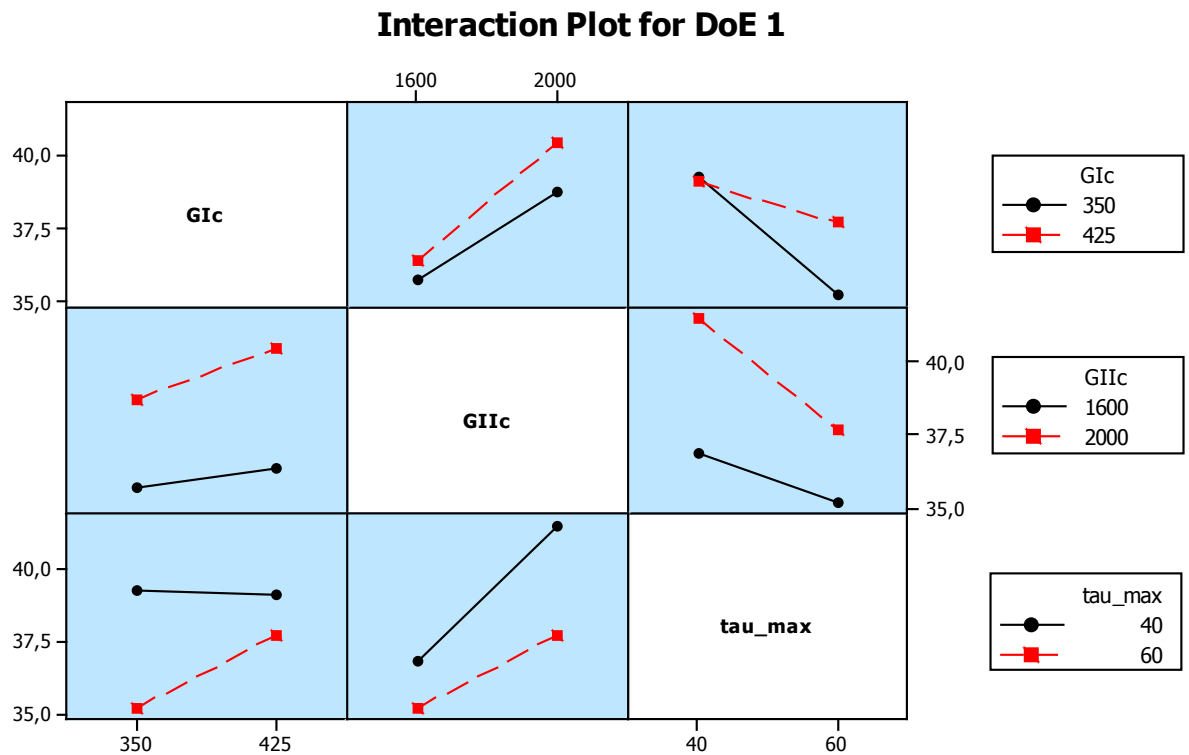
Figure 4.4. *Interaction plot where the average result of one parameter at the different test levels is compared against the value of the remaining parameter.*

4.1.2 DOE 2 – Modelling Parameters

A second DOE test matrix was constructed to evaluate the influence of altering certain FEA modelling parameters on the outcome of the tests. No coupled interactions were assumed between the material and modelling parameters, and so a separate test matrix could be used. The material parameter set used in the second DOE corresponds to run 8 in the first test matrix (DOE 1:8).
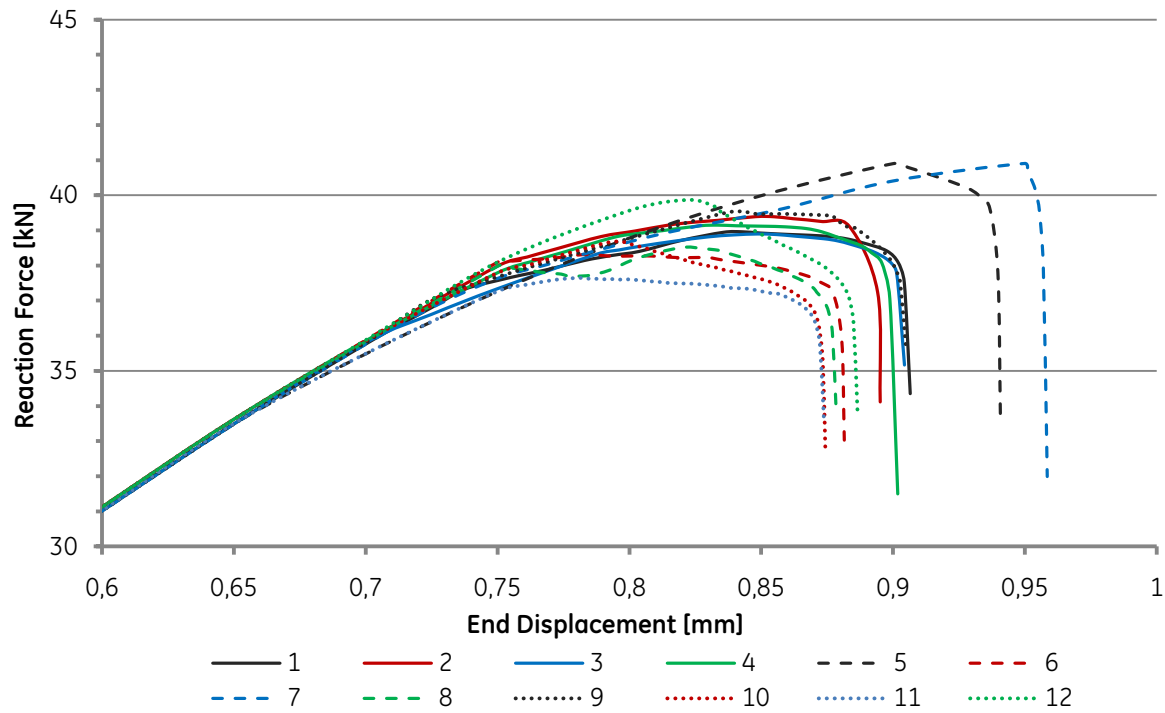

Figure 4.5. *Force – displacement plot of the tests included in the DOE 2 test matrix. Note that this is a close-up and the linear elastic section has been omitted for clarity.*

Table 4.2 *Test matrix for DOE 2.*

Run	Contact Algorithm	Contact Surface	Non-Linear Geometry	Result
1	Penalty	CFRP	On	38.96
2	Penalty	CFRP	Off	39.39
3	Penalty	Symmetric	On	38.89
4	Penalty	Symmetric	Off	39.15
5	Penalty	Titanium	On	40.90
6	Penalty	Titanium	Off	38.31
7	Aug. Lagrange	CFRP	On	40.91
8	Aug. Lagrange	CFRP	Off	38.51
9	Aug. Lagrange	Symmetric	On	39.51
10	Aug. Lagrange	Symmetric	Off	38.68
11	Aug. Lagrange	Titanium	On	37.65
12	Aug. Lagrange	Titanium	Off	39.87

Since the factors in the second DOE are not numerical, a meaningful effect value could not be computed. The effects of changing these parameters are instead only displayed through the effect and interaction plots below.
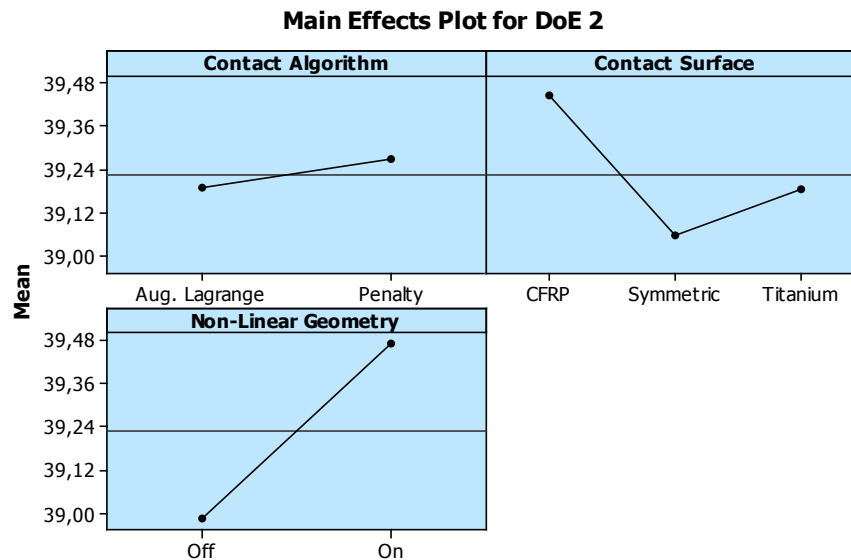

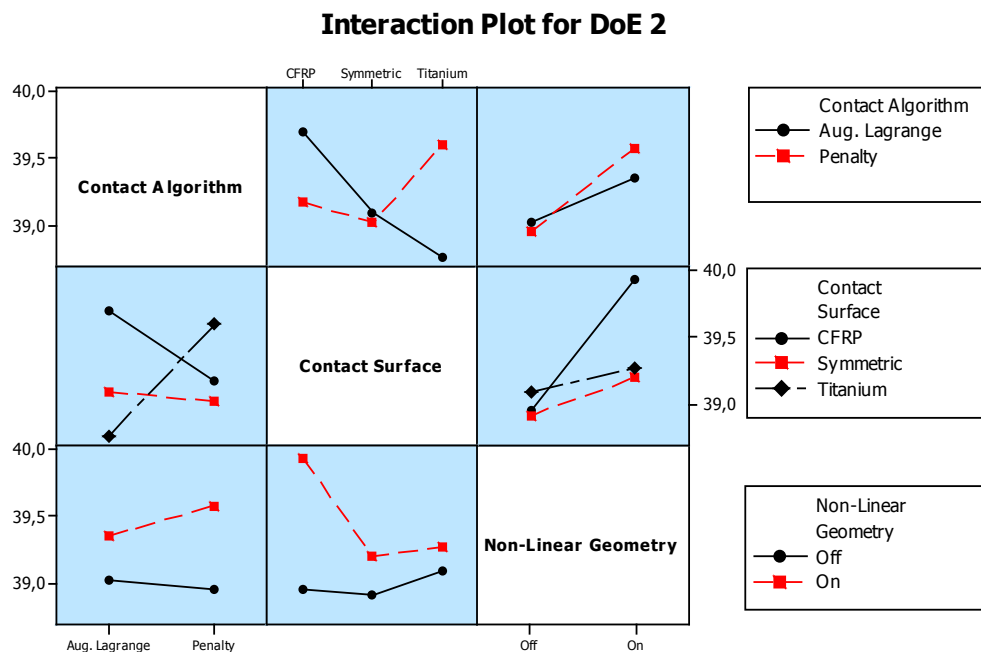Figure 4.6. *Effects of the main factors plotted against the mean result for each level.*

Figure 4.7. *Interaction plot for DOE 2*

4.1.3 *Typical Adhesive Stress Distribution*

The response of the CZM contact elements during a tensile test simulation is visualised in the following plots of the contact stresses in the adhesive layer. Both figures are extracted from a run with parameter set DOE 1:7. Top adherend is titanium and bottom is CFRP, note the symmetry condition about the Y-axis.
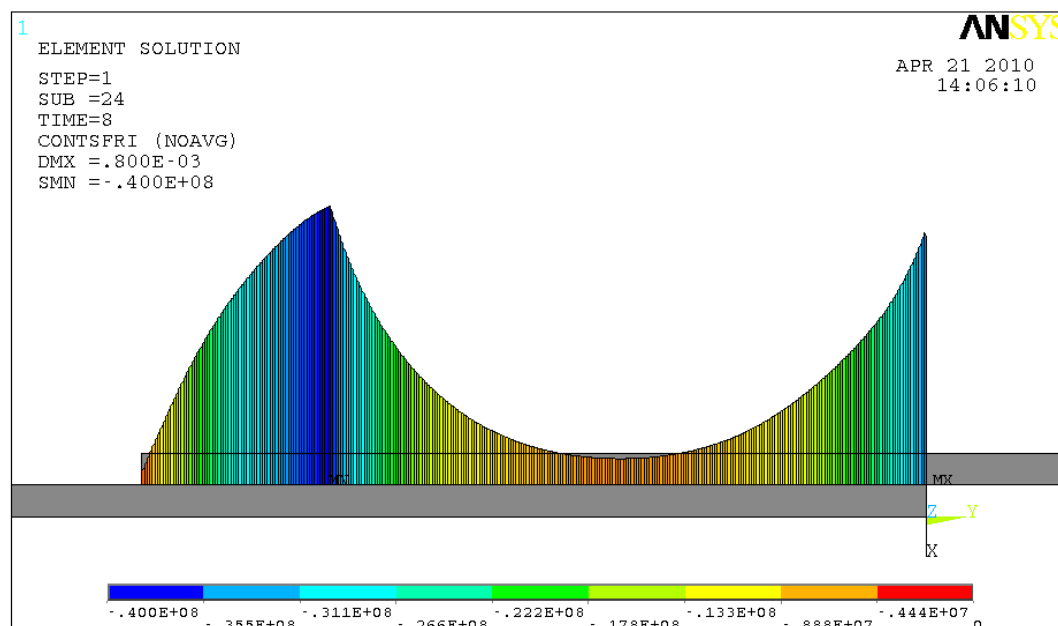

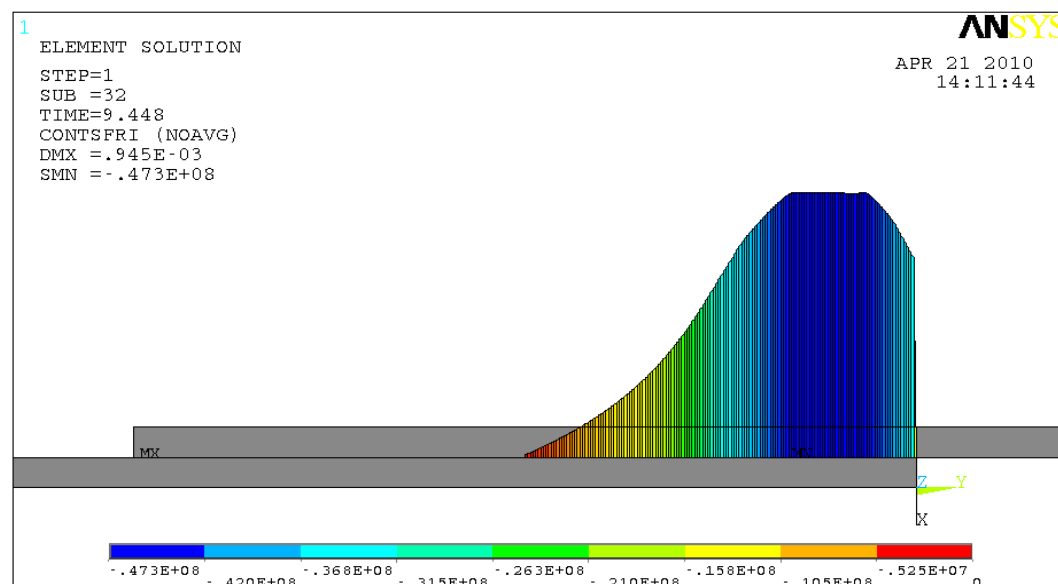Figure 4.8. *Adhesive shear stress at* u_y *= 0.8 mm for a DOE 1:7 test specimen*

Figure 4.9. *Adhesive shear stress at* u_y *= 0.945 mm, just before complete debonding.*

4.1.4 Final Parameters Resulting From the DOE Tests

The purpose of all analyses made with simulated test specimens was to compare the results to those of the screening tests performed by Sicomp and come to a conclusion regarding what parameters to use in the following analyses of the actual TED geometry. After analysing the DOE test data, making comparisons with the screening test result as well as taking other recommendations into consideration (see chapter 5.1.2), the decision was made to use the following parameters in the succeeding simulations:

Table 4.3. *Final parameter values used for further CZM analyses*

G_{Ic} [J/m^2]	G_{IIc} [J/m^2]	σ_{max} [Mpa]	τ_{max} [MPa]	K_n [N/m^3]	K_t [N/m^3]	Contact Algorithm	Contact Surface	Non-Linear Geometry
425	2000	44.5	40	2×10^{13}	1×10^{12}	Penalty	Ti	Off

In all the DOE tests performed an adhesive overlap length of 50 mm was chosen simply because it appeared as the best compromise between the 15, 50 and 100 mm overlaps that were used in the screening tests. To validate the results from the 50 mm overlap specimens and further analyse the influence of the tested parameters, similar analyses were performed with the model changed to the other adhesive lengths. Below are the results for the three different overlap lengths, analysed using the parameters presented in Table 4.3.
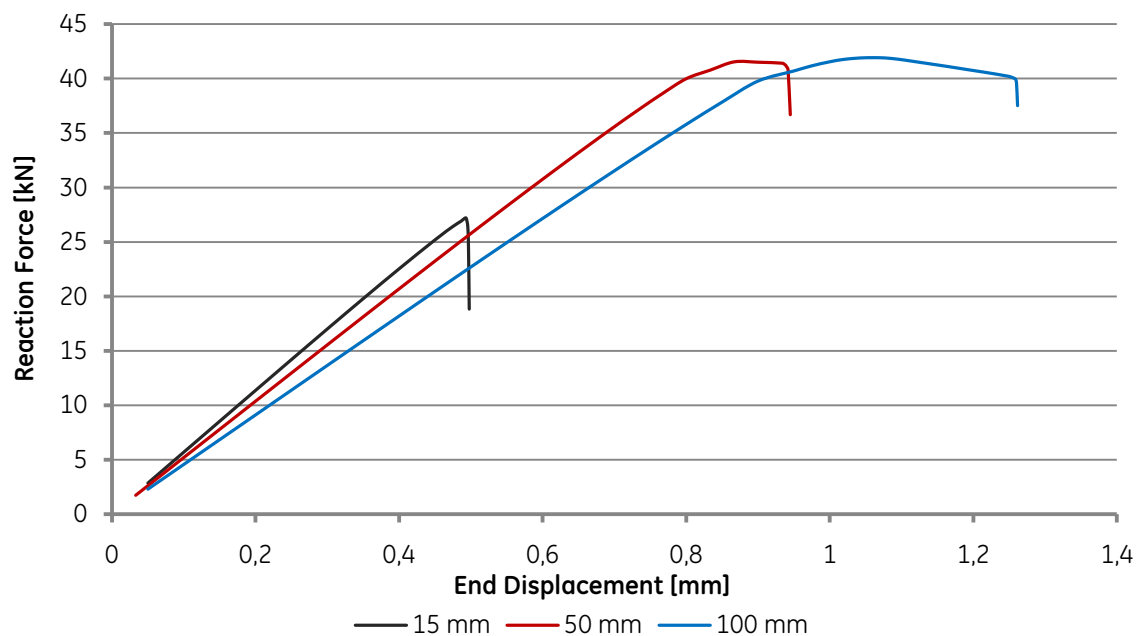

Figure 4.10. *Comparison of the reaction force response of specimens with three different adhesive overlap lengths*

4.1.5   3D Validation Model

To validate the 2D plane strain assumption that the above analyses was founded on, a 3D test specimen was also modelled and meshed. The geometry was that of the 2D specimens, simply extracted to a width of 25 mm. The mesh density on the contact elements is also somewhat lower than in the two-dimensional analyses. A contour plot of adhesive stress distribution during the tensile test at about 0.8 mm end displacement is shown in Figure 4.11 below. The plot shows the stresses in the contact elements of the adhesive layer from a top-down perspective; the surrounding solid elements of the adherends are not displayed for clarity, but would extend to the sides in the YZ-plane. As a comparison, the plot can be seen as a top-down view of the 2D stress plots in figures 4.8-9.
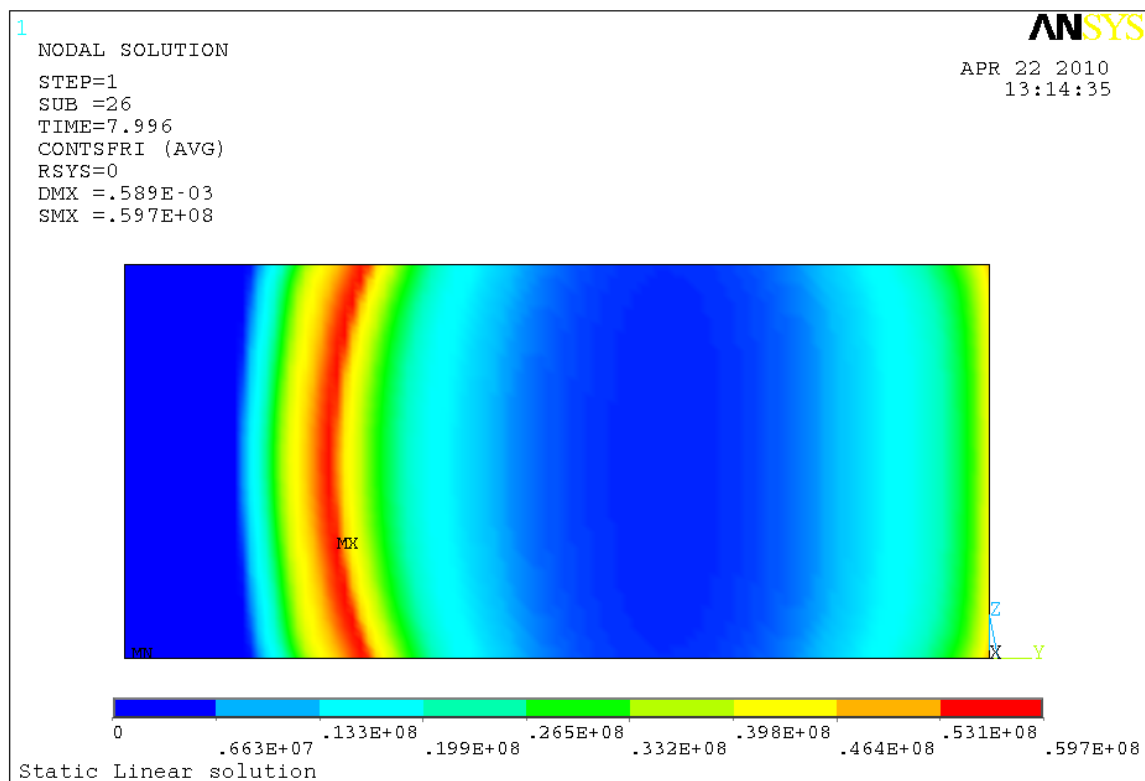

Figure 4.11. *Adhesive shear stress distribution over the adhesive surface of a 3D specimen model at* U_y = 0.8 mm. For this run the parameters where set according to DOE 1:8.

4.2 Axisymmetric TED Analysis

As a first step in evaluating the feasibility of a Ti 6Al-4V/CFRP hybrid design for the TED, two-dimensional axisymmetric models of the inlet flange with a simplified CFRP tube geometry were analysed.

To acquire a measure of how much the adhesive joint was affected by the loading and how close the adhesive was to reaching a critical load state, a more general parameter than just the adhesive stresses was needed. Since the mixed mode damage parameter d_m only is defined in the region where the adhesive already has started the damage process it was decided that, in addition to d_m, the parameter Δ (presented in chapter 2.3.3-a) would be an appropriate indicator of the general strain on the joint at lower stress levels.

In relation to the cohesive material law (see Figure 4.12), the Δ-parameter will be used from the unloaded state at the origin to the tip of the cohesive law, where the damage behaviour is initialised. From that point and further towards reaching the critical relative displacement of the joint, the d_m parameter will be used to describe the degree of damage on the CZM contact elements.
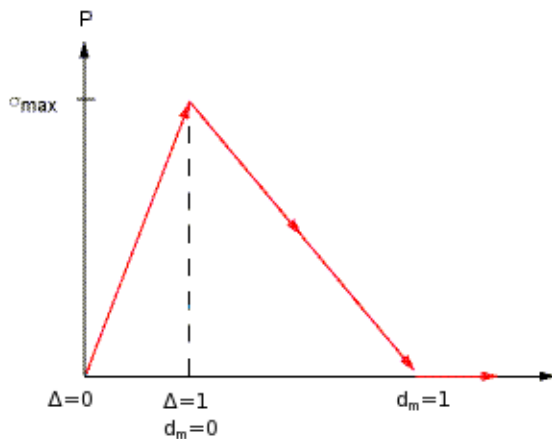

Figure 4.12. *Mixed mode cohesive law with ranges for Δ and d_m parameters.*

These two parameters, as well as the tangential and normal stresses in the adhesive layer, have been extracted and plotted versus time at two or three points (labelled A, B and C) depending on the geometry of the model. The locations of these points are shown in chapter 3.2.2.

The results presented below are grouped according to the geometry concepts laid out in chapter 3.

4.2.1   Preliminary Geometry – 40 mm Straight Overlap

4.2.1 - a Static Cryogenic Test (Load Case 1)

The cryogenic cooling load case was tested on the preliminary geometry with a 40 mm joint overlap geometry to analyse the general response of the adhesive during severe static cooling and to obtain a temperature distribution over the flange cross section.
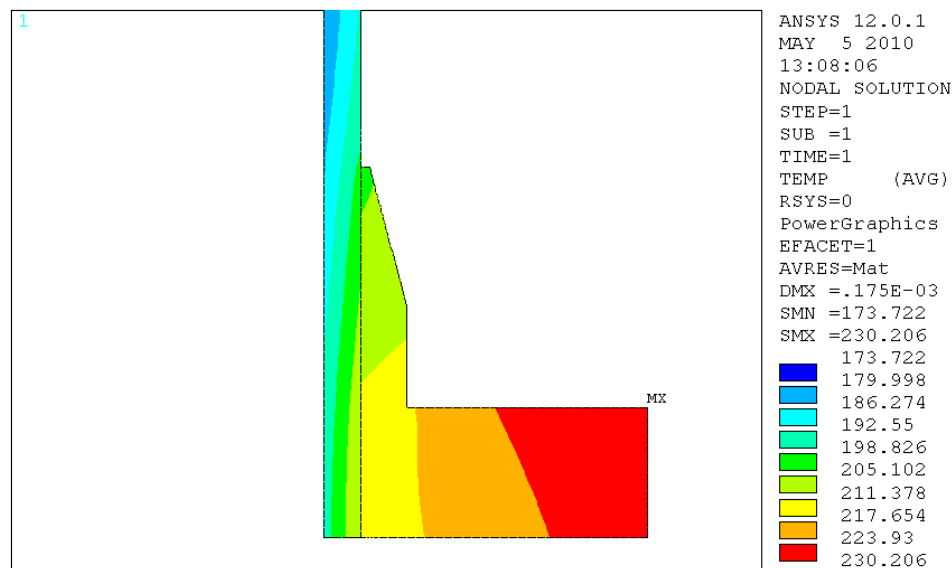

Figure 4.13. *Contour plot of the temperature distribution resulting from the static Load Case 1. Temperature is displayed in units of K.*
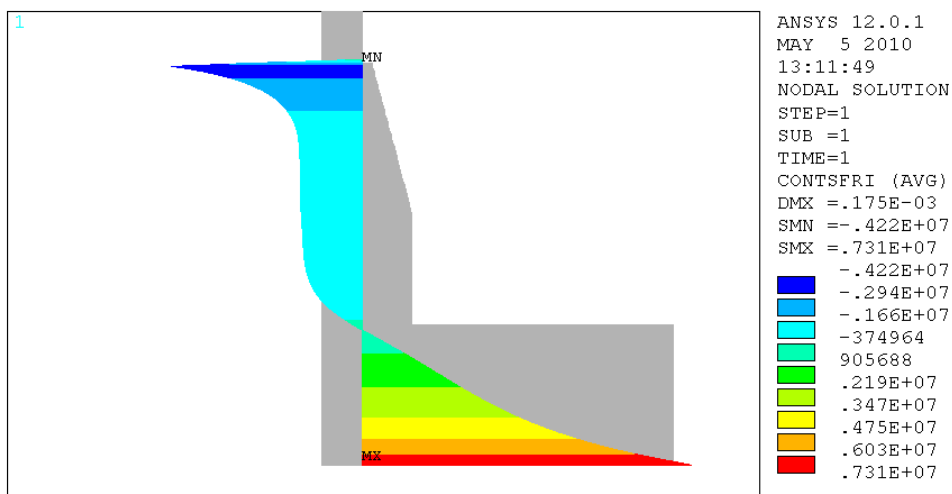

Figure 4.14. *Plot of the adhesive shear stress that is the result of the temperature field shown in Figure 4.13.*

4.2.1 - b Transient Engine Operation Sequence – Load Case 2

The same geometry was also tested with the transient load case to simulate an actual engine operation sequence. Stresses and effective displacements (Δ-parameter) were extracted at the end points of the joint and are plotted as a function of time in Figures 4.15-16 below
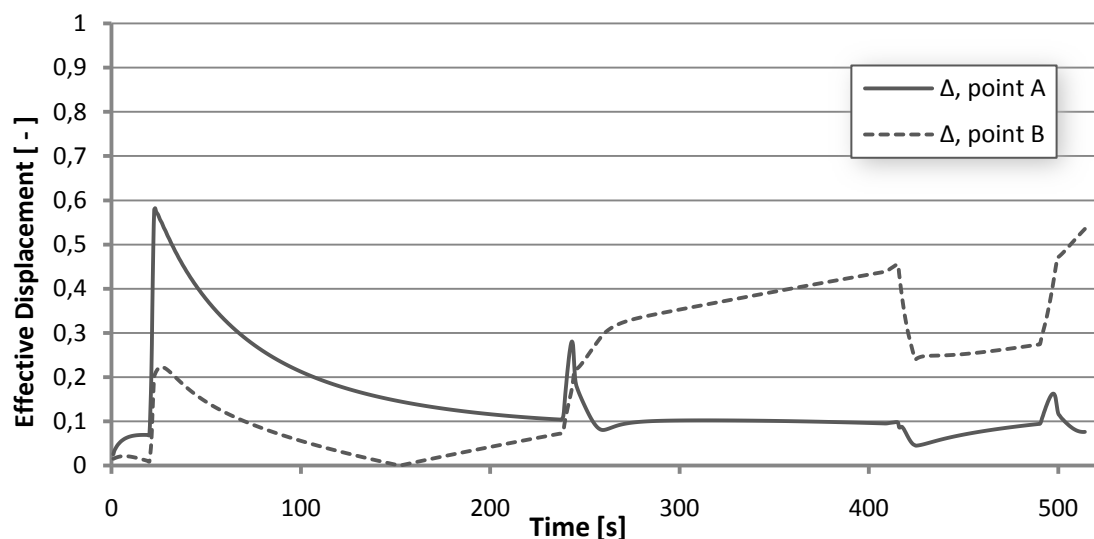

Figure 4.15. *Δ-value as a function of time for the original flange geometry with 40 mm adhesive length.*
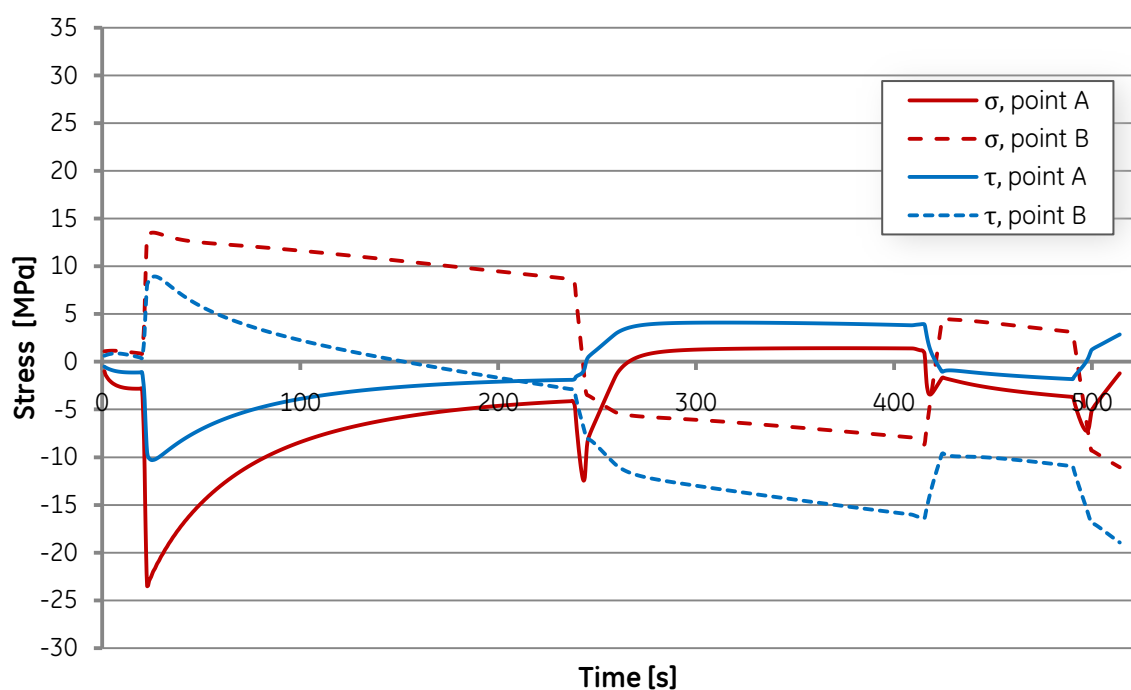
Figure 4.16. *Adhesive shear and normal stresses as a function of time for the original 40 mm geometry*

4.2.1 - c Load Case 2 – Separated Loads

To gain an understanding of how the different types of loads affect the adhesive joint a series of analyses were made where only one type of load was applied at the time. Separate runs were made for thermal, pressure and static structural loads. The stresses are extracted at point A in the preliminary geometry with 40 mm overlap.
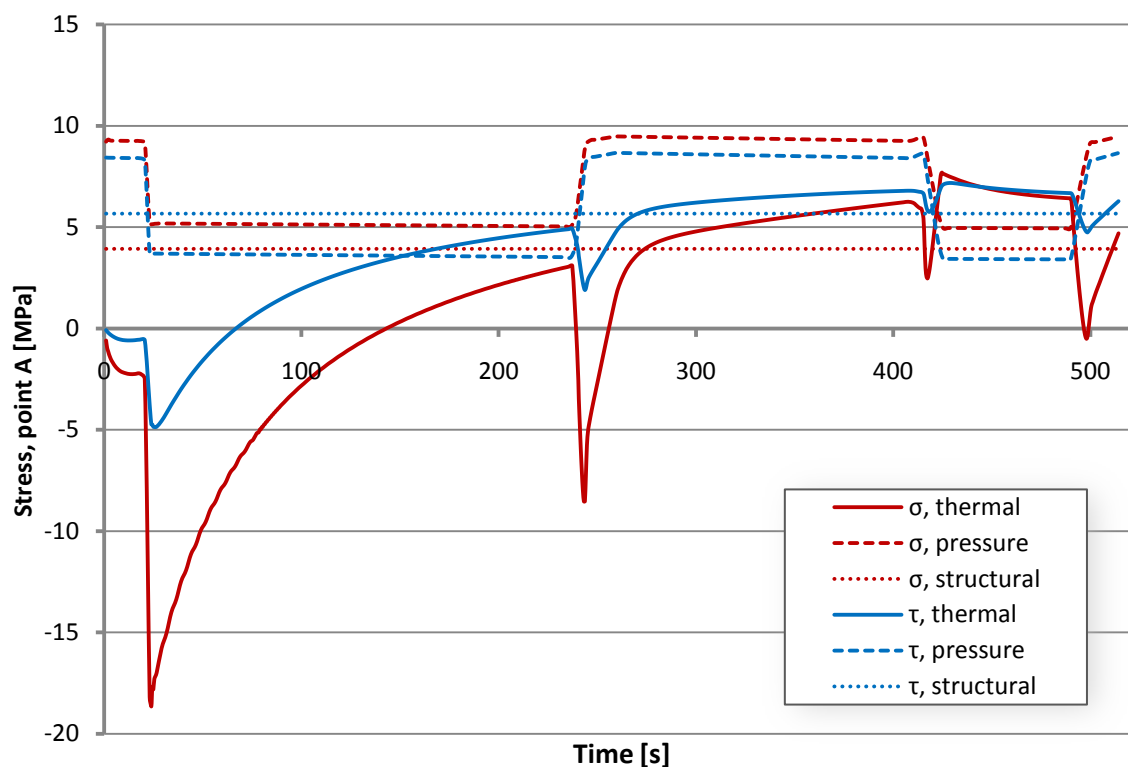
Figure 4.17. *Adhesive shear and normal stress as a function of time for three separate load types.*

4.2.2   Straight End – 25 mm overlap

The same load cases were tested with the overlap length shortened to 25 mm since that was considered the longest axial joint that could be accommodated without too much alteration of the current TED geometry.

4.2.2 - a Static Cryogenic Test (Load Case 1)
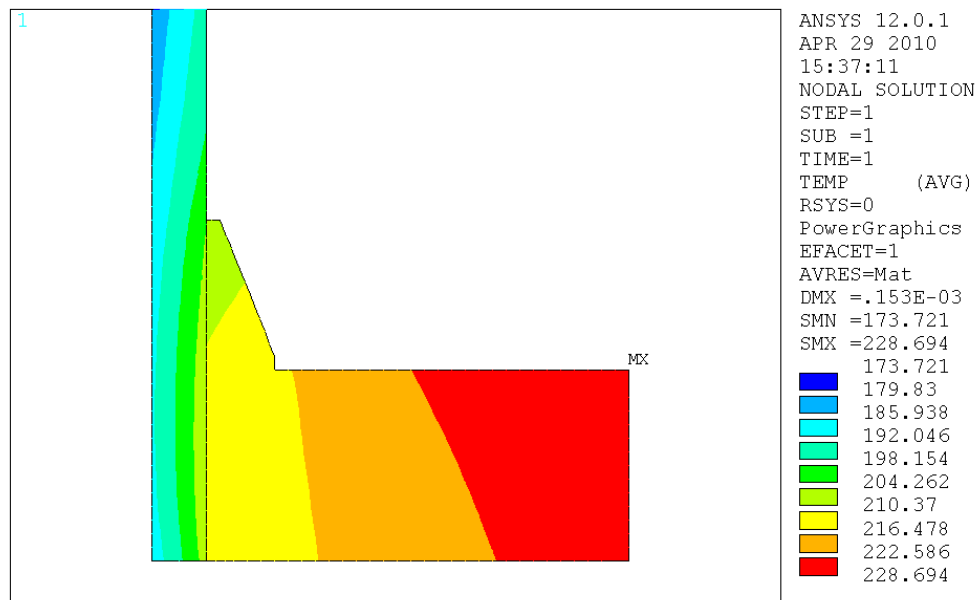
Figure 4.18. *Temperature distribution over the flange cross section from the static cryogenic test (Load Case 1). Temperatures in units of K.*
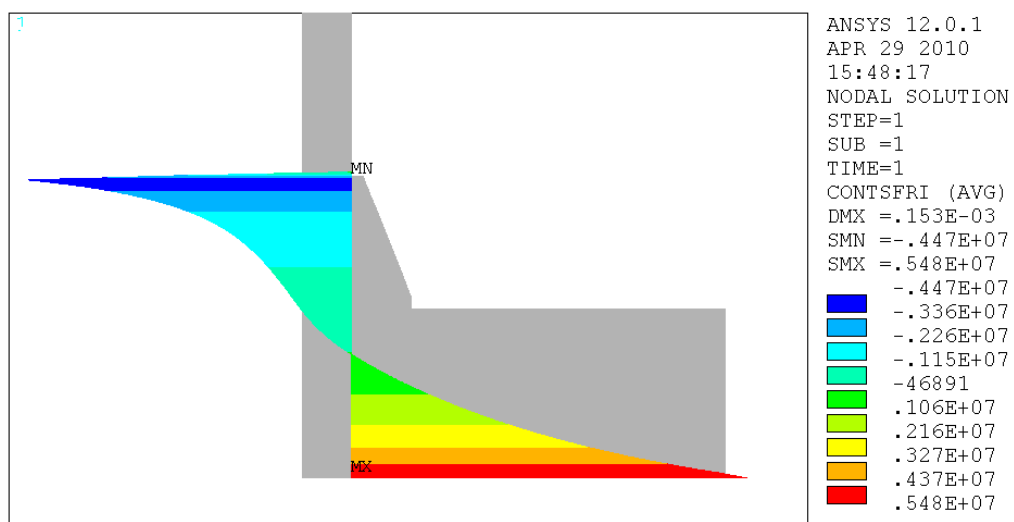
Figure 4.19 *Adhesive shear stress as result of the temperature load seen in Fig 4.14.*

4.2.2 - b Transient Engine Operation Sequence – Load Case 2
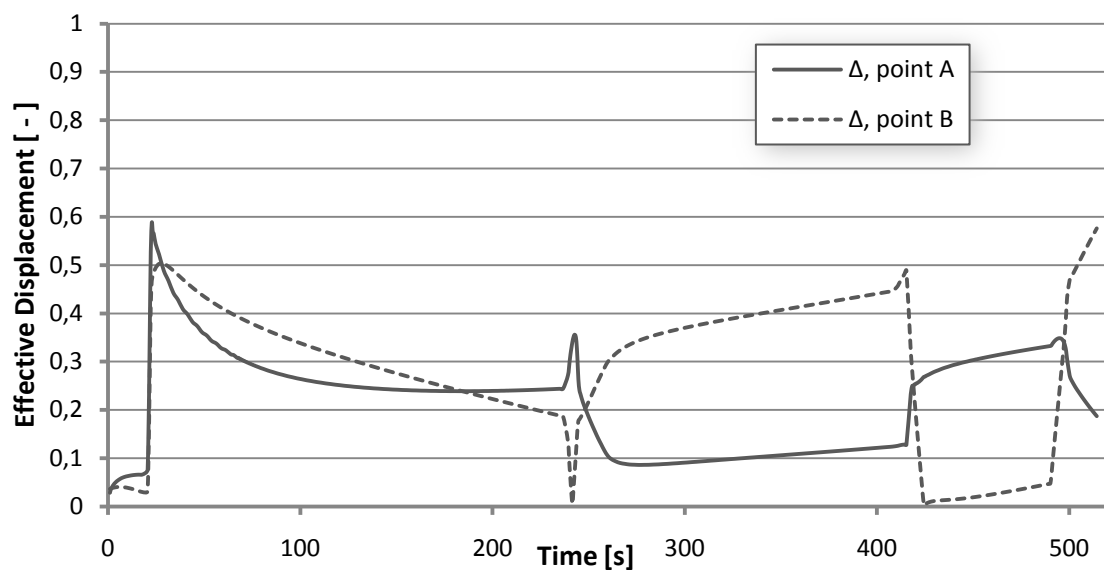
Figure 4.20. *Δ-value as a function of time for the original flange geometry with 25 mm adhesive length.*
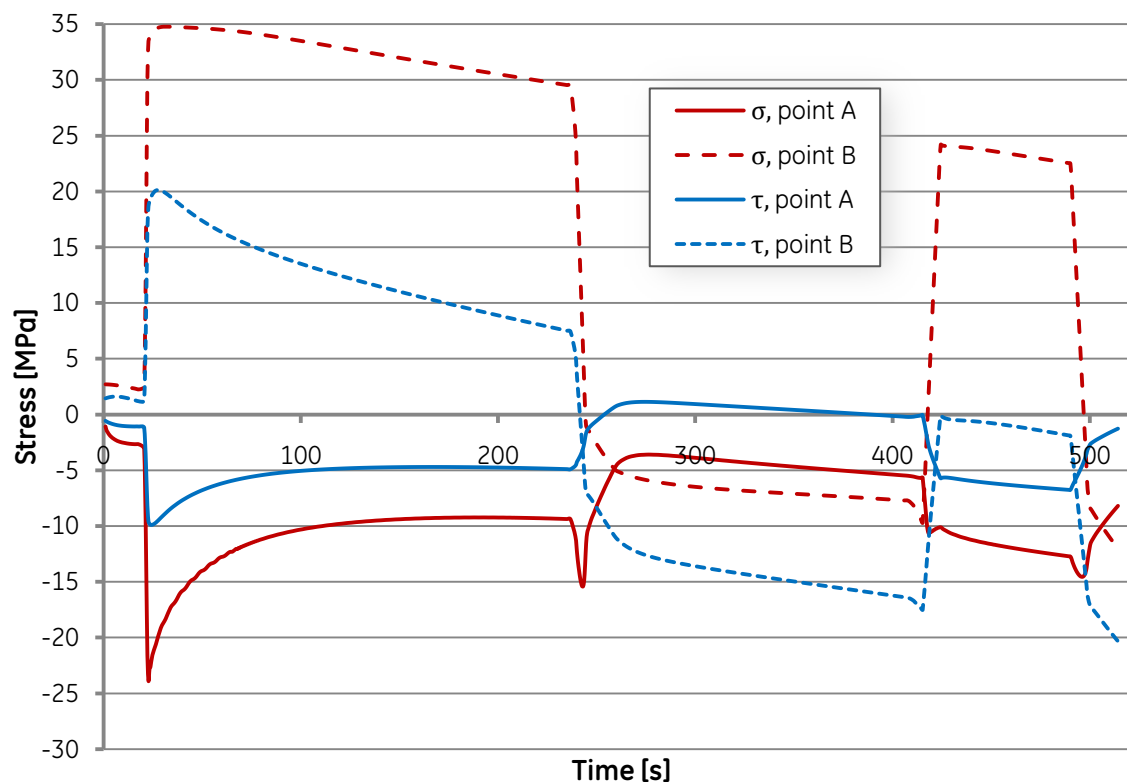
Figure 4.21. *Adhesive shear and normal stresses as a function of time for the original 25 mm geometry.*

4.2.3 Embedded Straight End Geometry

To further make the joint geometry more realistic, the composite tube was embedded into the flange to make it compatible with the TED flange geometry. This resulted in an extra adhesive surface at the end surface of the composite tube and therefore another measurement point had to be added as well. Testing was focused on the transient load cases since the low stresses resulting from Load Case 1 was not considered critical to the joint design.
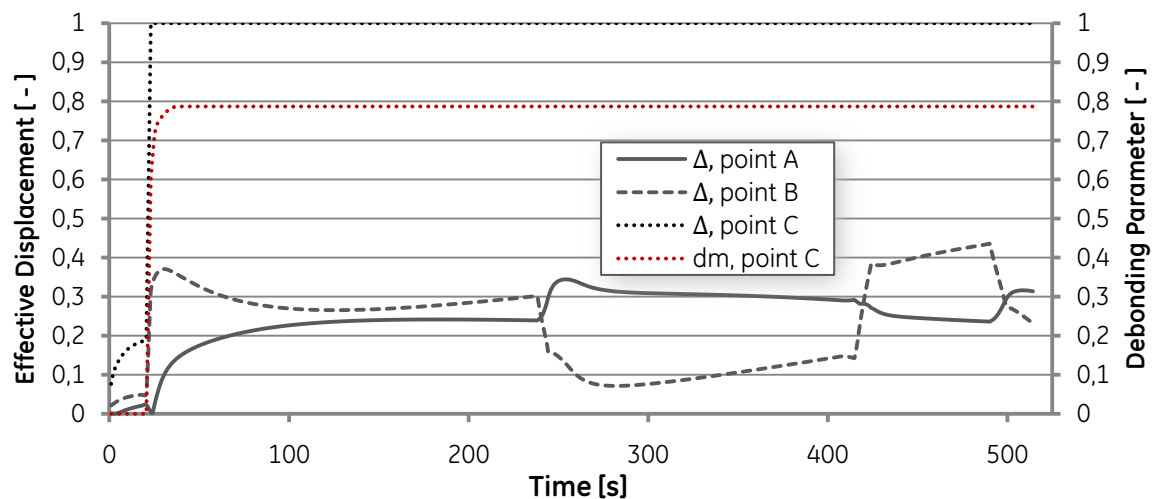
Figure 4.22. *Values of the Δ and d_m parameters as a function of time for the embedded straight end geometry with 25 mm adhesive length.*
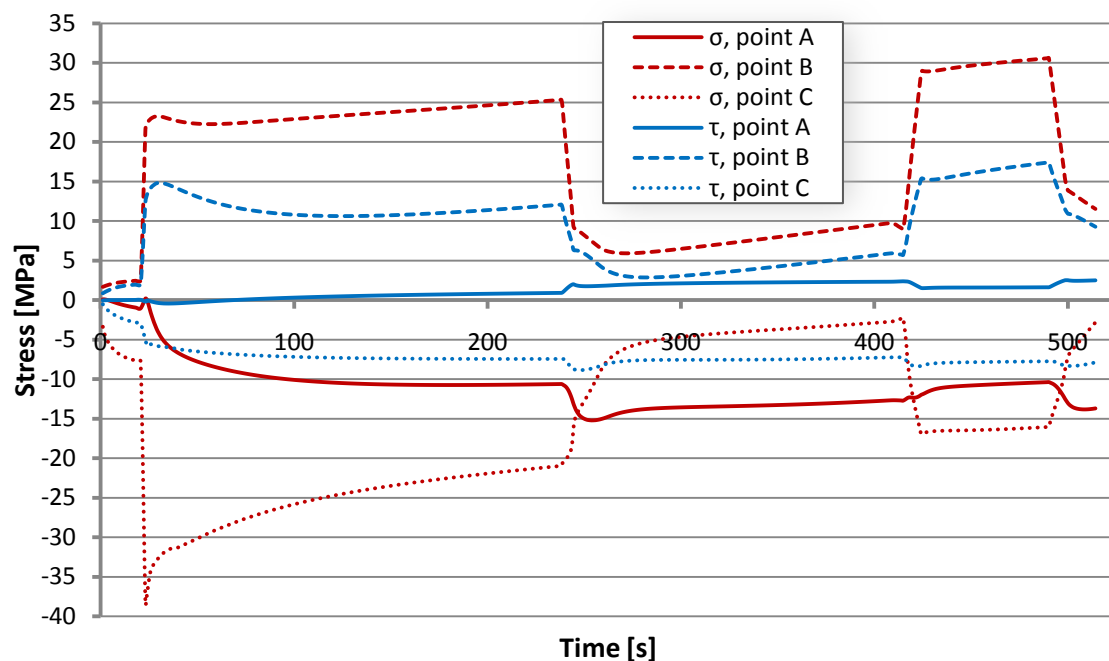
Figure 4.23. *Adhesive shear and normal stresses as a function of time for the embedded straight end geometry.*

4.2.4 Short Tapered End Geometry

To overcome the high peel stresses on the end surface in the embedded straight end geometry, the edge was tapered to a slanting edge that would transfer more of the load into the stronger tangential direction of the joint. As before this geometry was only tested with Load Case 2.
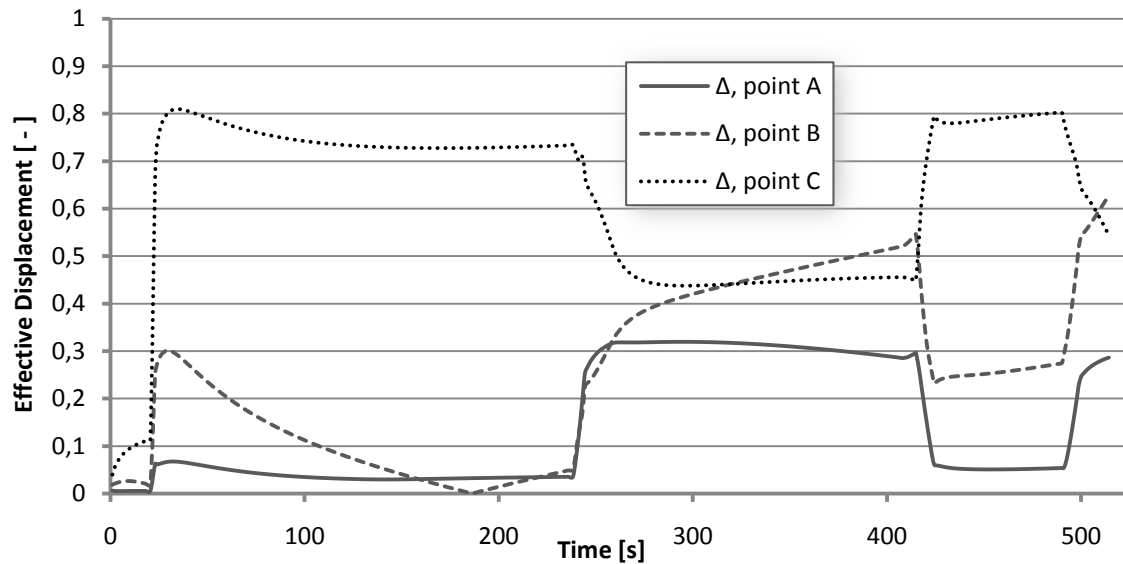
Figure 4.24. *Δ-value as a function of time for the short tapered geometry.*
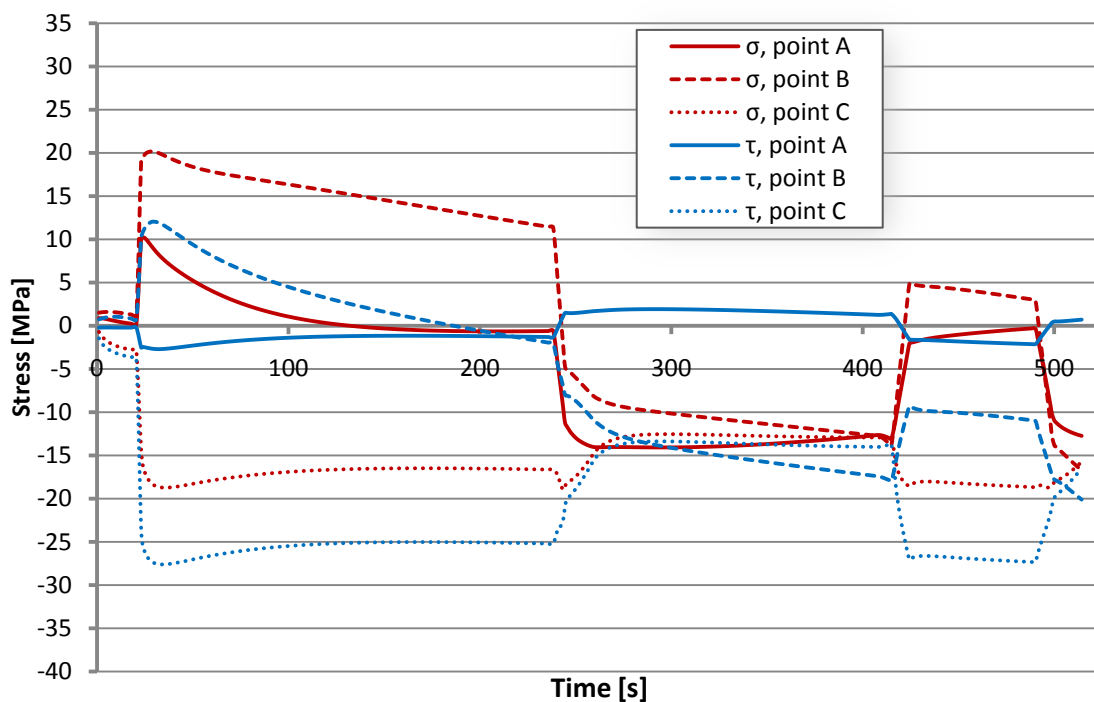
Figure 4.25. *Adhesive shear and normal stresses as a function of time for the short tapered end geometry.*

4.2.5 Fully Tapered End Geometry

After including production aspects into the concept generation process it was decided that a fully tapered geometry would be favourable. This final geometry concept was also only tested with Load Case 2.
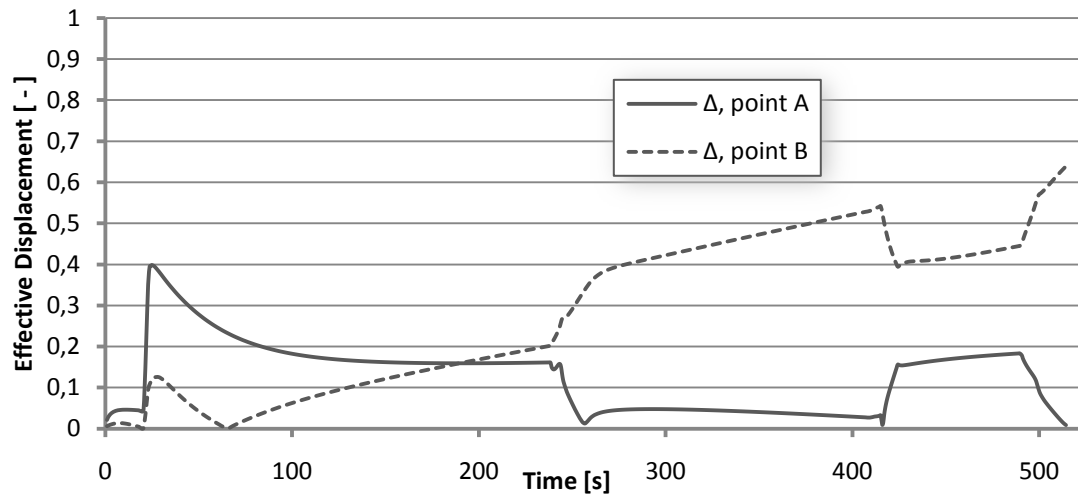
Figure 4.26. *Δ-value as a function of time for the fully tapered geometry.*
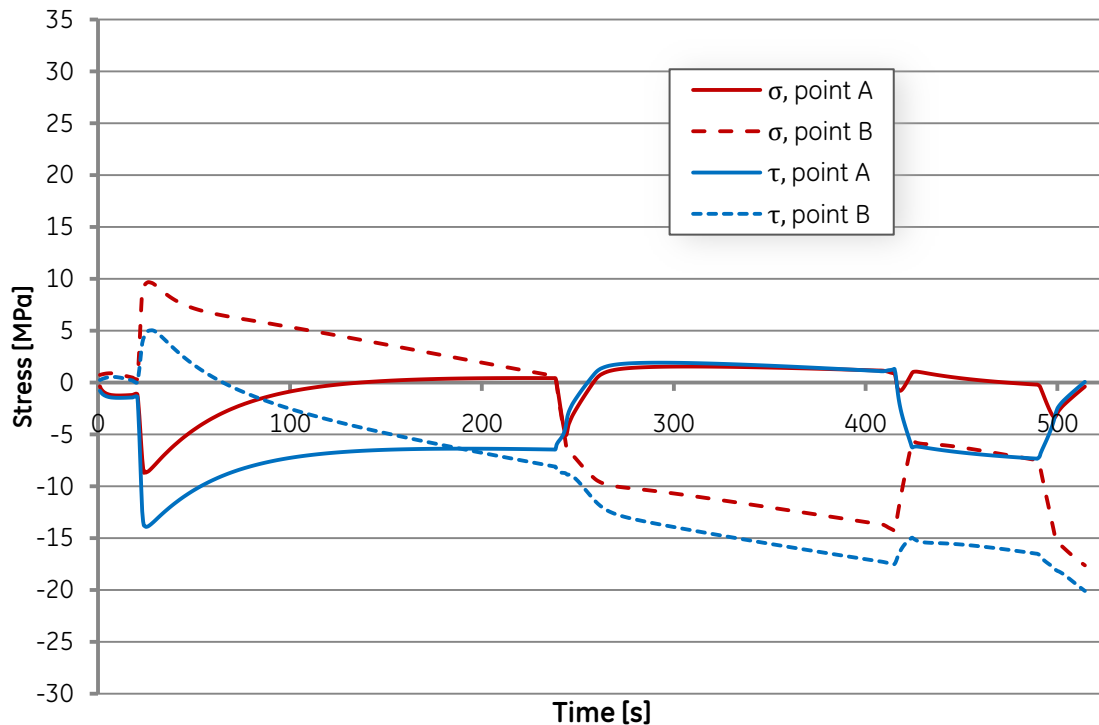
Figure 4.27. *Adhesive shear and normal stresses as a function of time for the short tapered end geometry.*

4.3 3D TED analysis

Since the actual operational loads on the TED interfaces are far from axisymmetric a fully three-dimensional model had to be created in order to analyse the joint under more realistic conditions. After analysing the axisymmetric results it was concluded that the most suitable joint design for the TED inlet flange would be a fully tapered geometry (see chapter 5.2.2-d) and hence that is what has been used for the 3D analyses.

4.3.1 Static Structural Analysis

Prior to commencing the time consuming transient analysis, a static run with only the unsymmetrical structural load applied was performed. The resulting stress distribution and the Δ-parameter at the adhesive layer is shown in Figures 4.26-28 below. The plots show only the contact elements forming the adhesive layer, the surrounding flange and composite tube is not displayed. The Δ-parameter has been separately calculated and plotted over the adhesive surface similar to the stress plots.
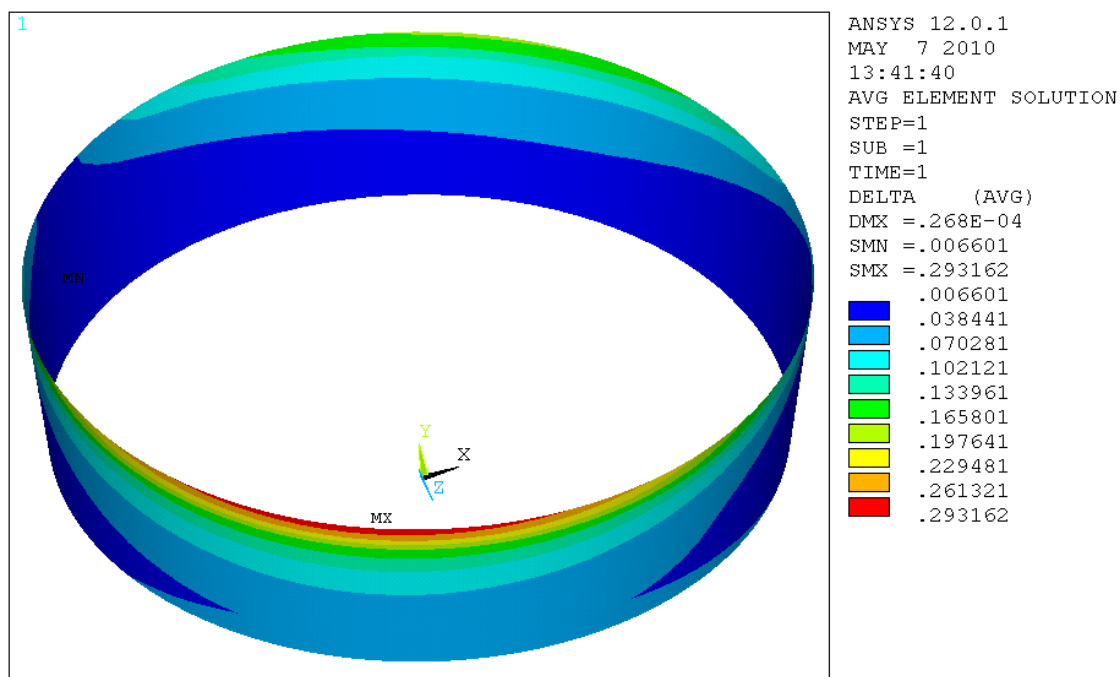
Figure 4.28. *The Δ-parameter showing the effective displacement resulting from static structural loads only.*
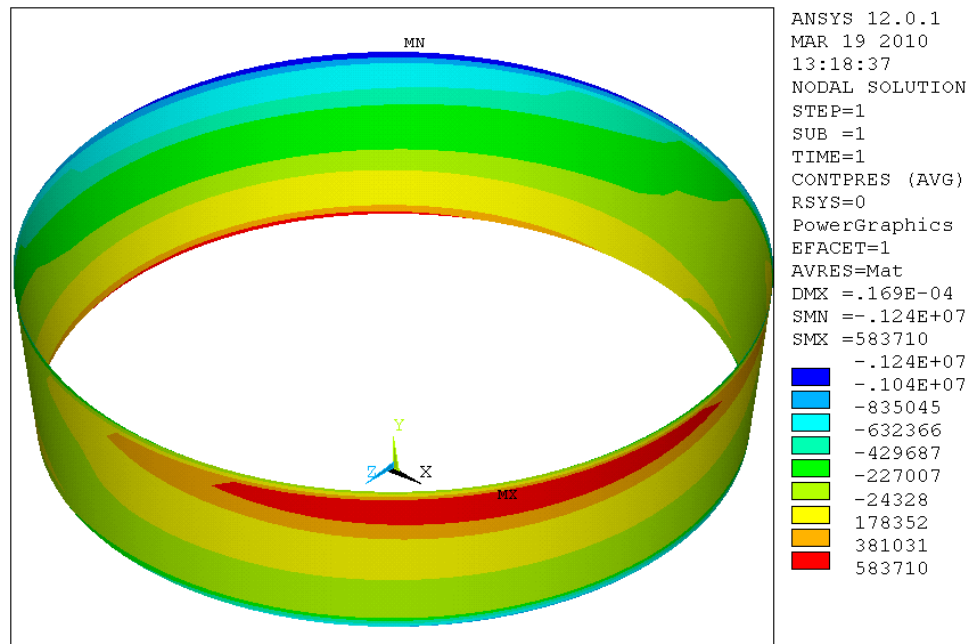
Figure 4.29. *Adhesive normal stress resulting from static structural loads only.*
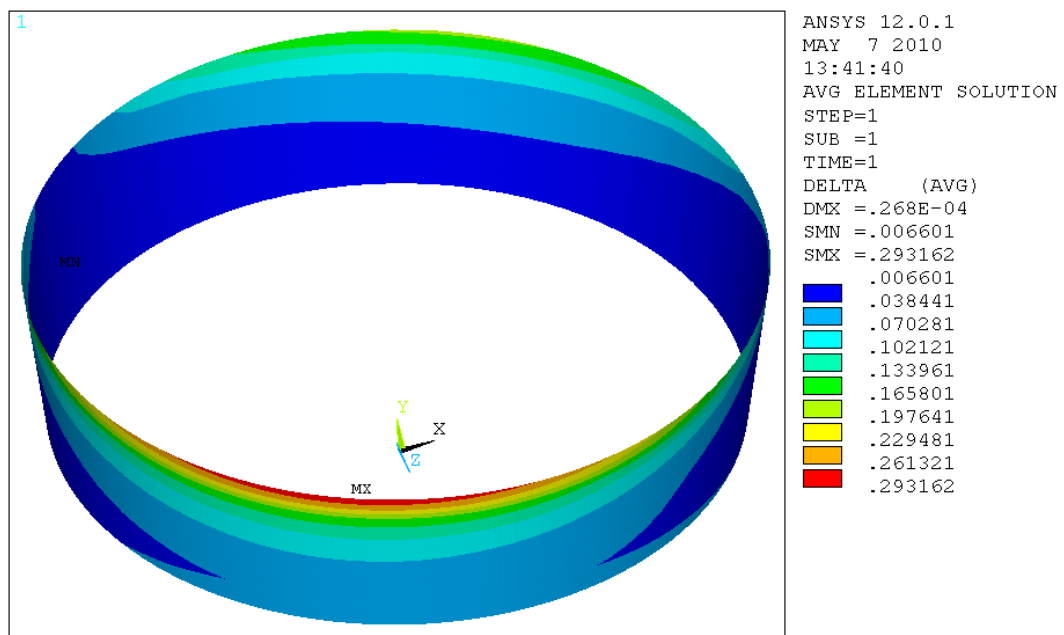
Figure 4.30. *Adhesive shear stress resulting from static structural loads only.*

4.3.2 Coarse Model Transient Analysis

A single full transient analysis was performed with the coarse 3D model to find points of interest on the contact surface where stress concentrations would be located. The approach with investigating static points on the joint would not be meaningful in the 3D case so and an alternate strategy was employed. Instead the highest value of the variable in question on the contact surface has been extracted for every time step and plotted as a function of time. Instead of pure normal stresses the peel stress is used instead in Figure 4.31, this is simply the absolute value of the negative normal stresses and shows better on a positive scale the detrimental effects on the adhesive layer.
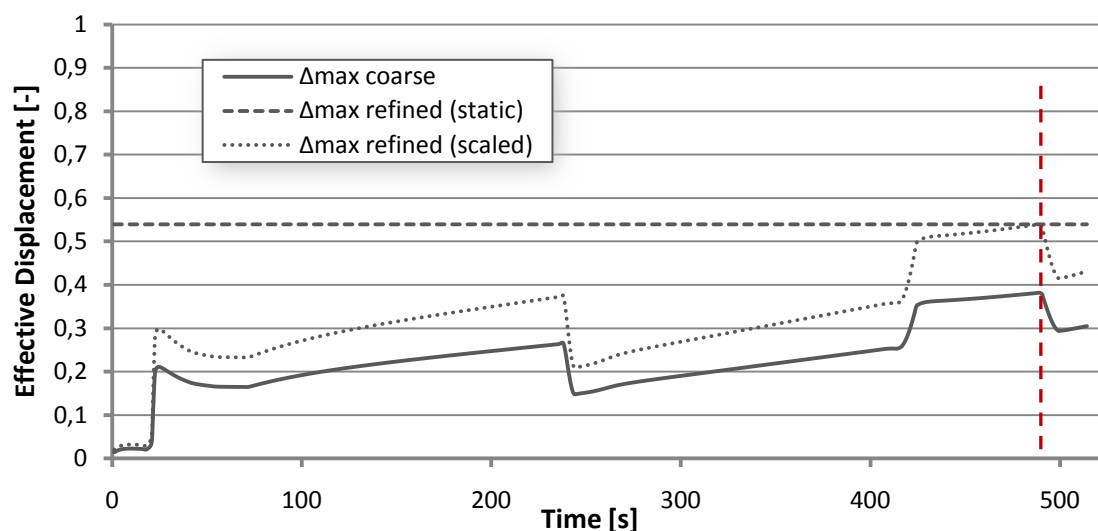
Figure 4.31. *Maximum value of the Δ-parameter over time for coarse full model and submodel
Red line marks the time step of the highest recorded Δ-value (489 s)*
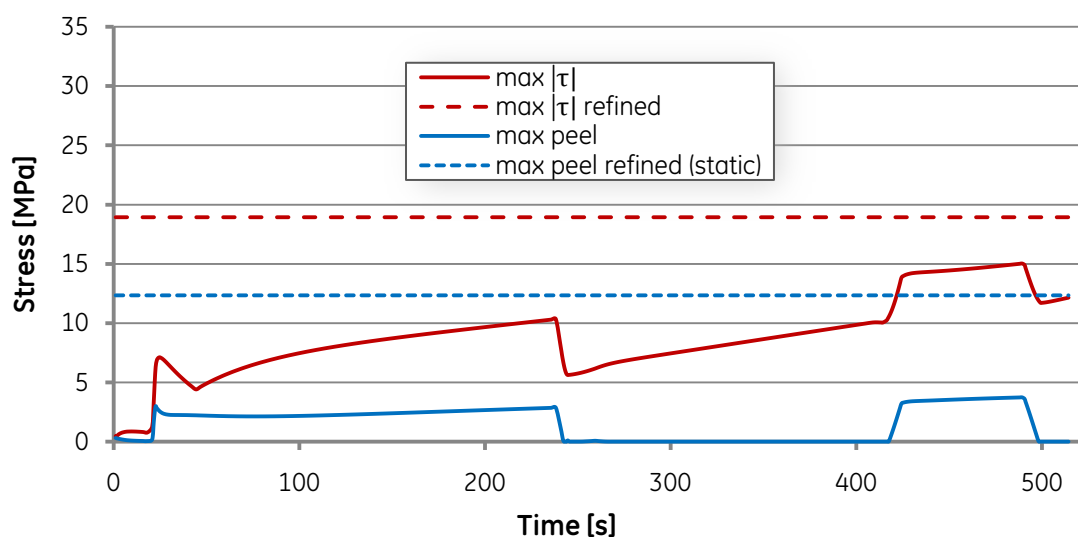
Figure 4.32. *Maximum values of adhesive shear stress and peel (absolute of negative adhesive normal stress) from full coarse model and the submodel.*

4.3.3 Submodel Result Plots

For the submodel analysis, a 50° section was cut out around the point where the highest value of the Δ-parameter was observed, and the temperature body loads and the cut-boundary displacements were extracted from the corresponding time step. As for the full model plots, the figures below show a contour plot on the contact elements without displaying any additional geometry.
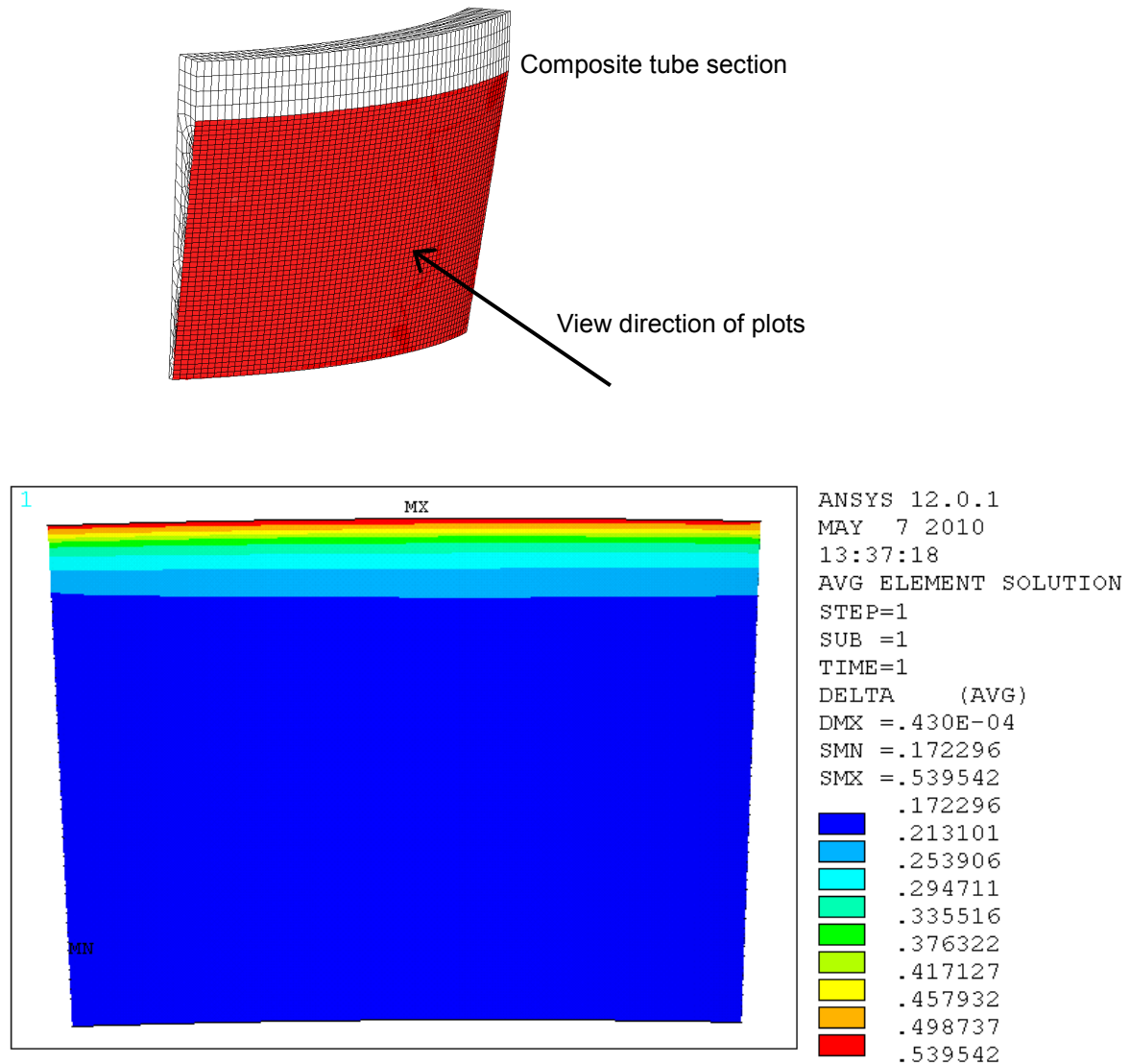
Figure 4.33. *Δ-parameter plot from the submodel. Corresponding to time t = 489.3 in transient run. Top figure shows the view direction of the submodel contour plots with contact elements marked in red.*
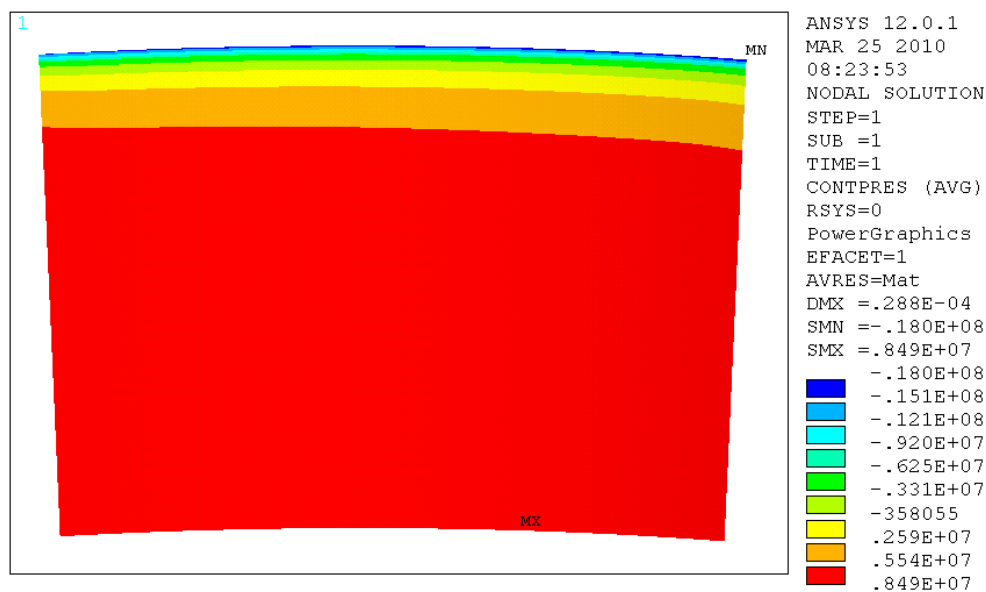
Figure 4.34. *Adhesive normal stress from the submodel. Corresponding to time t = 489.3 in transient run.*
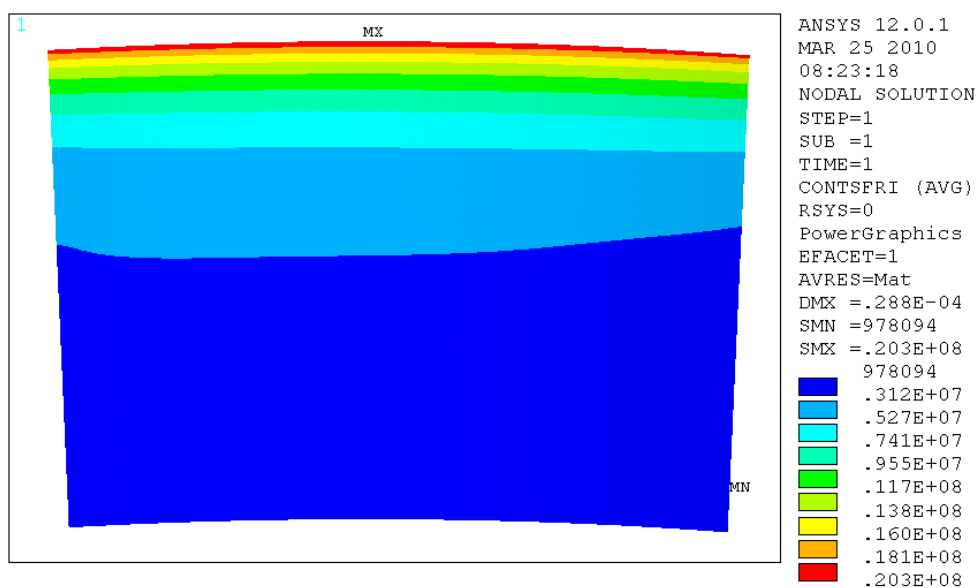
Figure 4.35. *Adhesive shear stress from the submodel. Corresponding to time t = 489.3 in transient run.*

4.4 Cryogenic Properties Analysis

Tests were performed to investigate the effect of altered material properties of the adhesive at low temperatures. The suggested parameters (see Table 3.7) were tested on DLJ test specimen models and after being sufficiently adjusted also on an axisymmetric TED geometry.
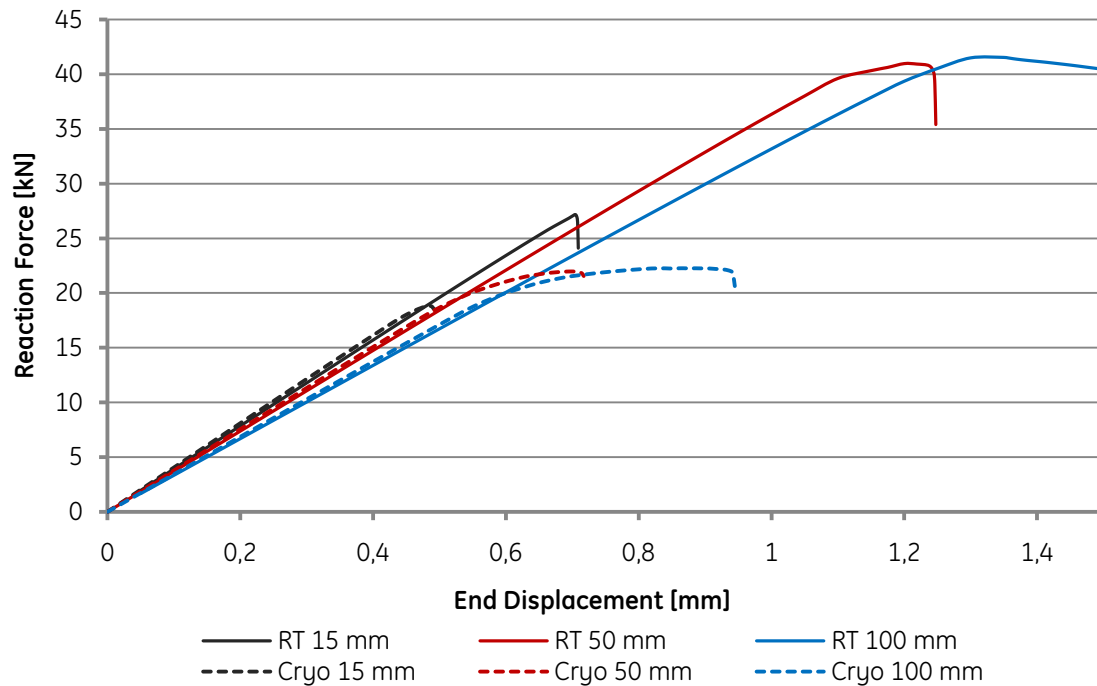
Figure 4.36. *Force – displacement plots of test specimen models of three overlap lengths using temperature dependent CZM material data.*

The tests on the TED geometry were performed using the fully tapered joint geometry and transient loads from Load Case 2, the only difference being using the temperature dependent material model when modelling the adhesive.
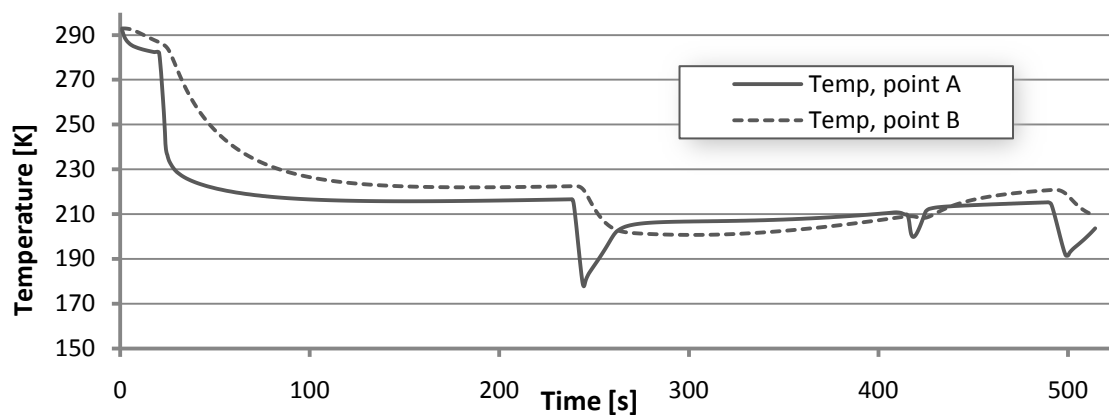
Figure 4.37. *Temperature at the end points of the adhesive layer during Load Case 2.*
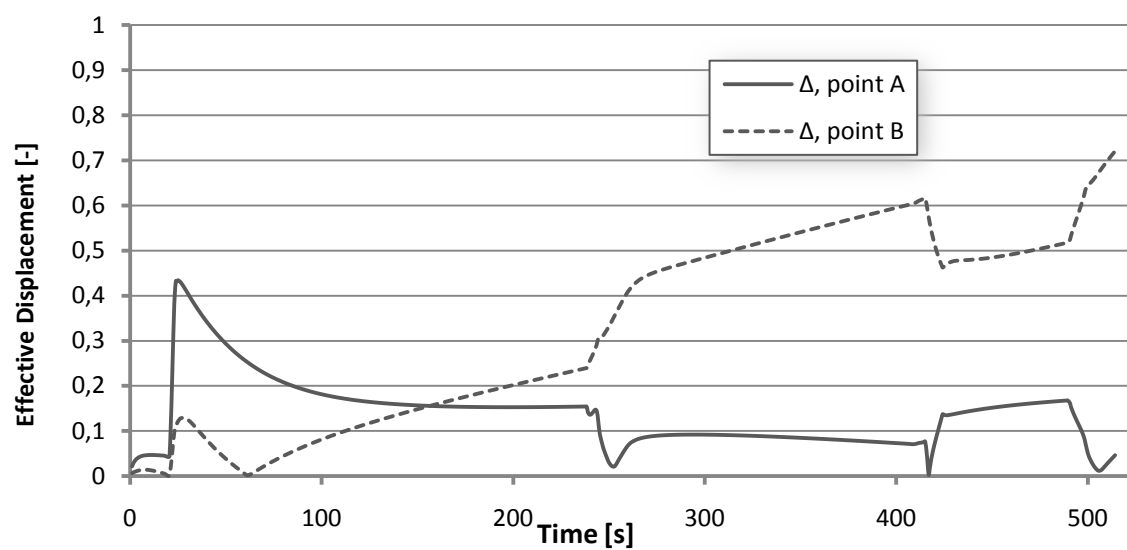
Figure 4.38. *Δ-value during Load Case 2 using temperature-dependent CZM data.*
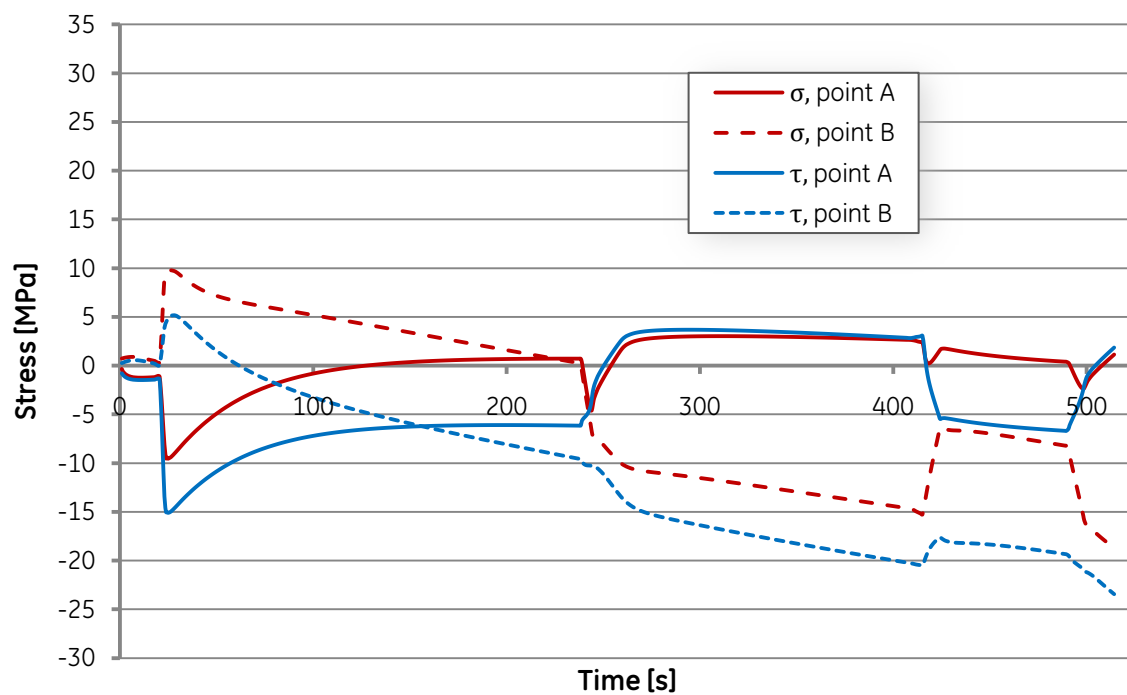
Figure 4.39. *Adhesive normal and shear stresses during Load Case 2 using temperature-dependent CZM-data.*

5. Discussion

This chapter discusses and comments on the previously presented results and contains inter-pretations of the figures, possible conclusion that can be drawn and general comments about the test outcomes. It is more subjectively written, and represents the author's interpretations and opinions about the obtained results. Also a few peripheral results that are not included in the previous chapter are presented here as a base for comparisons.

5.1 Analysis of Tensile Test Specimens

A main objective of this thesis project was to perform a valid and relevant analysis of the strength of adhesive joints in an engineering application. The lack of specific material data meant that the only available source for information about the strength performance was the tensile tests performed on DLJ specimens at Sicomp in Piteå. Although giving very good indi-cations about the global strength of the specific joint configuration, a tensile test of this kind does not yield any direct information about e.g. the local debonding and energy release in the adhesive.

Since no specific tests had been performed to acquire CZM material data within the KOMET project a compromise had to be made where a simulation of the tensile tests using FE-models of test specimens with CZM contact elements was performed and the results compared to those of the actual tests. The DOE test scheme used was a way to overcome this lack of a clearly distinguishable connection between the parameters and the test results.

The results of the first DOE test runs (see Figure 4.1) show a fairly typical response for an adhesive joint test specimen. First, there is an elastic part of the curve where the specimen is simply stretched under the load. This results in a section of the graph with an almost perfectly linear force-displacement response. Secondly, the adhesive layer starts to yield and the re-sponse curve levels out as the stiffness decreases. Eventually this softening leads to a point where the reaction force starts to decrease with increasing displacement as a larger and larger section of the joint has broken apart. When the remaining adhesive no longer withstands the forces imposed on it, it critically breaks apart and a rapid drop in the reaction force response is seen in the graphs.

The same response of the adhesive layer as modelled by the contact elements can also be seen from a different perspective in the contact stress plots in Figures 4.8-9. As expected the shear stress is concentrated to the edges of the adhesive zone (compare with Figure 2.3), but is somewhat unsymmetrical due to the dissimilar adherends. It is seen that debonding is initiated in the left end of the adhesive zone, and the crack propagates along the joint until a critical situation is reached where the remaining adhesive cannot sustain more loading (Figure 4.9). The connection between the cohesive law and the stress distribution is presented in Figure 5.1 where three distinctive phases of debonding are marked in both plots.
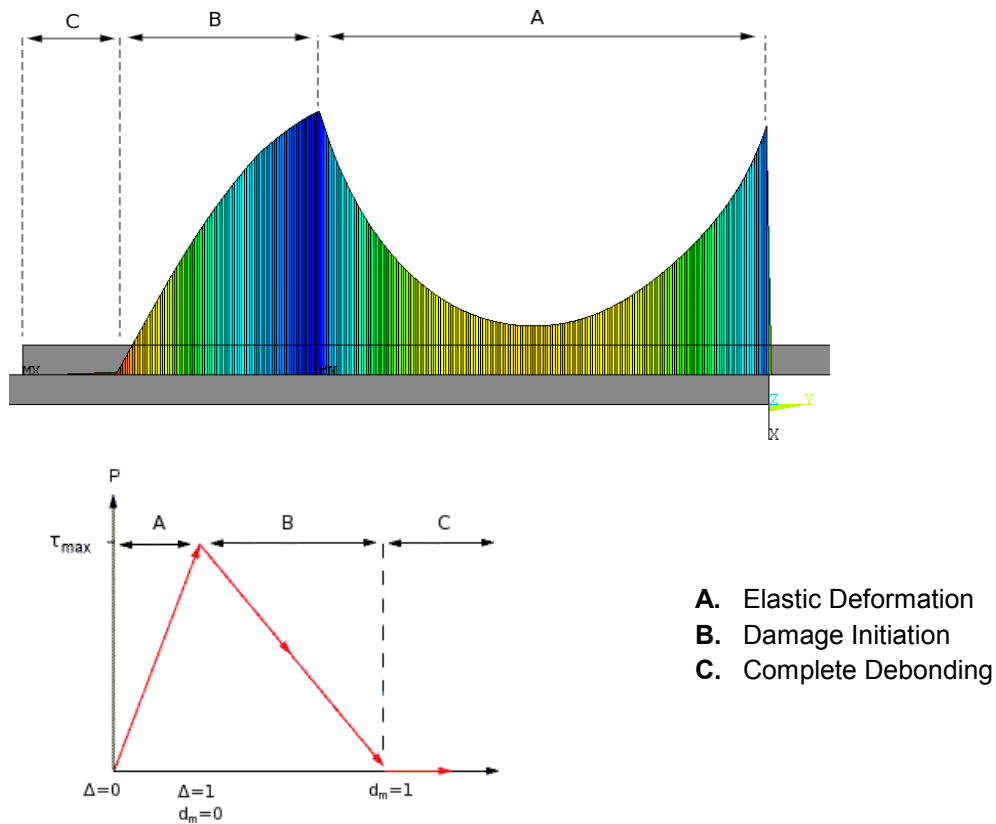
Figure 5.1. *Illustration of how the phases of the cohesive law affects the stress distribution of the contact elements during debonding.*

This same general behaviour can be seen in all of the test runs independent of the combination of parameters. As could be expected, the linear-elastic section is similar for all test runs with the same adherend geometry since the CZM parameters do not affect the material response of the adherends. It is not until the adhesive is damaged and starts to break up that the differences become apparent. To achieve a simple way of measuring the results of each run, the maximum reaction force is taken as a numerical value to use in the DOE calculations even though other factors have been taken into consideration when determining what final parameters to proceed with.

5.1.1 Comparison of FEA and Screening Test Results

Comparing the results to the experimental test results from Sicomp gives at hand that there are some differences in the response between the FE-models and the real test specimens (see Figure 5.2). Most notable is a significant difference in stiffness where the FEA results show a global stiffness of almost twice that of the real-life specimens (52 vs. 27 kN/mm). In addition to that the Sicomp samples also show less signs of the softening behaviour seen clearly in FEA, although there is, for two of the 50 mm samples, a "knee" on the curve at 1.5 mm displacement where a change in response stiffness takes place.
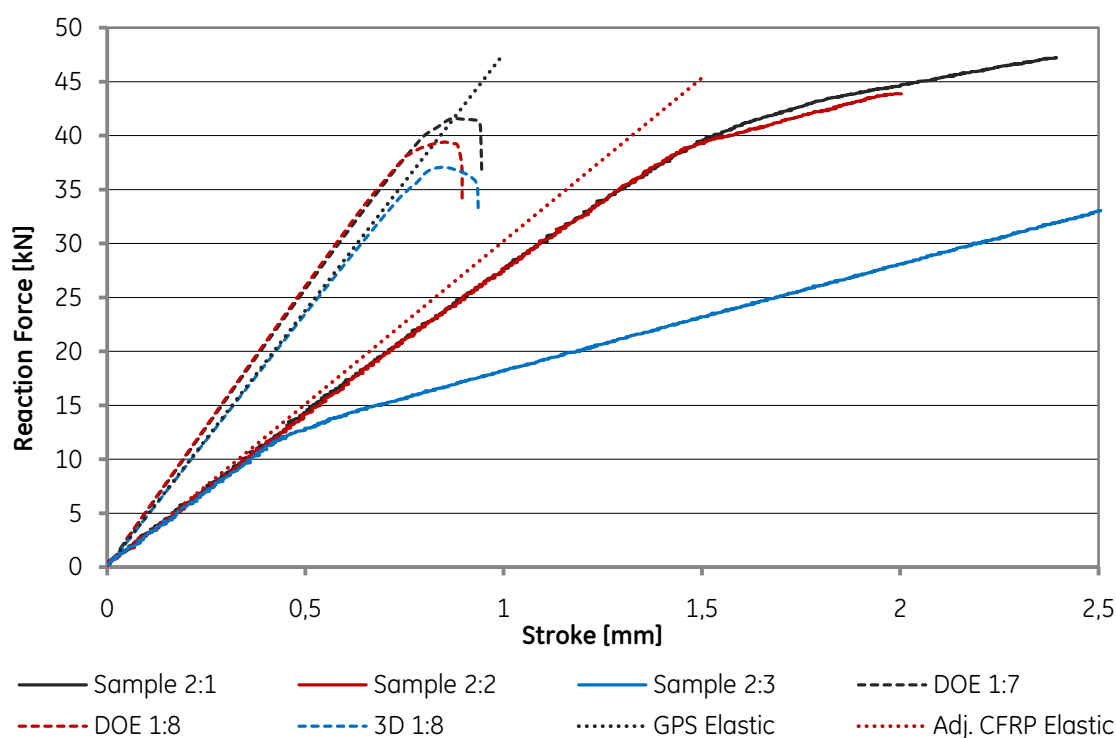
Figure 5.2 *Force-displacement results from CZM and elastic FEA compared to test results from screening test.*

Much work was done to investigate this difference in stiffness but no single factor could be found to easily explain the deviance. One contributing factor was that the simple plane strain assumption was not fully valid for the test specimens modelled. The three-dimensional speci-men model that was created and analysed for validation purposes shows a clear reduction in stiffness down to 47 kN/mm. As an explanation to this, the stress distribution results from the 3D analysis shown in Figure 4.11 reveals that the there are end effects towards the side edges of the adhesive layer that induces this deflection from the plane strain assumption. Had the assumption been fully true the stress distribution would have shown straight parallel bands across the layer rather than the curved bands that now can be seen.

An attempt was made to employ a more advanced type of FE-modelling using Generalised Plane Strain (GPS) method where the actual width of the modelled cross section is also taken into account. Unfortunately the contact elements used to model the adhesive did not support GPS and the method could not be used for a full test simulation. Despite this, an elastic model using the GPS elements was made where the adhesive layer was fully modelled and resolved with four elements over the layer thickness. Although not capable of predicting adhesive fail-ure, it too showed that the regular plane strain method overestimated the total stiffness of the specimen. The result of the GPS specimen model is included in Figure 5.2, denoted "GPS Elastic".

When further Sicomp test data was released, tests of a pure CFRP plate cut from the same laminate sheet as the DLJ specimens showed that the material data that was assumed for the

composite was incorrect. The test results show that the tensional modulus in the load direction was 42 GPa rather than 53 GPa, which is the value that was used in the FEA. Furthermore, results from another Sicomp analysis [36] suggested that strain in the part of the specimen that was clamped in the grips of the testing machine also affected the total displacement outcome. Taking the above mentioned effects into account a final elastic GPS analysis was set up to try to match the stiffness, resulting in the "Adj. CFRP Elastic" curve seen in Figure 5.2. The match was considered close enough and no further effort was put into analysing the stiffness.

5.1.2 Conclusions of the DOE

In this type of system, where many parameters are involved and interact in ways that are difficult to predict even with a thorough knowledge of the governing theories, a DOE approach can give good indication of the most important factors, and in which way changing them affects the result outcome. For the first set of DOE test the factors are all numeric, which makes it possible to calculate a main effect value for each of the factors and their combinations. The effect value can be interpreted as the gain on the results from increasing the value of the factor. The main effects for each single factor is found in the bottom row of Table 4.1 and are also presented in a Pareto chart (Figure 4.2) together with the effects from the factor combinations as well. A further presentation of the effects of the tested factors is shown in the main effects plot (Figure 4.3) where the levels of the factors are plotted against the results.
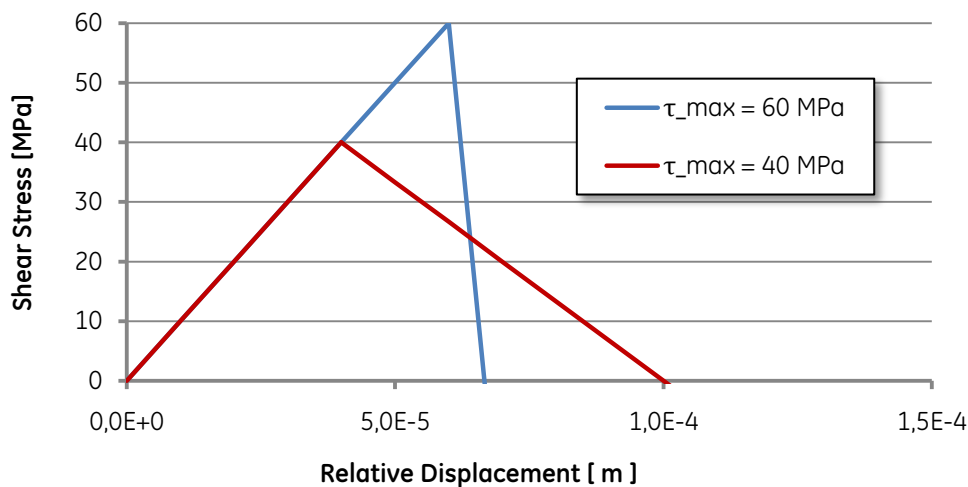
Figure 5.3. *Graph showing the tangential cohesive law at two levels of the maximum shear stress parameter. Other parameters at levels according to Table 4.3.*

From studying the effects of the material parameters it can clearly be seen that, as expected, the mode I fracture energy parameter G_{IIc} had a large positive effect on the outcome. What maybe was a bit more unexpected was that the tests showed a clear negative effect on the strength of the specimens from increasing the maximum shear stress factor of the adhesive, τ_{max}. The explanation probably lies in the shape of the cohesive law being altered so that there is no room for a softening damage behaviour and the adhesive breaks apart directly after the maximum shear stress is reached. This change can be seen in the plots of the tangential cohe-

sive law (Figure 5.3), where the higher τ_{max}-curve allows for very little additional displacement after the maximum shear stress value has been reached, provided that the fracture energy G_{IIc} is held constant.

Other than just looking at the effects of the single parameters, the interaction plot (Figure 4.4) gives an overview of the potential interactions between the factors. That is, if the level of one factor affects the effect on the result outcome of another. The graph lines are mainly parallel, indicating no interaction. The exception is the τ_{max} and G_{Ic} parameters that show some dependence; a high level of τ_{max} increases the effect of G_{Ic}, and vice versa. This can also be seen in the Pareto diagram of Figure 4.2.

The effects of the modelling parameters in the second DOE test matrix (Table 4.2) are a little bit harder to evaluate. Looking at the main effects plot (Figure 4.6) it is clear that changing these parameters does not have as a significant effect on the test result. The mean results only changes marginally with changing the individual factors. On the other hand there seems to be a more complex system of interactions between the factors. The interaction plot (Figure 4.7) shows a great number of interaction indications but, since the actual effects are so low, they are of lesser importance.

The final objective with both of the DOE's performed was to provide a base of understanding for deciding on what parameters to use for the studies of a metal-composite TED structure. The result of the DOE was a key element in the decision making, but other factors were involved as well. Especially when deciding on the modelling parameters recommendations from the ANSYS release documents, result consistency between different runs and computation time considerations also played a part. It should also be kept in mind that the goal was not to maximise the result parameter of the DOE tests but to match the specimen response in the FEA to that of the Sicomp screening tests.

Obtaining a perfect match at all three overlap lengths with one set of parameters proved to be a very difficult task. There were also some uncertainties about what actually happened in the tensile test at the "knee" seen in Figure 5.2. It was unclear if that was when the adhesive layer started to debond, and the remaining part was from the fracture zone going down into the composite, or if it was caused by the specimen sliding in the grips holding it. The final set of parameters presented in Table 4.3 is thus a compromise that yields bond strengths slightly higher than the tensile test results for 15 mm overlap lengths but around the level of the "knee" for 50 and 100 mm. A result comparison for all three overlap lengths is shown in Figure 4.10.

The "knee" in the result plot was later analysed by Sicomp and in the final report on the matter it was concluded that it was caused by sliding of the grips and that the actual strength of the 50 and 100 mm specimens was in the region of 45 kN. This was determined after analysing data from extensometers placed around the adhesive zone, away from the grips. These conclusions were however published after all the analytical work of this thesis had been done, and could thus not be taken into consideration.

5.2 Analysis of the TED Inlet Flange

The main purpose of the introductory analysis of the specimen models was to provide material parameters for the studies of the adhesive joints of a metal inlet flange attached to a composite main tube of a TED. The analysis took off where Sicomp's preliminary study ended by first validating the cohesive zone model used for the adhesive joint and the coupled-field thermal-structural model by remaking the analysis with the same geometry and loads as in the study. The results from these preliminary runs are presented in Figures 4.13-14 and show the temperature distribution and adhesive shear stress from Load Case 1 and plots of adhesive stresses and Δ-parameter from Load Case 2.
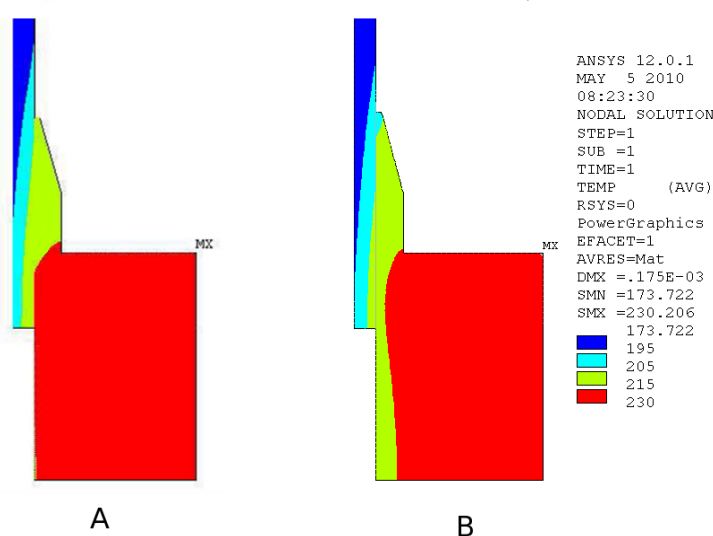
Figure 5.4. Comparison of the temperature distribution resulting from Load Case 1 from the Sicomp preliminary studies (A) and from the direct coupled CZM model (B). Temperature scale displayed on the right is valid for both plots.

The correlation of the results with those presented in the preliminary study was good for both load cases. The differences in the temperature field that are seen in the comparison in Figure 5.4 can be explained by the heat flux being modelled differently over the adhesive layer and that a more advanced, temperature dependent material model was used for the titanium. Also, the stresses in the adhesives showed a fairly good correlation in the transient load case, even though a higher degree of deviance than for the temperature was expected since the stresses were computed in an entirely different way. What can be seen is that the general shape of the curves is maintained, but there is a vertical translation and distortion of the results. A comparison of the normal/peel stresses plotted vs. time is shown in Figure 5.5, where it should be noted that point B (end-point near inlet) corresponds to point E in Sicomp's graph.

After only showing small result differences the analysis model was considered capable of handling the load cases involved in testing of the TED and further analyses of other, more optimised joint geometries could begin. Since no other load information was available, the use of the load cases from the preliminary studies was continued with the other geometries.
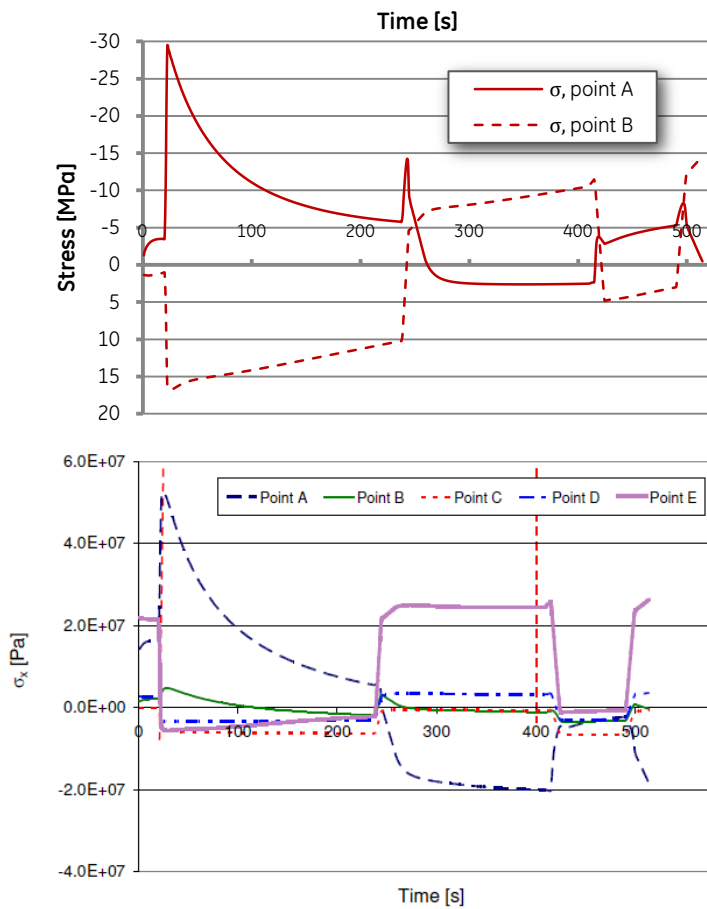
Figure 5.5. *Comparison of the peel stress levels during Load Case 2 between the CZM model (top) and the purely elastic model from Sicomp's preliminary studies (bottom). NB that point B in the top graph corresponds to point E in the bottom one.*

One of the important advantages with using cohesive contact elements to model the joint was that it includes a clearly defined failure criterion. As can be seen from e.g. Figure 5.1 the damage and failure behaviour can also be described by the two parameters Δ and d_m. This also allowed for convenient evaluation of the joint design concepts by looking at the maximum levels of these parameters. For the first analysis of the preliminary geometry, the Δ-plot (Figure 4.15) shows that the parameter value never goes above 0.6, it can be concluded that no damage would be caused to the adhesive joint as a result of the loads. Only when the Δ-parameter reaches 1 the adhesive can be considered to be damaged. Even after that, the damage parameter d_m needs to go from 0 to 1 before the contact elements start to break up locally – something that would not necessarily cause a complete failure of the joint.

5.2.1 Separate Load Analysis

When analysing the results from such a complex load case as Load Case 2 where thermal, pressure and structural loads interact it is valuable to have some level of understanding of the each load type's contribution to the final result. If for example, the pressure loads were to be completely dominating that would be useful knowledge when developing new joint concepts. To gain knowledge of the influence of each load type a series of tests were performed where only one type of load was applied to the model at the time.

Even though no interaction effects were included in this small study the results nonetheless proved interesting. The stress plot from the different runs (Figure 4.17) clearly shows that that the peaks observed in the shear stress curves are the result of thermal loading. Every time there is a sudden change in internal fluid flow in the TED, as described by the level of the film coefficient in the load sequence (Figure 3.9), there are high stresses induced in the adhesive as

a direct result of the increased temperature gradient in the radial direction. As the temperature approaches a steady-state condition these stresses decrease rapidly and the spikes observed in the thermal stress plot occur.

The pressure loads result in a more predictable stress pattern where high positive normal stresses arise directly in relation to the internal pressure. Also the static structural load results in positive stress levels, although considerably lower than those from thermal and pressure loads. What is more difficult to understand is the offset of the pressure reaction force curve, causing higher positive normal stresses when the internal pressure is low. Upon inspection, this was caused by an uncharacteristic stress distribution where the end elements showed a stress spike at lower loads. Since no physical explanation for this could be thought of, it was assumed that it was mainly caused by numerical issues in the FEA-setup.

 The important conclusions that can be drawn from this test are that the thermal loads cause the most severe effects on the joint by creating the peaks in the stress and Δ-parameter plots and that the influence of the structural loads is considerably less than expected and much lower than that of the pressure and thermal loads.

5.2.2   *Analysis of New Geometry Concepts*

After the FEA model had been confirmed by comparing to the results of the preliminary studies a series of design concepts of the joint cross section was produced and tested. The first step was to shorten the overlap lengths to make the incorporation of the joint with the TED cross section possible (see Figure 3.11). This 25 mm geometry was tested with both load cases just as for the longer 40 mm preliminary geometry so that a comparison could be made to study the effects of the shorter overlap.

5.2.2 - a *25 mm overlap Straight End*

First, it can be concluded that the cryogenic cooling test (Figures 4.13-14 and 4.18-19) seems to affect both the 25 and 40 mm geometries in a similar way. The temperature field is the same and the joint stresses are of the same magnitude. A calculation of the Δ-parameter over the surface reveals that the highest level reached during load case 1 is not more that around 0.35. As a result of the low dependence of the overlap length and the low stress level on the joint, it was then decided to focus only on Load Case 2 in the further studies of the joint geometries.
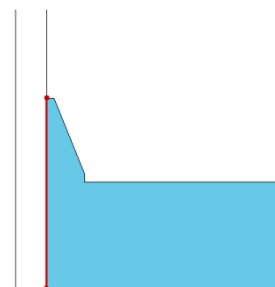
The results from Load Case 2 on the 25 mm straight end overlap (Figures 4.20-21) shows that the shorter joint is under a higher level of stress. Especially point B shows significantly higher levels of both shear and normal stress. However, the increase in normal stress is not that critical since a positive value of the adhesive normal stress σ indicates that the stress is caused by the adherends being pressed together rather than peeled apart. It has been suggested that a high stress level like this acts like a hydrostatic pressure on the adhesive and this could have a

negative impact on the load bearing capabilities. These effects are however not accounted for in this analysis.

Using the Δ-parameter as a measure of the combined loading effect on the joint, it can be seen that the higher values are shown throughout for point B while point A remains on roughly the same level. The maximum value of 0.59 occurs at point A at $t = 22.8$ s and the thus the final conclusion on the 25 mm straight overlap geometry is that it would sustain the loads from both load cases without any damage.

5.2.2 - b 25 mm Embedded Straight End

With the composite tube embedded into the flange, the geometry is theoretically feasible to use with the actual TED-geometry. As seen in Figure 3.11, the protruding inner stator interface flange that exists in the real TED is not modelled in the FEA model since it is not a loaded interface or structurally important. It does however create the need for an embedded joint cross section if a smooth inner surface is to be retained.
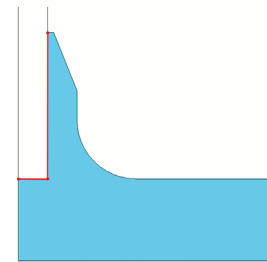
After analysing this joint concept under Load Case 2, it is clear that the adhesive on the end surface is severely stressed in peel, with a peak at 23 s when the engine starts up the first time and there is a high temperature gradient over the joint. The peel stresses come from the axial contraction of the composite which is what causes the main shear stress in the main adhesive surface. Looking at the stress plot in Figure 4.23 it can be seen that the normal stress line of the end surface (point C) follows the same pattern as the shear stress of the axial joint surface (points A and B).

Looking at the Δ-plot (Figure 4.22), the above mentioned peel stresses cause damage to the adhesive in point C and the damage parameter d_m is plotted to visualise the level of this damage. Since the damage is an irreversible process much like plastic deformation of a continuum solid, the d_m-parameter remains at 0.8 even after the stress is relieved. The damage parameter never reaches 1 so theoretically no debonding occurs, but a redesign of the joint is still warranted in order to keep the stresses at manageable levels throughout the joint.

5.2.2 - c Short Tapered End

A simple redesign was made of the embedded straight end joint to shift the loading on the edge surface over from the normal to the tangential direction. The stress result plot of the Load Case 2 run (Figure 4.25) shows that the alterations had the desired effect on the outcome; the peels stresses are lower while the shear stresses have increased to compensate. More of the load is now also taken by the main adhesive surface, which can be seen by the higher stress levels of point A and B.
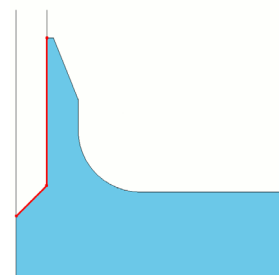
The effects of the changed geometry can clearly be seen in the Δ-plot (Figure 4.24) where the maximum parameter value now is around 0.8 and no damage is sustained. Point C is still under high stress, but the moderate stress levels over the main adhesive surface makes this geometry a feasible alternative for use in further studies.

5.2.2 - d Fully Tapered

After consulting composite manufacturers with experience of fitting metal flanges to composite tubes, it was learned that a fully tapered joint was preferable from a manufacturing point of view. When curing the adhesive it is desirable to keep the joint under a constant pressure to obtain optimal joint strength. The conical shape of the adhesive surfaces with a tapered cross section means that this can be achieved simply by applying axial pressure under proper alignment during the curing. Since making the composite tube with a perfectly sharp edge is not possible, a small end surface has been left also in the model although it has not been modelled with contact elements. In the actual joint, this would also help to adjust small radial mismatches between the parts as a small gap between the mating surfaces would be filled out with surplus adhesive.
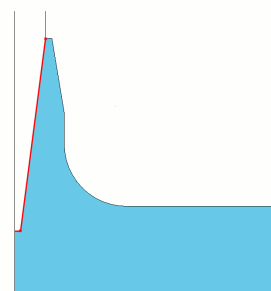
Strength-wise the tapered joint also shows to be very capable with low stresses measured at both points during the analysis (see Figure 4.27). The only concern is the there seems to be a negative trend during the load cycle in the point B stresses and during the course of the test they go further and further down the negative scale. This means an increase in peel stress and results in a clearly positive time-derivative for the Δ-curve (see Figure 4.26). The question is why these increasing stresses appear when none of the load variables show and such a trend (see Figures 3.7-9). The most likely scenario is that this is caused by transient temperature effects that develop over time but more specific testing would be needed to answer the question definitely. The risk with this behaviour is of course that the increase in peel stress continues and peaks at an unknown value after the load sequence ends. To accurately investigate this, a prolonged test sequence would be needed with data of how the internal bulk temperature rises after the current load sequence has ended.

Despite the uncertainties about the development of thermal stresses described above, the tapered joint cross section emerged as the most suitable choice for the TED application. The adhesive stresses were kept at moderate levels as well as the production feasibility was increased by choosing a joint type that is used in the industry today.

5.3 Analysis of the 3D Flange Model

The main reason for performing the 3D analysis was the possibility to apply the asymmetric loads that the TED is subject to under actual flight operation. These were suspected to be more damaging to the adhesive due to bending moments that could cause local peel stresses. There were also uncertainties about how well the structural loads used in the axisymmetric analysis reflected the real in-flight loads, especially since it was seen that the structural load had such a minor influence on the total result.

The extraction of reaction forces by using a master node and rigid connections to the nodes on the cut surface should provide a good representation of the forces acting on the flange section. What compromises the results in this case is that a TED constructed completely of Inconel 718 has a different structural stiffness than a hybrid design of Ti 6Al-4V and carbon fibre composite. This leads to the reaction forces from interface loads being differently distributed. An attempt to correct this would likely require an entirely new FE-model to be built, which would be very time consuming, and outside the scope of this thesis.

Table 5.1. *Reaction forces and moments for the inlet flange section extracted from the Inconel 718 full TED model.*

F_x [kN]	F_y [kN]	F_z [kN]	M_x [Nm]	M_y [Nm]	M_z [Nm]
[CONFIDENTIAL INFORMATION]					

Using the set of loads extracted from the full Inconel 718 model (Table 5.1), the first analysis made was a simple static run with only these extracted structural loads applied. The purpose was mainly to test how severely the bending moments M_x and M_z affect the adhesive. Contour plots of the adhesive normal and shear stresses (Figures 4.29-30) show that, especially for the shear stress, local maxima exists were the stress levels are very high (14 MPa compared to 6 MPa in the axisymmetric case). The peel stresses were however not as bad as feared and only reached up to about 1.3 MPa. The mixed mode effects of both normal and shear stresses combined are shown in the Δ-parameter contour plot (Figure 4.28). The maximum of the Δ-plot coincides geometrically with that of the shear stress plot, so there seems to be little interaction between the stresses in this case.

It was decided that analysing the 3D-model with the same mesh resolution as the axisymmetric models would be far too time consuming to be justifiable within this project. Instead a submodelling technique was employed where two separate FE-models were used – a coarsely meshed full model (Figure 3.16) and a more detailed submodel consisting of an angular section cut out of the full model geometry (Figure 3.17).

A single transient run using the coarse model was performed using the pressure and thermal loads from the axisymmetric Load Case 2 together with the structural loads from Table 5.1. The results from this run are shown in figures 4.31-32 and shows a pattern comparable to that of the axisymmetric analysis of the same joint geometry, although without as distinctive peaks at the thermal transition points. What can seem remarkable at first is that even though the

structural loads had a more significant effect on their own in the static 3D case, the combined result of structural and transient loads is a lower stress maximum. The reason for this is that the coarse mesh in the full 3D model does not fully resolve the local stress concentrations resulting in the stress "peaks" being cut off.

Since the magnitude of the stress results of the coarse model is not reliable, the main purpose was to locate the time and position of the stress maxima and analyse them further using the submodel. The most critical point was chosen at the time where the highest Δ-value was measured ($t = 489$ s, marked with a red vertical line in Figure 4.31). At this time the contact surface was analysed and the coordinates of the Δ-maximum (marked as MX in Figure 4.30) were extracted.

Since the submodel was analysed as a static load case with loads and BC's directly imported from the right time step in the transient analysis, only single scalar values were obtained for the maximum Δ-values and stresses. These are for the sake of comparison included in the transient plots for the coarse model and clearly show that a higher maximum values are obtained with a sufficiently refined contact mesh. To gain understanding of what the result would have been with a transient analysis of a finely meshed model a scaled copy of the Δ-plot from the coarse model is also included in the graph. The values have simply been scaled to match the Δ-value from the submodel at $t = 489$ s.
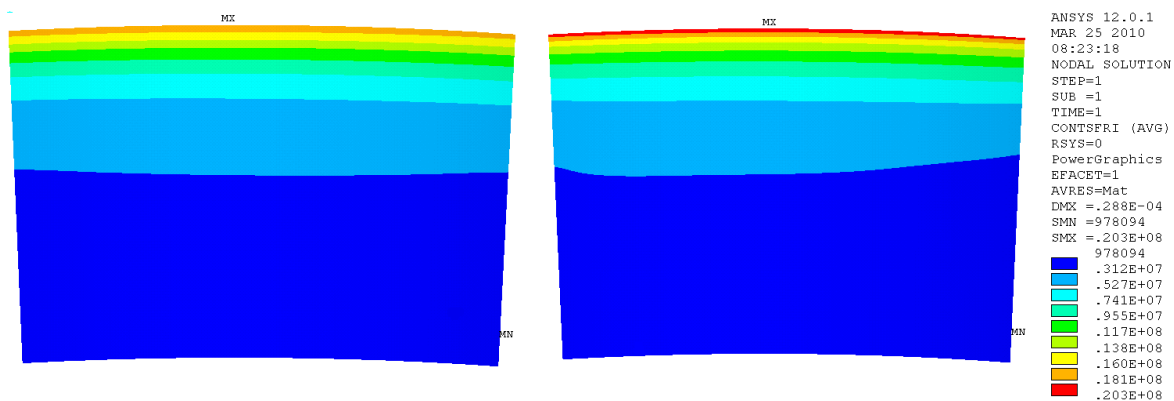
Figure 5.6. *Comparison of the adhesive tangential stress on contact surface of the submodel (right) and the corresponding section of the coarse model (left).*

A validation that the submodel actually is a true representation of the same area of the coarse model at the same time under the same load case, can be done by checking that the stress distribution next to the stress concentration and the location of the concentrations match between the models. Figures 5.6 -7 show the contour plots of the same area of the coarse model and the submodel next to each other on the same scale and it is clear that, in both cases, there is an adequate match between the stress distributions away from the edges. The submodel can be validated further by noting that maximum value of the Δ-parameter occurs at the centre of the top edge of the contact surface in Figure 4.33, as this section was chosen because it was centred on the stress concentration in the coarse model.
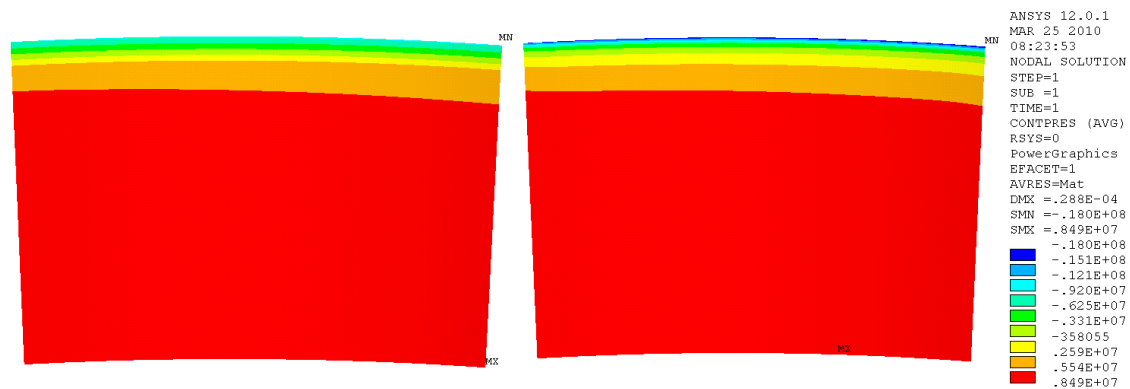
Figure 5.7. *Comparison of the adhesive tangential stress on contact surface of the submodel (right) and the corresponding section of the coarse model (left).*

The more detailed results from the submodel still do not show any excessively high stress levels compared to the axisymmetric or the static 3D case. Combining all load types in the 3D case apparently did not lead to a linear superposition of the stresses but instead a result where the overall stresses were slightly lower than in the axisymmetric analysis. An important factor in reducing the effects of the static bending moments was discovered to be the high internal pressure pushing the adherends together and thereby reducing the peeling effects. A potentially dangerous case could thus be, if static and thermal load were applied without an internal pressure. However, this is not a likely scenario since both the high thermal convection and the internal pressure are the result of cold gaseous hydrogen passing through the TED and so one of them would not likely appear one on its own.

5.4 Analysis of Cryogenic Properties

The temperature-dependent material model that was used to simulate the cryogenic tensile tests was based information about cryogenic behaviour of DLJ joint both from literature sources and Sicomp's experiments, together with assumptions of the reactions on the parameter levels. The results of the simulated tensile tests (Figure 4.36) show that a severe reduction of the joint strength, comparable to that seen Sicomp's results, is obtained for the 50 and 100 mm overlap lengths. The shorter 15 mm overlap does not show a quite as dramatic decrease, not even relative to its original strength. The decreases in joint strengths are -45% for the two longer overlap lengths and -30% for the 15 mm specimens putting them somewhere between the severe decreases of Sicomp's specimens and the more moderate figures found in other scientific articles (see Table 3.6 for a comparison).

A perfect match with Sicomp's results was not considered absolutely necessary since they so noticeably differed from the other test results published. Other articles with results of cryogenic test of metal to composite joints even saw an increase in bond strength at -150 °C [34]. The more cautious decrease of joint strength observed with the new material model was thus believed to be sufficient for proceeding with tests of the TED geometry.

To be more time-efficient the new temperature-dependent material model was tested on the 2D axisymmetric model during a full run with Load Case 2. The adhesive stress response of the 2D and 3D models were comparable in the previous analyses, and since the axisymmetric model actually showed a higher stress level it was also considered a more conservative choice.

The results from this test are presented in Figures 4.38-39 and shows relatively low influence from the new material parameters. The only apparent difference when comparing to the corresponding results with the old material model (Figures 4.26-27) seems to be a slight increase of the stress levels in point B and an according increase of the Δ-parameter. Part of the explanation to this low influence could be that the temperature in the joint never reaches temperatures comparable to those experienced in the cryogenic tensile tests. A plot of the nodal temperatures at points A and B during the analysis (Figure 4.37) shows that the temperature keeps to about -60 °C (~210 K) for most of the test sequence and never reaches lower than -90 °C.

It is also worth mentioning that the stress inducing effects of different thermal expansions of the adherend materials were already included in the first analysis of the TED geometry but not in the first tensile test analyses since these were performed at uniform room temperature. This too contributed to the greater strength reduction seen in the latter.

It could be argued that it is not fair to compare an ultimate strength test with the stresses from a load case simulation and in one sense it is true that they are two different things being compared. On the other hand, the stress level and the Δ-parameter give a good enough representation of the state of the joint to justify the comparison. Either way these results do show that the adhesive joint of the TED inlet flange is strong enough not to be damaged from the loads caused by engine usage.

5.5 Potential Weight Savings

The reason why a composite design of the TED was first considered was because of the weight saving possibilities. In spaceflight, every kilogram saved in the carrier structure allows for another kilogram of precious cargo to be delivered into orbit. Calculations show that the estimated cost of delivering cargo to GTO with the Ariane 5 launcher is as high as $11,000 per pound or $24,000 per kg [37] meaning that even relatively small weight reductions can be financially justifiable.

Weight estimations of a number of different TED configurations have been made and the figures are presented in Table 5.2 below. Conclusions from the estimated weights of the different TED designs are that, relative to the current Inconel 718 design, a 57% weight reduction from 7.7 to 4.3 kg would be obtained with a titanium/composite model. However there is a TED made entirely out of Ti 6Al-4V under development at the moment, and even though the structure probably would need some reinforcement, the lower density of titanium means that a serious weight reduction would be the outcome.

Table 5.2. *Estimated weight of various TED designs*

Material Configuration	Estimated Mass [kg]
Ti 6Al-4V/Composite	3.3
Inconel 718	7.7
Ti 6Al-4V	4.3
Composite only	1.5

Comparing the titanium-composite hybrid design that has been analysed in this report with the proposed titanium design the weight saving is reduced considerably to around a single kilogram, making the competition difficult for the likely more development-costly hybrid design. The current TED geometry holds so much of its volume in the flange sections that keeping these made of metal yields only a relatively low weight reduction. The full potential of using composites is therefore only realised if these too can be made out of some sort of composite material. A suggested alternative is using a hybrid laminate technique where some layers in the composite laminate are replaced by thin titanium sheets to increase bearing strength and provide a metal flange surface. This technology is currently under investigation in the KOMET 2 research project which is the direct sequel of the KOMET project hosting this thesis.

6. Conclusions

This chapter contains a summary of the most important results and their importance to the outcome of the project. Guidelines for the most relevant future work within the subject are also laid out and included under this headline.

6.1 CZM Analysis of Adhesive Joints

Using a Cohesive Zone Model approach is a powerful alternative when analysing the complex process of adhesive debonding. The major benefit is that the entire process from crack initiation to complete debonding through elastic displacement and damage/softening of the adhesive is included in the model and can be handled in a single analysis. No crack-tip elements or similar is needed as in other LEFM-based methods and the location of the initiation of fracture, or debonding, is also determined by the FE model. CZM provides a clear failure criterion included in the cohesive law that makes it possible to analyse both partial and complete debonding.

As experienced in this report, one of the disadvantages is that a CZM analysis requires material parameters specialised for the joint configuration in question, that typically are not available in literature. Acquiring these parameters through testing is not particularly difficult, but the procedures, although mostly standardised by ASTM and ISO, still require resources and competence not available everywhere. As has been shown by this report, determining material parameters indirectly through e.g. tensile tests is a possible way to go, but must still be considered a secondary alternative to dedicated experimental testing. Another limitation to CZM worth mentioning is that the debonding only occurs along the plane defined by the cohesive zone elements. This is usually not an issue when modelling adhesive joints but can be bothersome when modelling composite adherends where the crack can advance into the layers of the composite.

For an analysis case such the TED, where the severity of the stresses in the adhesive is not known, the CZM approach has worked well and provided dependability in the sense that the same FE-model can be used no matter if the adhesive layer would debond completely or be barely stressed at all. In retrospect, knowing that stress levels were fairly low, a simpler elastic model of the joints could have been an alternative since the damage modelling capabilities of the cohesive zone model were hardly used at all.

6.1.1 Review of the Analysis Procedure

Performing an FE-analysis using a CZM methodology differs in some ways from a regular elastic analysis and there are a few crucial steps that need to be included. Based on the analyses in ANSYS that have been performed in this project, a brief review of the most important steps has been concluded:

1. Obtain material data that is valid for the joint that needs to be analysed. The material parameters contain information about the fracture behaviour of the entire joint and are thus specific to a certain configuration of adherends and adhesive.
2. Define the adhesive surfaces of the FE-model and adjust mesh size of the underlying solid to provide a suitable mesh size for the contact elements. In ANSYS, these are overlaid on the solid mesh and share the same nodes. At the same time care must be taken to keep the mesh size small enough to adequately resolve the stress concentrations in the adhesive.
3. Create a CZM material model to use with the contact elements. The material data is entered into a data table using the `TB` command, somewhat differently than for other material data. Note that the contact stiffness and temperature conduction parameters are entered separately as a `REAL` constant set.
4. Set appropriate parameters for the contact element type. The right `KEYOPTS` must be set to have the contact elements correctly model a bonded contact instead of e.g. friction contact.
5. Mesh contact surfaces with contact and target elements. Mind which surface is meshed with contact elements as this may affect the results.
6. Apply loads and boundary conditions to the FE-model as usual.
7. Solve, but be aware that the time step size affects the solution through the artificial dampening coefficient.

6.2 Feasibility of a CFRP/Metal TED Design

The main question to answer within this thesis has been "Will the adhesive joints of the TED flanges hold?" Judging from the results obtained from both the axisymmetric and 3D analyses the only possible conclusion is that the joint will sustain the stresses from both thermal and mechanical loading without taking any significant damage. There are of course aspects regarding this that has not been covered by this report, but with the assumptions and analysis methods used herein the results unanimously point to the conclusion that adhesive joining of metal flanges to a composite main body is a feasible design option.

Provided that the CFRP structure can be manufactured to the geometry that is required, the tapered tubular joint should provide a joint geometry that is possible to assemble and cure with conventional methods. The production factors have only been covered very briefly within the report, but some effort has been put into choosing a joint type that can be manufactured to the standards required by the application.

On the subject of weight savings it is difficult to say if the proposed metal-composite design can be a profitable alternative without a more thorough cost analysis. It is clear that it will be difficult to compete with the titanium design without improving the weight reduction results, but it has also been confirmed that there is potential in combing metal and composite through adhesive joining; something that can perhaps prove useful in other design concepts. A possibility is also that the titanium concept proves difficult to realise due to the negative effects of hydrogen gas on the titanium. If the titanium should prove to become too brittle because of the hydrogen, a composite design of the main body may be the only remaining alternative to drastically reduce the weight of the TED.

The question if it is possible to design a TED mainly out of carbon fibre composite cannot be answered solely from the results of this thesis, but at least some critical questions on the way have been answered and plans can now be made for further analyses of the matter.
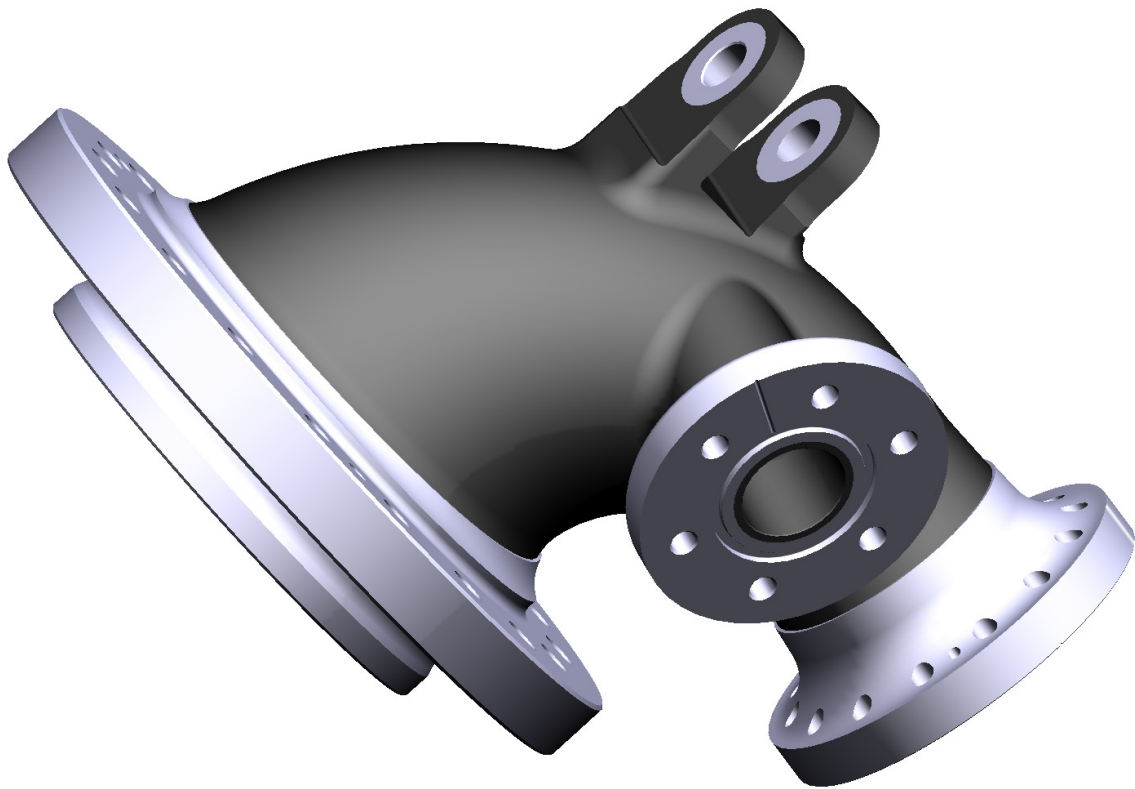
Figure 6.1. *A rendered 3D image of what a metal-composite TED design could look like.*

6.3 Further Research Options

This project considered one of the first steps toward designing a metal-composite hybrid design of the TED. If the concept should be realised a lot of work remains before a working prototype can be constructed. The following section covers some of the more important topics that have emerged during the work with this project.

More reliable material data is needed for a final conclusion on the strength of the adhesive joints. Ideally, specialised testing to obtain the parameters needed for the CZM FE-model should be performed with test specimens made of the material used and perhaps also at low temperatures (although as low as -150°C might not be necessary). If the parameters obtained by such experiments were to differ too much from the ones used in this report, the results presented herein would need to be adjusted accordingly.

The design of the composite tube needs to be investigated further. Which geometries are possible to produce with e.g. resin transfer moulding and/or filament winding? How does a bent composite tube react to the thermal loads in terms of deformation and induced stresses etc? How thick does the composite laminate have to be to contain the high internal pressure?

As mentioned in the Discussion chapter, the 3D load case used for the structural loads on the flanges is only validated for an Inconel 718 design. To perform further reliable studies, work should be done on obtaining structural loads that are based on the stiffness of a metal-composite design. This includes producing an FE-model of the full TED geometry. A potentially severe problem with the composite design that has not been discussed in this report is the engine support interface on the back of the TED. A solution on how to incorporate this interface into a composite design is vital in order to realise a functional prototype.

The next step in analysing the adhesive joints of the flanges would be to manufacture samples of the flanges and analyse the strength through experimental testing. This would give a more direct answer to the question of the joint strength, but not yield much information about internal stresses etc. It also seems like the only truly reliable way to analyse the influence of cryogenic temperature on the joint strength.

A factor that has not been considered when analysing the adhesive in this project is the how it is affected by fatigue. Since the Vinci engine is not designed for prolonged, continuous use it is mainly the low-cycle fatigue (LCF) properties that would be of interest, even though the specified dynamic load cases also include cyclic vibrations for high-cycle fatigue testing. Some research has been done on the subject and is available in literature [38] [39] [40], but for more than learning the general behaviour of the adhesive, testing of the specific joint configuration is needed.

7. References

[1] WIDFELDT B AND FRYKLUND F, Eds., Flygmotor - Volvo Aero 1930-2005. Nässjö, Sweden: Air Historic Research, 2005.

[2] SAFRAN GROUP, "Vinci on Track," SAFRAN Magazine, pp. 36-38, January 2010.

[3] VOLVO AERO CORPORATION. (2009) Introduction to Turbines & Rotors Department. Presentation.

[4] MATTSON D, LUNDSTRÖM R AND EMAN J, "Preliminary studies of typical stresses in composite to metal joints for aerospace applications," CR09-25, Swerea SICOMP, Piteå, 2009.

[5] BHOWMIK S, BENEDICTUS R, POULIS J A, BONIN H W AND BUI VT, "High-performance nanoadhesive bonding of titanium for aerospace and space application," International Journal of Adhesion & Adhesives, 2009, **29**:259-267.

[6] TOMBLIN J S, YANG C, and Hartner P, "Investigation of Thick Bondline Adhesive Joints," DOT/FAA/AR-01/33, U.S. Department of Transportation, Washington, DC, 2001.

[7] JANSSON N, "Method for Estimation of Ultimate Strength of Adhesive Joints," VOLS:10097121, Volvo Aero Corporation, Trolhättan, 2010.

[8] ADAMS R D, Comyn J, and Wake W C, Structural Adhesive Joints in Engineering, 2nd ed. London, UK: Chapman & Hall, 1997.

[9] VOLKERSEN O, "Die Nietkraftverteilung in zugbeanspruchten Nietverbindungen mit konstanten Laschenquerschnitten," Luftfahrtsforschung, 1938, **15**:41-47.

[10] GOLAND M AND REISSNER E, "The Stresses in Cemented Joints," Journal of Applied Mechanics, ASME, 1944; **66**:A17-A27.

[11] TORSTENFELT B, Finite Elements - From the Early Beginning to the Very End, Preliminary ed. Linköping: Linköpings Univeristet, 2007.

[12] HUGHES T, The Finite Element Method: Linear Static and Dynamic Finite Element Analysis.: Dover Publications, 2000.

[13] HARRISON N L AND HARRISON W J, Journal of Adhesion, 1972; **3**:195.

[14] WOOLEY G R AND CARVER D R, Journal of Aircraft, 1971; **8**:817.

[15] SCHMIDT P, "Computational Models of Adhesively Bonded Joints," Linköping University, Linköping, PhD Thesis 2007.

[16] GRIFFITH A A, "The phenomenon of rupture and flow in solids," Philosophical Transactions of the Royal Society, 1921; **221**:163-198.

[17] IRWIN G R, "Analysis of stresses and strains near the end of a crack transversing a plate," Journal of Applied Mechanics, 1957; **24**:361-366.

[18] ANDERSON T L, Fracture Mechanics - Fundamentals and Applications, 3rd ed. Boca Raton, FL: CRC Press, 2005.

[19] ALFANO G AND CRISFIELD M A, "Finite element interface models for the delamination analysis of laminated composites: mechanical and computational issues," International Journal for Numerical Methods in Engineering, 2001; **50**:1701-1736.

[20] GUESS T R, REEDY E D, AND STAVIG M E, "Mechanical Properties of Hysol EA-9394 Structural Adhesive," SAND95-0229, Sandia National Laboratories, Albuquerque, NM, 1995.

[21] MATTSSON D, "Description of manufacturing and tests performed within the KOMET project," CR09-062, Swerea SICOMP, Piteå, 2009.

[22] "Standard test method for strength properties of double jap shear adhesive joints by tension loading," ASTM D3528-96 , 1996.

[23] GUNAWARDANA S, "Prediction of failure initiation of adhesevely bonded joints using mixed-mode fracture data," Wichita State University, Wichita, KS , M Sc Thesis 2003.

[24] EDGREN F, "Specification for application of composite to metal joint in engine environment," VOLS:10075712, Volvo Aero Corporation, Trollhättan, 2009.

[25] MAGNUSSON K, "Material Specification: Forged Ti 6Al-4V," VOLS:10086015, Volvo Aero Corporation, Trollhättan, 2009.

[26] LANGLOIS V, "Specification of selected external load cases for the partial structural justification of the exhaust casing of the Vinci hydrogen turbopump," Snecma Moteurs, Vernon, 2007.

[27] ANSYS INC. (2007) ANSYS 11.0 Release Documents. Chapter 9.1 Submodeling.

[28] KIM M-G, KANG S-G, KIM C-G, AND KONG C-W, "Tensile response of graphite/epoxy composites at low temperature," Composite Structures, 2006; **79:**84-89.

[29] KIM M-G, KANG S-G, KIM C-G, AND KONG C-W, "Tensile properties of carbon fiber composites with different resin compositions at cryogenic temperatures," Advanced Composite Materials, 2010; **19:**63-77.

[30] REED R P AND GOLDA M, "Cryogenic properties of unidirectional composites," Cryogenics, 1994; **34**(11):909-928.

[31] GRAF N A, Schieleit G F and Briggs R, "Adhesive bonding characterization of composite joints for cryogenic usage," Lockheed Martin Space Systems, New Orleans, LA,.

[32] SHIMODA T, HE J, AND ASO S, "Study of cryogenic strength and fracture behaviour of adhesives for CFRP tanks of reusable launch vehicles," Memoirs of the Faculty of Engineering, Kyushu University, 2006; **66**(1):55-70.

[33] BARTOSZYK A, JOHNSTON J, KAPERIELAN C, AND KUHN J, "Design/analysis of the JWST ISIM bonded joints for survivability at cryogenic temperatures," Proceedings of SPIE, 2005; **5868:**1-10.

[34] KANG S-G, KIM M-G, AND KIM C-G, "Evaluation of cryogenic performance of adhesives using composite-aluminium double-lap joints," Composite Structures, 2007; **78:**440-446.

[35] LUNDMARK P AND MATTSON D, "Mechanical testing of the composite-titanium joint studied in the KOMET project," CR10-017, Swerea SICOMP, Piteå, 2010.

[36] ANDRÉ A, "KOMET project results from FE models - cohesive modelling," Swerea SICOMP, Gothenburg, Presentation 2009.

[37] FUTRON CORPORATION, "Space transportation costs: Trends in price per pound to orbit 1999-2000," Bethesda, MD, 2002.

[38] AZARI A, PAPINI M, SCHROEDER J A, AND SPELT J K, "Fatigue theshold behavior of adhesive joints," International Journal of Adhesion & Adhesives, 2009; **30:**145-159.

[39] MENEGHETTI G, QUARESIMIN M AND RICOTTA M, "Influence of the interface ply orientation on the fatigue behaviour of bonded joints in composite materials," International Journal of Fatigue, 2010; **32:**82-93.

[40] ABDEL WAHAB M M, HILMY I, ASHCROFT I A, AND CROCROMBE A D, "Evaluation of fatigue damage in adhesive bonding: Part 2: Single lap joint," Journal of Adhesion Science and Technology, 2010; **24:**325-345.

Appendix A

A-I. Cross section of the Vinci hydrogen turbo-pump
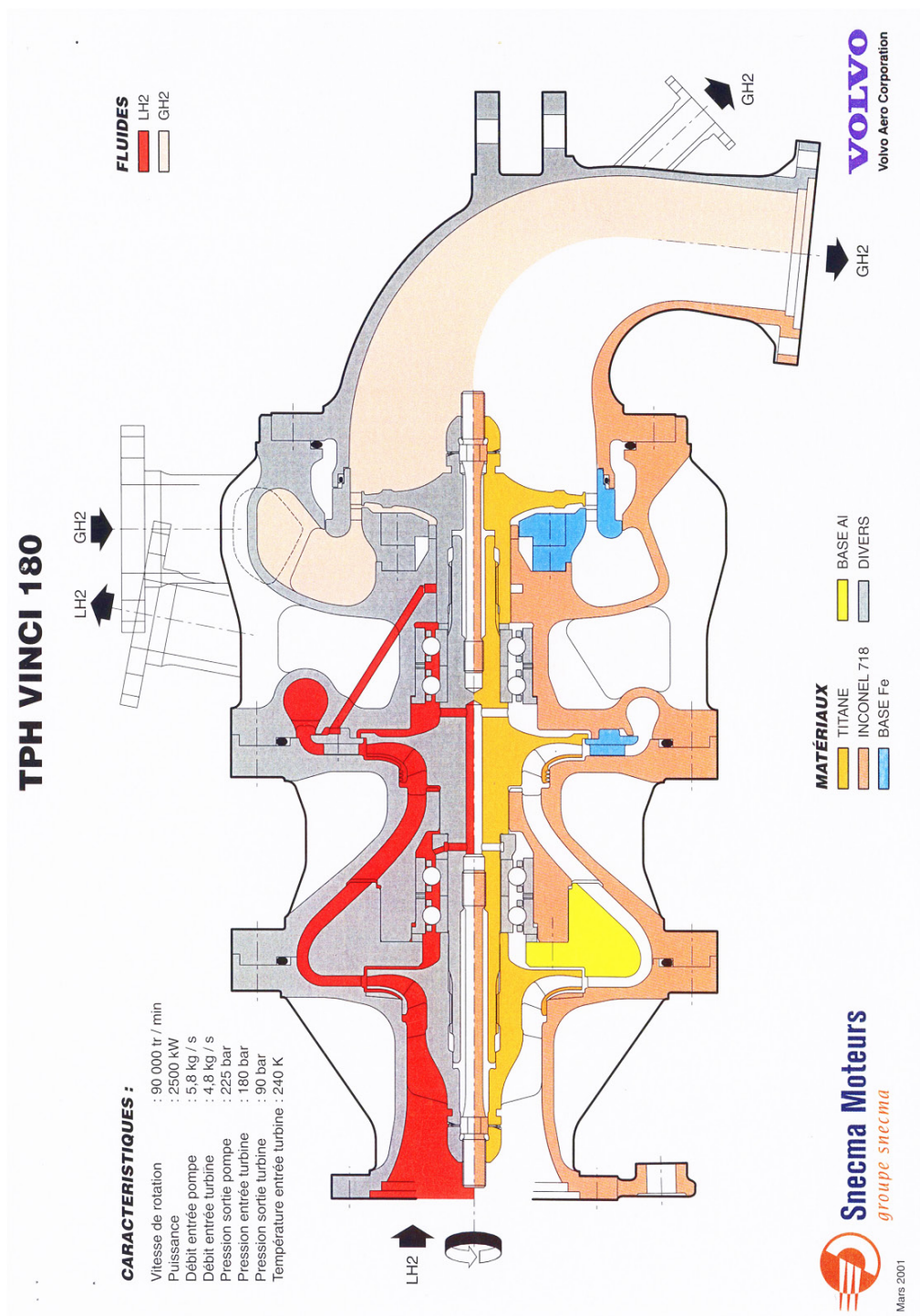
A-II. Flow chart of the Vinci engine (only lower stages shown)
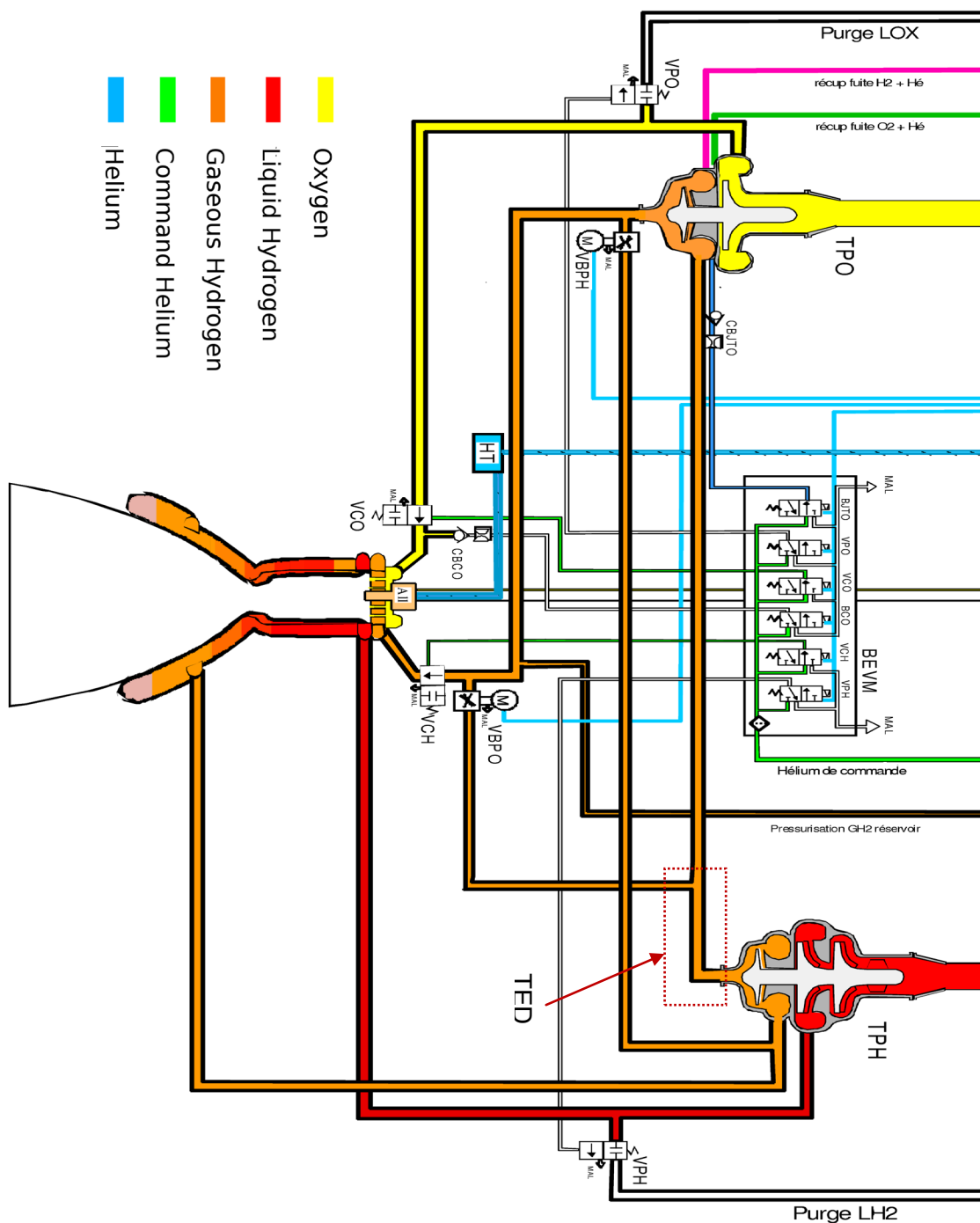
Appendix B

B-I. ANSYS Code Sample – Tensile Test Specimen Analysis

```
/COM, *********************************************************************
/COM, ***            CZM-Modelled Double Lap Joint Specimen           ***
/COM, *********************************************************************
/COM, --  File: 1-8_100.ans
/COM, --  Date: 2010-02-16
/COM, --  Creator: Fredrik Fors, Dept. 6670
/COM, --  Project: Exjobb KOMET
/COM, --
/COM ********************************************************************

/FILNAME,1-8_100,1
/prep7

/com,!-------------------------------------------------------------------------
/com,!   Parameters
/com,!-------------------------------------------------------------------------

pi=acos(-1)
*SET,L_A,0.1        !length of adhesive zone
*SET,L,0.0635       !adherend total length
*SET,T,0.002        !adherend thickness
*SET,E,4e9          !adhesive tensile modulus
*SET,G,1.46e9       !adhesive shear modulus
*SET,T_A,0.2e-3     !adhesive thickness

/com,!-------------------------------------------------------------------------
/com,!   Geometry
/com,!-------------------------------------------------------------------------
!keypoints
K,1,0,0,0
K,2,0,-L_A-0.005,0
K,3,0,-L-L_A,0
K,4,-T,L,0
K,5,-T,0.005,0
K,6,-T,0,0
K,7,-T,-L_A,0
K,8,-T,-L_A-0.005,0
K,9,-T,-L-L_A,0
K,10,-2*T,L,0
K,11,-2*T,0.005
K,12,-2*T,-L_A,0

!Areas
A,8,2,1,6
A,9,3,2,8
A,12,7,5,11
A,11,5,4,10

/com,!-------------------------------------------------------------------------
/com,!   Mesh
/com,!-------------------------------------------------------------------------

!Element type definitions
ET,1,PLANE182,
KEYO,1,3,2                  !plane strain behaviour
ET,2,TARGE169
```

```
ET,3,CONTA171,,1              !Penalty function method
KEYO,3,9,1                    !exclude initial penetration
KEYO,3,10,0                   !redefine pair contact stiffness at load step
KEYO,3,12,5                   !always bonded contact

!Materials def
MPTEMP,1,293
MPDATA,EX,1,,114e9  !Titanium
MPDATA,PRXY,1,,0.33

MPDATA,EX,2,,10.1e9 !orthotropic CFRP
MPDATA,EY,2,,52.9e9
MPDATA,EZ,2,,52.9e9
MPDATA,PRXY,2,,0.056
MPDATA,PRYZ,2,,0.317
MPDATA,PRXZ,2,,0.056
MPDATA,GXY,2,,3.69e9
MPDATA,GYZ,2,,20.1e9
MPDATA,GXZ,2,,3.69e9

TB,CZM,3,1,,CBDE    !CZM adhesive
TBDATA,1,44.5e6,425,40e6,2000,0.005,1 !Adhesive mtrl parameters

!AREA ATTRIBUTES
ASEL,S,AREA,,1,2
AATT,2,,1
ASEL,S,AREA,,3,4
AATT,1,,1
ALLSEL

!AREA MESH SIZES
AESI,1,0.0005
AESI,2,0.0005
AESI,3,0.0005
AESI,4,0.0005

!meshing areas
MSHK,1
AMES,1,4,1
LREFINE,4,9,5,1,1,CLEAN,ON  !refine at bond line

!Contact Zone Mesh
REAL,1
TYPE,2  !Target surface mesh
MAT,3
LSEL,S,,,4
NSLL,S,1
ESLN,S,0
ESURF

TYPE,3  !Contact surface mesh
LSEL,S,,,9
NSLL,S,1
ESLN,S,0
ESURF
RMODIF,1,3,-2e13    !Set normal penalty stiffness
RMODIF,1,12,-1e12   !Set tangent penalty stiffness
ALLSEL
```

```
/com,!-------------------------------------------------------------------------
/com,!   Boundary conditions
/com,!-------------------------------------------------------------------------

!Symmetry line
LSEL,S,,,2,6,4
DL,ALL,,SYMM
ALLSEL

!clamped end
DL,5,,ALL,0

!Displaced end
DL,13,,UX,0
DL,13,,UY,0.0015    !Prescribed displacement


/com,!-------------------------------------------------------------------------
/com,!   Solve
/com,!-------------------------------------------------------------------------

/solu
tref,293
tunif,293
ANTYPE, STATIC
eqslv,sparse
SOLCONTROL, ON

NSUBST,30,1000,30
OUTRES,ERASE
OUTRES,NSOL,ALL
OUTRES,RSOL,ALL
OUTRES,NLOA,ALL
OUTRES,STRS,ALL
OUTRES,EPEL,ALL
OUTRES,MISC,ALL
AUTOTS,1
TIME,15
/NERR,500

SOLVE
FINISH


/com,!-------------------------------------------------------------------------
/com,!   Delete unnecessary files
/com,!-------------------------------------------------------------------------

/SYS,rm *.emat *.esav *.full *.page *.mntr *.PVTS *.lock
```

B-II. ANSYS Code Sample – 2D Axisymmetric Analysis

```
/COM,  ******************************************************************
/COM, ***           Axisymmetric TED geometry test with CZM        ***
/COM,  ******************************************************************
/COM, --  File: 25g3b_lc2.ans
/COM, --  Date: 2010-03-16
/COM, --  Creator: Fredrik Fors, 6670
/COM, --  Project: Exjobb KOMET
/COM, --
/COM, --  Description: Transient coupled analysis
/COM, --  Direct thermal-struct. 25 mm overlap, Fully Tapered Geometry
/COM ******************************************************************

/FILNAME,25g3b_lc2,1
/prep7

/com,!-------------------------------------------------------------------------
/com,!   Parameters
/com,!-------------------------------------------------------------------------

pi=acos(-1)

*SET,L_A,0.025       !length of adhesive zone
*SET,L,0.3           !Total tube length

*SET,R1,0.060        !Inner radius
*SET,R2,0.103        !Flange outer radius

*SET,T,0.005         !Tube wall thickness
*SET,T2,0.005        !Flange wall thickness
*SET,T3,0.014        !Flange axial thickness
*SET,T_A,0.2e-3      !Adhesvie thickness
*SET,TS,0.028        !Stiffness flange thickness

/com,!-------------------------------------------------------------------------
/com,!   Geometry
/com,!-------------------------------------------------------------------------

!Tube
K,1,R1,T3+TS-0.004
K,2,R1+0.001,T3+TS-0.004
K,3,R1,T3+L_A+0.002+TS
K,4,R1+T,T3+L_A+0.002+TS
K,5,R1,L+TS
K,6,R1+T,L+TS

A,1,2,4,3
A,3,4,6,5

!Flange
K,11,R1,0+TS
K,12,R2,0+TS
K,13,R2,T3+TS
K,14,R1+T+T2-0.002,T3+TS
K,15,R1+T+T2-0.002,T3+L_A-0.01+TS
K,16,R1+T+T2/5,T3+L_A+0.002+TS
K,17,R1+T,T3+L_A+0.002+TS
K,18,R1+0.001,T3+TS-0.004
K,19,R1,T3+TS-0.004

A,11,12,13,14,15,16,17,18,19
```

```
LFILLT,11,10,0.01
AL,19,17,18
AADD,3,4

!External Interface Flange
K,20,R1,0
K,21,R2,0


A,20,21,12,11


/com,!----------------------------------------------------------------------------
/com,!   Materials Definition
/com,!----------------------------------------------------------------------------
!Titanium 6-4
/input,ti64_forging,mat-SI,'../../'  !Read Ti data file


!Orthotropic CFRP
!Structural
MPDATA,EX,2,,10.1e9
MPDATA,EY,2,,52.9e9
MPDATA,EZ,2,,52.9e9
MPDATA,PRXY,2,,0.056
MPDATA,PRYZ,2,,0.317
MPDATA,PRXZ,2,,0.056
MPDATA,GXY,2,,3.69e9
MPDATA,GYZ,2,,20.1e9
MPDATA,GXZ,2,,3.69e9
!Thermal
MPDATA,C,2,,900
MPDATA,KXX,2,,0.78
MPDATA,KYY,2,,5.54
MPDATA,KZZ,2,,5.54
MPDATA,DENS,2,,1528
!Coupling
MPDATA,ALPX,2,,56.1e-6
MPDATA,ALPY,2,,3.8e-6
MPDATA,ALPZ,2,,3.8e-6

!EA-9394 Adhesive
TB,CZM,3,1,,CBDE    !CZM material
TBDATA,1,44.5e6,425,40e6,2000,0.005,1 !Adhesive mtrl parameters

/com,!----------------------------------------------------------------------------
/com,!   Mesh
/com,!----------------------------------------------------------------------------

!Element type definitions
ET,1,PLANE223,11
KEYO,1,3,1                   !Axisymmetric

ET,2,TARGE169

ET,3,CONTA172,1,1           !thermal-structural DOFs, penalty method
KEYO,3,9,1                  !exclude initial penetration
KEYO,3,10,0                 !redefine pair contact stiffness at load step
KEYO,3,12,5                 !always bonded contact

ET,4,MASS21,0,0,3           !Mass element for moment load

!AREA ATTRIBUTES
ASEL,S,AREA,,1,2
```

```
AATT,2,,1
ASEL,S,AREA,,3,5,2
AATT,1,,1
ALLSEL

!AREA MESH SIZES
AESI,1,0.001
AESI,2,0.001
AESI,3,0.001
AESI,5,0.001

!meshing areas
MSHK,1
AMES,2,3
MSHK,0
AMES,1,5,4

!refine at bond line
LREFINE,1,2,,1,1,CLEAN,ON
LREFINE,14,15,,1,1,CLEAN,ON

!Contact Zone Mesh
TYPE,2                    !Target surface mesh
MAT,3
LSEL,S,,,14              !Flange
NSLL,S,1
ESLN,S,0
ESURF

TYPE,3                    !Contact surface mesh
LSEL,S,,,2              !Tube
NSLL,S,1
ESLN,S,0
ESURF
RMODIF,1,3,-2e13         !Set normal penalty stiffness
RMODIF,1,12,-1e12         !Set tangent penalty stiffness
RMODIF,1,14,0.24/T_A      !Set thermal conductivity coefficient

!Rigid connection for moment load
N,100000,0,L+0.028
R,2,1E-10
REAL,2
TYPE,4
E,100000
LSEL,S,,,6
NSLL,S,1
NSEL,A,NODE,,100000
!NSEL,S,LOC,Y,L,0
CERIG,100000,ALL,ALL
DOF,UZ,ROTY
ALLSEL


/com,!-------------------------------------------------------------------------
/com,!   Boundary conditions
/com,!-------------------------------------------------------------------------

!Defining load tables
*DIM,TRANSTEMP,TABLE,12,2,1,TIME,TEMP
*SET,TRANSTEMP(1,0,1),0
*SET,TRANSTEMP(1,1,1),260
*SET,TRANSTEMP(2,0,1),20.6
```

```
*SET,TRANSTEMP(2,1,1),260
*SET,TRANSTEMP(3,0,1),22.4
*SET,TRANSTEMP(3,1,1),205
*SET,TRANSTEMP(4,0,1),238.4
*SET,TRANSTEMP(4,1,1),212
*SET,TRANSTEMP(5,0,1),244.4
*SET,TRANSTEMP(5,1,1),127
*SET,TRANSTEMP(6,0,1),259.4
*SET,TRANSTEMP(6,1,1),162
*SET,TRANSTEMP(7,0,1),409.3
*SET,TRANSTEMP(7,1,1),196
*SET,TRANSTEMP(8,0,1),415.3
*SET,TRANSTEMP(8,1,1),177
*SET,TRANSTEMP(9,0,1),424.3
*SET,TRANSTEMP(9,1,1),211
*SET,TRANSTEMP(10,0,1),490.3
*SET,TRANSTEMP(10,1,1),213
*SET,TRANSTEMP(11,0,1),499.3
*SET,TRANSTEMP(11,1,1),165
*SET,TRANSTEMP(12,0,1),514.3
*SET,TRANSTEMP(12,1,1),182

*DIM,TRANSPRES,TABLE,12,2,1,TIME,TEMP
*SET,TRANSPRES(1,0,1),0
*SET,TRANSPRES(1,1,1),0.64e6
*SET,TRANSPRES(2,0,1),20.6
*SET,TRANSPRES(2,1,1),0.69e6
*SET,TRANSPRES(3,0,1),22.4
*SET,TRANSPRES(3,1,1),7.68e6
*SET,TRANSPRES(4,0,1),238.4
*SET,TRANSPRES(4,1,1),7.95e6
*SET,TRANSPRES(5,0,1),244.4
*SET,TRANSPRES(5,1,1),0.7e6
*SET,TRANSPRES(6,0,1),259.4
*SET,TRANSPRES(6,1,1),0.29e6
*SET,TRANSPRES(7,0,1),409.3
*SET,TRANSPRES(7,1,1),0.68e6
*SET,TRANSPRES(8,0,1),415.3
*SET,TRANSPRES(8,1,1),0.27e6
*SET,TRANSPRES(9,0,1),424.3
*SET,TRANSPRES(9,1,1),8.07e6
*SET,TRANSPRES(10,0,1),490.3
*SET,TRANSPRES(10,1,1),8.11e6
*SET,TRANSPRES(11,0,1),499.3
*SET,TRANSPRES(11,1,1),0.91e6
*SET,TRANSPRES(12,0,1),514.3
*SET,TRANSPRES(12,1,1),0.3e6

*DIM,TRANSCONV,TABLE,12,2,1,TIME,TEMP
*SET,TRANSCONV(1,0,1),0
*SET,TRANSCONV(1,1,1),274.6
*SET,TRANSCONV(2,0,1),20.6
*SET,TRANSCONV(2,1,1),298.9
*SET,TRANSCONV(3,0,1),22.4
*SET,TRANSCONV(3,1,1),22214
*SET,TRANSCONV(4,0,1),238.4
*SET,TRANSCONV(4,1,1),22639
*SET,TRANSCONV(5,0,1),244.4
*SET,TRANSCONV(5,1,1),594
*SET,TRANSCONV(6,0,1),259.4
*SET,TRANSCONV(6,1,1),158.7
*SET,TRANSCONV(7,0,1),409.3
*SET,TRANSCONV(7,1,1),422
```

```
*SET,TRANSCONV(8,0,1),415.3
*SET,TRANSCONV(8,1,1),190.2
*SET,TRANSCONV(9,0,1),424.3
*SET,TRANSCONV(9,1,1),23343
*SET,TRANSCONV(10,0,1),490.3
*SET,TRANSCONV(10,1,1),23269
*SET,TRANSCONV(11,0,1),499.3
*SET,TRANSCONV(11,1,1),707.5
*SET,TRANSCONV(12,0,1),514.3
*SET,TRANSCONV(12,1,1),146.2

!Interior boundary convection
LSEL,S,LINE,,4,7,3
LSEL,A,LINE,,16,20,4
NSLL,S,1
SF,ALL,CONV,%TRANSCONV%,%TRANSTEMP%

!Exterior boundary convection
LSEL,S,LINE,,5
LSEL,A,LINE,,9,13
LSEL,A,LINE,,17,19,2
NSLL,S,1
SF,ALL,CONV,20,293
NSEL,S,LOC,X,R1+T-0.00001,R1+T+0.00001
NSEL,R,LOC,Y,L_A+T3+TesS,L_A+T3+0.002+TS
SF,ALL,CONV,20,293
ALLSEL

!Clamped Flange
DL,18,,UY,0
DL,18,,UZ,0

/com,!-----------------------------------------------------------------------
/com,!   Loads
/com,!-----------------------------------------------------------------------

!Axial Force
SFL,6,PRES,-35.65e6 !Axial force as pressure Fax/A

!Internal pressure
LSEL,S,LINE,,4,7,3
LSEL,A,LINE,,16
NSLL,S,1
SF,ALL,PRES,%TRANSPRES%
ALLSEL

!Moment
F,100000,MY,270
D,100000,TEMP,200

SAVE,/home/yy53171/FE-files/AxiSym/lc2/25g3b_lc2,db,MODEL
/com,!-----------------------------------------------------------------------
/com,!   Solve
/com,!-----------------------------------------------------------------------

!---Transient Coupled Solution---
/assign,rst,/home/yy53171/FE-files/AxiSym/lc2/25g3b_lc2,rst !sets result file
name

/solu

tref,293
!tunif,293
```

```
ANTYPE, TRANSIENT
TIMINT,ON,THERM
TIMINT,OFF,STRUCT
EQSLV,SPARSE
!NLGEOM, ON
SOLCONTROL, ON

NSUBST,514,1000,207
OUTRES,ERASE
OUTRES,STRS,ALL
OUTRES,NSOL,ALL
OUTRES,MISC,ALL
AUTOTS,ON
TIME,514.3
/NERR,500

SOLVE
FINISH

/com,!-------------------------------------------------------------------------
/com,!   Delete unnecessary files
/com,!-------------------------------------------------------------------------

/SYS,rm *.emat *.esav *.full *.page *.mntr *.PVTS *.lock
```

B-III. ANSYS Code Sample – 3D Submodel Analysis

```
/COM, *******************************************************************
/COM, ***                    3D TED flange geometry with CZM          ***
/COM, *******************************************************************
/COM, --  File: stat_fine_t489.ans
/COM, --  Date: 2010-03-23
/COM, --  Creator: Fredrik Fors, 6670
/COM, --  Project: Exjobb KOMET
/COM, --
/COM, --  Description: Static th-st analysis, 3D flange
/COM, --  fine mesh, BCs from trans_coarse @time 489 s
/COM *******************************************************************

/FILNAME,stat_fine_t489,1
/prep7
ABBRES,NEW,'MYAB',' ','../'

/com,!-------------------------------------------------------------------------
/com,!   Parameters
/com,!-------------------------------------------------------------------------

pi=acos(-1)

*SET,L_A,0.025        !length of adhesive zone
*SET,L,0.048          !Total tube length

*SET,R1,0.060         !Inner radius
*SET,R2,0.103         !Flange outer radius

*SET,T,0.005          !Tube wall thickness
*SET,T2,0.005         !Flange wall thickness
*SET,T3,0.014         !Flange axial thickness
*SET,T_A,0.2e-3       !Adhesvie thickness
*SET,TS,0             !Stiffness flange thickness

/com,!-------------------------------------------------------------------------
/com,!   Geometry
/com,!-------------------------------------------------------------------------

CLOCAL,11,0,0,0,0,0,0,-90

!Tube
K,1,R1,T3+TS-0.004
K,2,R1+0.001,T3+TS-0.004
K,3,R1,T3+L_A+0.002+TS
K,4,R1+T,T3+L_A+0.002+TS
K,5,R1,L+TS
K,6,R1+T,L+TS
A,1,2,4,6,5,3

!Flange
K,11,R1,0+TS
K,12,R2,0+TS
K,13,R2,T3+TS
K,14,R1+T+T2-0.002,T3+TS
K,15,R1+T+T2-0.002,T3+L_A-0.01+TS
K,16,R1+T+T2/5,T3+L_A+0.002+TS
K,17,R1+T,T3+L_A+0.002+TS
K,18,R1+0.001,T3+TS-0.004
K,19,R1,T3+TS-0.004
A,11,12,13,14,15,16,17,18,19
```

```
LFILLT,10,9,0.01
AL,17,18,16
AADD,2,3

!External Interface Flange
!K,20,R1,0
!K,21,R2,0
!A,20,21,12,11

!Keypoints defining axis of rotation
K,30,0,0
K,31,0,0.1
CSYS,0


/com,!-------------------------------------------------------------------------
/com,!   Materials Definition
/com,!-------------------------------------------------------------------------
!Titanium 6-4
/input,ti64_forging,mat-SI,'../'  !Read Ti data file


!Orthotropic CFRP
!Structural
MPDATA,EX,2,,10.1e9
MPDATA,EY,2,,52.9e9
MPDATA,EZ,2,,52.9e9
MPDATA,PRXY,2,,0.056
MPDATA,PRYZ,2,,0.317
MPDATA,PRXZ,2,,0.056
MPDATA,GXY,2,,3.69e9
MPDATA,GYZ,2,,20.1e9
MPDATA,GXZ,2,,3.69e9
!Thermal
MPDATA,C,2,,900
MPDATA,KXX,2,,0.78
MPDATA,KYY,2,,5.54
MPDATA,KZZ,2,,5.54
MPDATA,DENS,2,,1528
!Coupling
MPDATA,ALPX,2,,56.1e-6
MPDATA,ALPY,2,,3.8e-6
MPDATA,ALPZ,2,,3.8e-6

!EA-9394 Adhesive
TB,CZM,3,1,,CBDE    !CZM material
TBDATA,1,44.5e6,425,40e6,2000,0.005,1 !Adhesive mtrl parameters

/com,!-------------------------------------------------------------------------
/com,!   Mesh
/com,!-------------------------------------------------------------------------

!Element type definitions
ET,1,SOLID186              !Structural solid, full integration
ET,2,TARGE170
ET,3,CONTA174,0,1          !structural-thermal DOFs, penalty method
KEYO,3,9,1                 !exclude initial penetration
KEYO,3,10,0                !redefine pair contact stiffness at load step
KEYO,3,12,5                !always bonded contact

ET,5,MESH200,7             !Meshing element for 3D sweeping

!AREA ATTRIBUTES
ASEL,S,AREA,,1
```

```
AATT,2,,5
ASEL,S,AREA,,4
AATT,1,,5
ALLSEL

!Mapped Sweep Mesh
AESIZE,1,0.002
LESIZE,2,0.0006
SMRT,8
AMES,1
AESIZE,4,0.003
LESIZE,8,0.005
LESIZE,9,0.005,,,0.6
LESIZE,7,0.004,,,1.5
LESIZE,13,0.0006
LESIZE,12,0.0006
LESIZE,11,0.002,,,0.2
SMRT,8
AMES,4

!Cylindrical coord. system for meshing
CSYS,5
CLOCAL,15,1
ESYS,15

EXTOPT,ON
ESIZE,,60
TYPE,1
VROTAT,1,4,,,,,30,31,-50,1

!Contact Zone Mesh
CSYS,0
ESYS,0
TYPE,2                    !Target surface mesh
MAT,3
ASEL,S,,,19,36,17         !Flange
NSLA,S,1
ESLN,S,0
ESURF

TYPE,3                    !Contact surface mesh
ASEL,S,,,3,22,19          !Tube
NSLA,S,1
ESLN,S,0
ESURF
RMODIF,1,3,-2e13          !Set normal penalty stiffness
RMODIF,1,12,-1e12         !Set tangent penalty stiffness
RMODIF,1,14,0.24/T_A      !Set thermal conductivity coefficient
ALLSEL

/com,!-----------------------------------------------------------------------
/com,!   Boundary conditions
/com,!-----------------------------------------------------------------------

!Import temp data from transient solution
/INPUT,/home/yy53171/FE-files/3D/thbc,bfi

!Read cut-plane BC's
/INPUT,/home/yy53171/FE-files/3D/stbc,cbd

!Clamped Flange
ASEL,S,LOC,Y,0
NSLA,S,1
```

```
CSYS,15
NROTAT,ALL
D,ALL,UY,0,,,,UZ
CSYS,0
ALLSEL

/com,!----------------------------------------------------------------------
/com,!   Loads
/com,!----------------------------------------------------------------------

!Internal pressure
CSYS,5
ASEL,S,LOC,X,R1
NSLA,S,1
CSYS,0
SF,ALL,PRES,8.1e6
ALLSEL

SAVE,/home/yy53171/FE-files/3D/stat_fine_t489,db

/com,!----------------------------------------------------------------------
/com,!   Solve
/com,!----------------------------------------------------------------------

!---Static Structural Solution---
/ASSIGN,rst,/home/yy53171/FE-files/3D/stat_fine_t489,rst !sets result file name
/SOLU

TREF,293
ANTYPE, STATIC
EQSLV,SPARSE
SOLCONTROL, ON
NSUBST,1
OUTRES,ERASE
OUTRES,STRS,ALL
OUTRES,NSOL,ALL
OUTRES,MISC,ALL
AUTOTS,ON
TIME,1
/NERR,500

SOLVE
FINISH
```